Representing grounding-line dynamics in Antarctic ice-sheet models
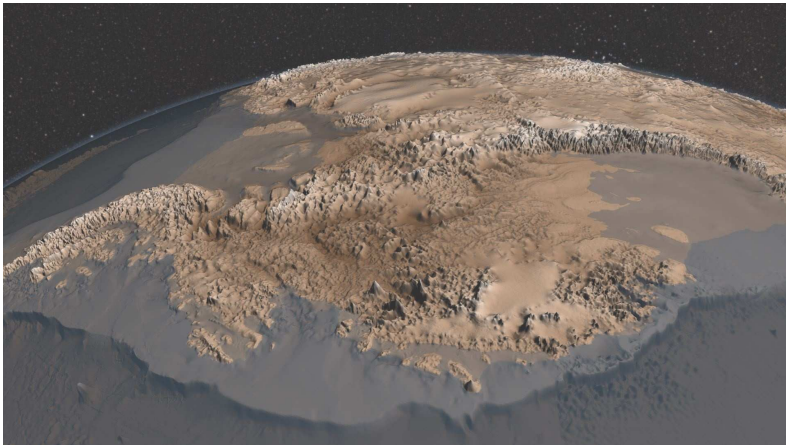
David Docquier

Université Libre de Bruxelles (ULB)
Faculté des Sciences
Laboratoire de Glaciologie

Representing grounding-line dynamics in Antarctic ice-sheet models

Représentation de la dynamique de la ligne d'ancrage dans les modèles cryosphériques antarctiques

David Docquier

Thèse de doctorat
présentée en vue de l'obtention du titre de
Docteur en Sciences

Promoteur : Prof. F. Pattyn

Submitted on 22 August 2013
Public defense held on 4 October 2013

Whatever you do will be insignificant, but it is very important that you do it.

[Mahatma Gandhi]

Contents

Abstract

Since the mid-20th century, global average temperatures have dramatically risen mostly due to the increasing amount of greenhouse gas emissions in the atmosphere. The effects of this recent global warming are already evident and could be exacerbated in the near future if no real action is taken. Recent ice loss in West Antarctica, monitored by satellite measurements and other techniques, gives cause for concern in such a warming world. A major part of this loss has been driven by warm water masses penetrating underneath the ice shelves in this region. This has led to a flow acceleration of the inland outlet glaciers and a greater discharge of ice to the ocean. The actual resulting contribution of West Antarctica to sea-level rise is estimated to be ~ 0.2 mm per year between 1992 and 2011, i.e. about one third of the ice-sheet contribution (Antarctica and Greenland), and is expected to increase in the near future.

In this thesis, we first clearly demonstrate that modeling grounding-line (the boundary between grounded and floating ice) migration depends on both the numerical approach and the physical approximation of the ice-sheet model used. Ice-sheet models prescribing the ice flux at the grounding line and using appropriate physical level and numerical approach converge to the same steady-state grounding-line position irrespective of the grid size used. However, the transient behavior of those models is less accurate than other models and leads to an overestimated grounding-line discharge. Therefore, they need to be used with particular attention on short time scales. Furthermore, the non-inclusion of vertical shear stress in those models increases the effective viscosity and gives steady-state grounding-line positions further downstream when compared to full-Stokes models.

The second major finding of this thesis is the high control of geometry (glacier width and bedrock topography) on Thwaites Glacier, one of the fastest-flowing outlet glaciers in West Antarctica. A flowline finite-difference Shallow-Shelf Approximation (SSA) model is applied to the glacier and shows that ice-flow convergence (through width parameterization) slows down the grounding-line retreat when compared to simulations where the width is constant. A new buttressing parameterization is also tested on the glacier and permits a better understanding of this effect. Finally, the three-dimensional version of the model above is applied to Thwaites Glacier and highlights the strong control of lateral variations in bedrock topography on grounding-line migration.

Résumé

Depuis le milieu du 20e siècle, les températures moyennes globales ont fortement augmenté principalement à cause de l'augmentation des émissions de gaz à effet de serre d'origine humaine. Les effets de ce réchauffement global récent sont déjà détectables et pourraient s'accentuer dans un futur proche si aucune mesure réelle n'est prise. La perte récente de glace en Antarctique de l'Ouest, enregistrée par mesures satellites et d'autres techniques, est préoccupante dans un monde qui se réchauffe. Une grande partie de cette perte de glace est due à la pénétration de masses d'eau chaude sous les plateformes de glace flottante dans cette région. Cela engendre une accélération de l'écoulement des glaciers émissaires et une plus grande décharge de glace vers l'océan. Ainsi, la contribution récente à la hausse du niveau de la mer de l'Antarctique de l'Ouest s'élève à ~ 0.2 mm par an entre 1992 et 2011, c'est-à-dire près du tiers de la contribution des calottes glaciaires (Antarctique et Groenland). On estime que cette contribution va continuer à augmenter dans le futur proche.

Dans cette thèse, nous démontrons clairement que la modélisation de la migration de la ligne d'ancrage (frontière entre glaces posée et flottante) dépend de l'approche numérique et de l'approximation physique du modèle cryosphérique utilisé. Les modèles cryosphériques qui prescrivent le flux glaciaire à la ligne d'ancrage et qui utilisent un niveau de physique et une approche numérique appropriés convergent vers la même position d'équilibre de la ligne d'ancrage quelle que soit la taille de maille utilisée. Cependant, le comportement transitoire de ces modèles est moins précis que d'autres modèles et mène à une surestimation du flux à la ligne d'ancrage. Dès lors, ces modèles doivent être utilisés avec précaution sur de courtes périodes de temps. De plus, la non inclusion des contraintes verticales de cisaillement dans ces modèles augmente la viscosité effective et donne des positions d'équilibre de la ligne d'ancrage plus en aval en comparaison avec les modèles 'full-Stokes'.

La seconde découverte majeure de cette thèse est le contrôle important exercé par la géométrie (largeur du glacier et topographie du lit rocheux) sur Thwaites Glacier, l'un des glaciers émissaires les plus rapides en Antarctique de l'Ouest. Un modèle 'Shallow-Shelf Approximation' (SSA) résolvant les différences finies le long d'une ligne d'écoulement est appliqué au glacier et montre que la convergence de l'écoulement glaciaire (au travers de la paramétrisation de la largeur) ralentit le retrait de la ligne d'ancrage comparé aux simulations où la

largeur est constante. Une nouvelle paramétrisation de l'effet arc-boutant est testée sur le glacier et permet de mieux comprendre cet effet. Finalement, la version en trois dimensions du modèle ci-dessus est appliquée à Thwaites Glacier et met en évidence le contrôle important des variations latérales de l'altitude du lit rocheux sur la migration de la ligne d'ancrage.

Acknowledgments - Remerciements

This thesis is the result of four years of hard work during which I have learnt a broad range of concepts in glaciology and developed different skills necessary to achieve this marathon (perseverance, autonomy, teamwork, communication, rigour, innovation, etc.). Many people contributed directly or indirectly to the development of this long but fast project.

The first person I thank is my supervisor, Frank Pattyn. Merci beaucoup pour ton encadrement pendant cette thèse Frank. Tu m'as accompagné du début à la fin et j'ai appris énormément de choses grâce à toi, que ce soit à propos des méandres numériques de la modélisation ou de l'art de la communication (aussi bien écrite qu'orale). Tu m'as véritablement lancé au début de la thèse et tu m'as directement fait confiance pour effectuer toute une série de tâches (participation à des congrès, enseignement, encadrement de mémoires, activités de vulgarisation, etc.). Tu m'as laissé beaucoup d'autonomie tout en me remettant sur les rails lorsque je m'éloignais un peu trop du chemin. Grâce à toi, j'ai pu non seulement découvrir un domaine précis des sciences de la Terre mais aussi effectuer une myriade de voyages à l'étranger dans le cadre de séjours de recherche, conférences et cours. C'est toi qui m'as 'boosté' pour devenir 'Early Career Member' du projet ice2sea, ce qui m'a permis d'apprendre beaucoup de choses. Tu m'as véritablement intégré au sein de la communauté glaciologique internationale. Je suis reconnaissant envers toi pour tout ça et bien d'autres choses encore.

Then, I would like to thank the jury members, Jean-Louis Tison, Lionel Favier, Kael Hanson and Richard Hindmarsh for accepting to assess this work.

I send warm thanks to all the lab members at ULB with who I could share knowledge, experiences, friendship and great times. It was really a great opportunity for me to be involved in that very professional and relaxed team. Merci Jean-Louis pour ton soutien et tes questions et conseils pertinents lors des différentes réunions d'accompagnement, qui m'ont chaque fois permis de recalibrer le sujet de ma thèse. Merci Claire pour ton aide administrative très efficace ainsi que pour ton aide organisationnelle 'récréative' (repas de Noël, dîner glaciologues/géologues, drinks de thèses, etc.). Merci Saïda pour ta bonne humeur, tes encouragements et les nombreuses discussions philosophiques. Merci Charlotte pour avoir partagé avec dynamisme le même bureau que moi pendant deux années et m'avoir prodigué de précieux conseils pour mener ma thèse à bien. Thanks a lot Faezeh for motivating me in the beginning

of the PhD to do as many activities as possible. Merci Thierry pour ton énergie débordante et pour ton aide informatique précieuse. Merci Mathieu pour les discussions très intéressantes et pour ton amitié, qui s'est notamment renforcée lors des quelques voyages effectués ensemble. Merci Fred pour ton écoute et tes conseils à la fois professionnels et sportifs. Gracias Carlos por la comida en tu kot, me gustaría ir a Bolivia ahora. Merci Laura pour tes explications concernant les modèles de Frank. Merci Marie pour ton soutien tant au laboratoire qu'à l'étranger (lors de conférences à Vienne et en Californie entre autres). Merci Denis pour avoir initié des événements tels que le Science Fair APECS et pour avoir partagé une décapotable du tonnerre avec moi en Californie. Merci Brice pour ton implication très active au sein du labo et ton jusqu'au-boutisme dans la résolution des problèmes. Merci Gauthier et Thomas pour votre enthousiasme et votre participation active au raid de La Roche. Merci Jiayun et Morgane pour votre investissement dans les différentes activités ainsi que pour votre gentillesse. Merci beaucoup Reinhard pour tes nombreux conseils scientifiques d'expert, l'organisation d'événements de labo, la relecture d'une partie de ma thèse et pour l'amitié qui s'est créée entre nous pendant ces deux dernières années passées dans le même bureau. Thanks a lot Ceri for having read a part of my thesis and I wish you all the best with your new life in Brussels. Merci à mon petit mémorant, Charles, pour m'avoir appris des choses sur Pine Island Glacier. Merci aussi à François et Véronique.

Thanks to the lab of 'Ice and Climate' at the VUB, especially to Johannes for organizing the b-GLAMOR seminars with me and for all the very interesting discussions we had about ice-sheet modeling and other (non-)related topics. Thanks also Johannes for the sea-level experiments. Thanks Philippe, Harry, Heiko and Oleg.

Thanks to other researchers from ULB, spécialement Robin pour les moments de course à pied, Vinciane pour l'organisation du dîner géologues/glaciologues, Chiara pour l'aide logistique associée à l'enseignement, Pierre Coheur pour m'avoir fait confiance dans les organisations liées à l'écolde doctorale UNITER, Lionel, Martin et Julie pour leur aide au sein d'UNITER.

I thank all the people with who I collaborated during my short stay at LGGE in Grenoble. Merci beaucoup Gaël pour ton encadrement et tes nombreux conseils, notamment concernant ton désir insatiable d'en savoir plus sur l'influence d'un modèle 'schoofé'. Tu m'as permis de réellement faire un pas en avant dans mes recherches et tu es un contributeur essentiel aux Chapitres 2, 3 et 4. Merci Anne-Sophie pour la collaboration active sur la ligne d'échouage, non seulement à Grenoble mais aussi à Bruxelles, qui a abouti à la publication d'un article. Merci Lionel pour ton aide dans l'utilisation d'Elmer/Ice et tes nombreux conseils en or, non seulement à Grenoble mais aussi pendant le début de ton postdoc à Bruxelles. Merci Olivier et Catherine pour vos questions pertinentes lors de mon séjour à Grenoble ainsi que lors de diverses conférences. Merci Fabien pour ton aide informatique précieuse. Merci Vincent pour les discussions intéressantes sur le 'schoofage'.

I also warmly thank David Pollard from Pennsylvania State University (USA). You greatly welcomed me during two months in your lab and I am very glad to have worked with you

on Thwaites Glacier. You provided me very insightful advice, not only during my short stay in Penn State, but also through numerous emails. Thanks a lot for your comments concerning the first paper (Chapter 2), they permitted to greatly improve the article. I also thank you for all non-professional stuff, e.g. eating on campus and hiking. Thanks to your family too for Thanksgiving. Thanks to the team of glaciology at Penn State. Thanks Eric for the accomodation in Penn State as well as Tarun for squash and integration.

Thanks a lot to other international collaborators with who I had very interesting discussions concerning my thesis : Richard Hindmarsh, Thomas Zwinger, Byron Parizek, Steph Cornford, Steve Price, Ruppert Gladstone, etc. Thanks to Anne Le Brocq, Kirsty Tinto and Ian Joughin for the provision of data concerning Thwaites Glacier as well as their constructive comments through emails.

Thanks also to the members of the European FP7 programme ice2sea in which my work was embedded. I had the chance to attend most ice2sea Open Forums (e.g. Amsterdam, Copenhagen, London) and to present my research there. Thanks to the steering committee of ice2sea, in which I was involved as an early career member with Louise Sorensen. Special thanks to David Vaughan (coordinator), Elaina Ford (manager), Gil Alexander (assistant) and Hartmut Hellmer (leader of Work Package 4).

Je remercie la Fédération Wallonie-Bruxelles pour m'avoir alloué une bourse de doctorat (Action de Recherche Concertée IceCubeDyn) pendant ces quatre années de thèse, ainsi que le FNRS pour les financements de divers voyages de recherche à l'étranger.

I also would like to thank Regine Hock for organizing the International Summer School in Glaciology in Alaska in June 2010, which was a key moment of my PhD, where I could learn many glaciological concepts in a wonderful environment and meet other international PhD students. Thanks Jan for your friendship and for having invited me later to Utrecht for both giving a talk and attending your PhD defense. Unfortunately, I did not learn Dutch but I am learning Greek... Thanks Markus for your invitation to come to Oslo and other great times when we met (Brussels, San Francisco). Thanks Joanna for the accommodation. Thanks to the other PhD students who attended the summer school in Alaska, with who I kept in touch, especially Pierre, Alicia, Tyler and Jake.

Thanks to the lab of climatology at ULg, where I sometimes went to share my work and results. Merci Xavier pour m'avoir précédemment encadré (mémoire) et avoir continué à t'intéresser à mes recherches. Merci Sébastien et Alexandre pour le partage de connaissances climato-glaciologiques et votre amitié. Merci M. Erpicum pour votre enthousiasme et votre intérêt dans ma thèse.

I also thank all my friends : even if you did not professionally collaborate with me, you contributed to my social blossoming. Merci à tous les anciens camarades de l'ULg, et spécialement Nadia, Gilles, Charline, Marie, Valentin, Matthieu, Tommy, Nicolas, Francq, Caro, Véro, François, Yannick, Martin, Stéphane, Pierre, Julie, Brice, Bernard, René, Clémentine, Philippe, Antoine, LeUyen et Andrea. Merci aux grands animateurs Romain, Godefroid, Sophie et Larissa.

Thanks a lot to the Erasmus students who I met several times during the thesis : Mohammad, Justine, Mathilde, Razvan, Jiri, Jana, Xavier, Mathieu, etc. Merci aux amis de Bruxelles : Giulia, Laure, Laura, Thibault, Kim-Chi, Alain, Olivier, Michel, Seb, Hicham, Patrick, Pascal, Hélène, Anne-Sophie et Fred entre autres. Muchas gracias a los amigos que conocí en Ecuador : la familia Barcia, Carmen y Virginia, Tito, Nadia, Guilhem, Balthazar, Thibaut, Stephan, etc. Merci aux voisins de la campagne : Vincent, Céline, Thomas, Pierre-Henri et les autres.

J'adresse un énorme remerciement à ma famille proche pour leur patience et leur incontournable amour : Maman, Papa, Catherine, Anne-Cécile, Charlotte, Simon-Pierre, Pierre, Arnaud et Charlotte H. Merci aussi à Mouty ainsi qu'à mes cousin(e)s, tantes et oncles. Merci à Josiane. Ευχαριστώ πάρα πολύ την οικογένεια της Χρύσας για τη θερμή υποδοχή τους, ειδικά την Βιβή, τον Νίκο, τον Βαγγέλη, την Άρτεμη και τον Γιάννη.

Τελικά, ευχαριστώ πάρα πολύ την αγάπη της ζωής μου. Η διαδρόμη ήταν πολύ πιο εύκολο με εσένα, Χρύσα.

1

Introduction

1.1 Recent ice-sheet loss

Since the start of the Industrial Revolution, i.e. the middle of the 18th century, humankind has altered the global climate through the increasing amount of greenhouse gas emissions in the atmosphere [Solomon and others, 2007]. Most of the observed increase in global average temperatures since the mid-20th century (Fig. 1.1) is due to this anthropogenic influence [Solomon and others, 2007]. Beside this recent global warming, ice losses have been identified along the coasts of the two great ice sheets[1], i.e. Antarctica and Greenland. These ice sheets contain ~ 90 % and ~ 9 % of the world's glacier ice respectively, corresponding to a sea-level rise equivalent of ~ 58 m and ~ 7 m respectively [Church and others, 2001; Fretwell and others, 2013].

An ice sheet forms by the accumulation and the compaction of snow over many years, with sufficiently low temperatures. Once the ice sheet becomes large enough, it starts to flow due to its own weight and by the action of gravity. Its volume is controlled by the mass balance, i.e. the difference between accumulation, by which snow/ice is added to the ice sheet, and ablation, by which snow/ice is lost, during an entire year. Accumulation is mainly done through snow precipitation, while a series of different ablation processes exist.

The ablation processes responsible for the recent observed ice-sheet loss can be divided into two groups: surface melting and dynamical changes (i.e. iceberg calving and basal melting underneath the ice shelves[2]). In Greenland, ice is mainly lost through surface melting and both iceberg calving and basal melting [Van den Broeke and others, 2009; Rignot and others, 2011], while basal melting and iceberg calving dominate Antarctic ice-sheet loss [Pritchard and others, 2012; Rignot and others, 2013] (Fig. 1.2). Almost no surface melting is present in Antarctica (except in the warmer Antarctic Peninsula) due to the extremely cold temperatures [Walton, 2013]. A recent study [Rignot and others, 2013] shows that basal melting accounts for more than half the Antarctic ice loss, much more than previous estimates [Cuffey and

---

[1]Ice sheets are ice masses of continental size (area > 50 000 km^2), which rest on solid land [Greve and Blatter, 2009].

[2]Ice shelves consist of floating ice nourished by the inflow from an adjacent ice sheet, typically stabilized by large bays [Greve and Blatter, 2009].

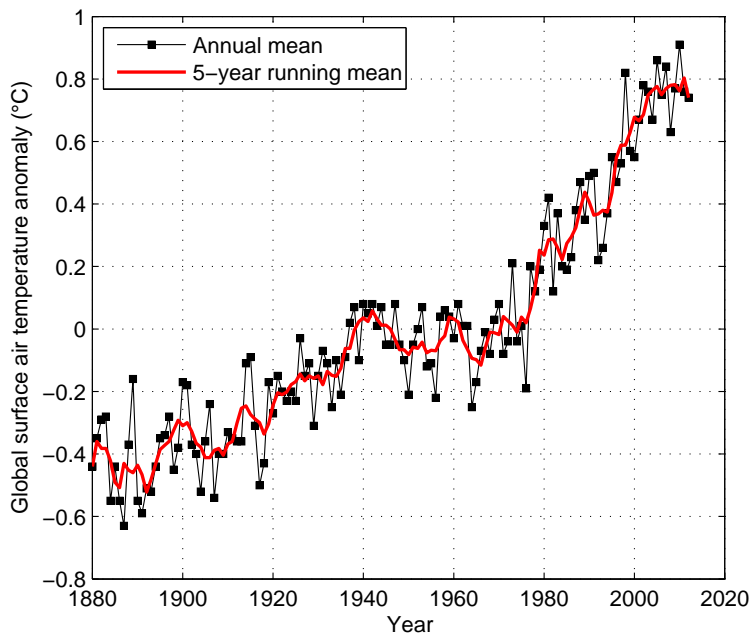**Figure 1.1:** *Global surface air temperature anomaly from 1880 to 2012, with the base period 1951-1980 [Graph created with data from Goddard Institute for Space Studies (GISS),* `http: // data. giss. nasa. gov/ gistemp/ graphs_ v3/ ].`
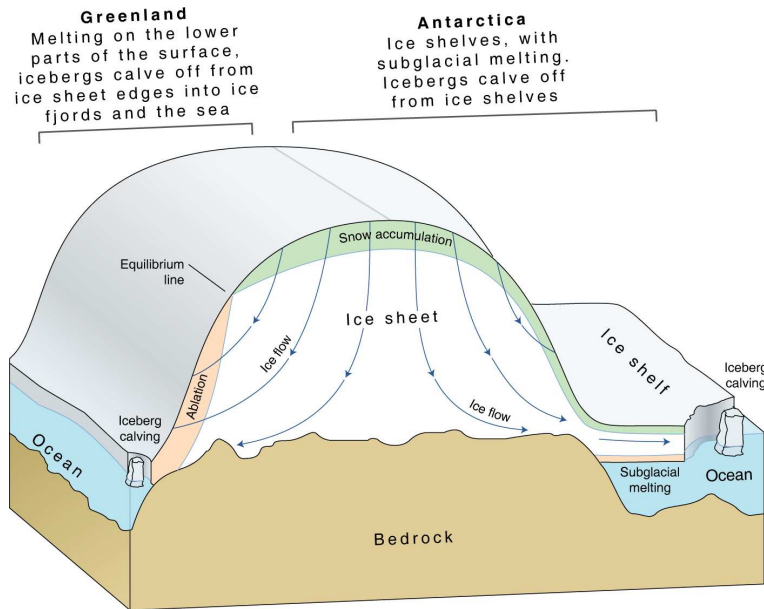
Figure 1.2: *Schematic illustration of Greenland (left) and Antarctic (right) ice sheets, where the main processes of mass gain (snow accumulation) and loss (surface ablation/melting in Greenland, basal melting and iceberg calving for both ice sheets) can be identified. Also shown is the ice flow, which is driven by gravity to slide and flow downhill from the highest points of the interior to the coast [Image credit: Hugo Ahlenius, UNEP/GRID-Arendal [2007], based on material provided by K. Steffen, CIRES/Univ. of Colorado, `http://www.grida.no/graphicslib/detail/ ice-sheets-schematic-illustration-for-greenland-and-antarctica_13c2`, 12/06/2013].*

Paterson, 2010], and that half of the meltwater comes from 10 small outlet glaciers in West Antarctica and Antarctic Peninsula.

Recent techniques, including radar altimetry [Wingham and others, 2009], laser altimetry [Zwally and others, 2011], gravimetry [Chen and others, 2009; Velicogna, 2009; Chen and others, 2011] and mass-budget method [Rignot and others, 2008; Van den Broeke and others, 2009; Rignot and others, 2011], show a large spread of mass-change estimates in Antarctica and Greenland for the past two decades [Hanna and others, 2013]. However, the disparity among different techniques has been considerably reduced in the last years [Shepherd and others, 2012], partly due to the improvement in glacial isostatic adjustment (GIA) models [King and others, 2012] coupled with more robust Global Positioning System (GPS) measurements [Thomas and others, 2011]. While Greenland has been loosing ice at an increasing pace[3], the situation is less clear for Antarctica with large dynamic losses in West Antarctica

---

[3]Wouters and others [2013] suggest that it is not possible to detect an acceleration in ice-sheet loss with sufficient certainty due to the short observational record and large temporal climate variability. About 20 years would be necessary.

and surface mass balance (SMB) gain in East Antarctica (Fig. 1.3) [Shepherd and others, 2012].

Antarctic and Greenland ice sheets play an important role in the total contribution to current sea-level rise. The Fourth Assessment Report (AR4) from Intergovernmental Panel on Climate Change (IPCC) identified a contribution from the ice sheets to sea-level rise of ~ 0.19 mm a^{-1} from 1961 to 2003 and ~ 0.42 mm a^{-1} from 1993 to 2003 [Bindoff and others, 2007], i.e. ~ 11 % and ~ 14 % of the total observed sea-level rise, respectively. Other major causes of sea-level rise are melting of mountain glaciers and ice caps and ocean thermal expansion [Cazenave and Llovel, 2010; Nicholls and Cazenave, 2010]. More recently, Shepherd and others [2012] reconciled satellite measurements and mass-budget method and found that the polar ice sheets have contributed ~ 0.59 mm a^{-1} to the rate of global sea-level rise from 1992 to 2011. According to another recent study, the ice-sheet contribution measured with Gravity Recovery and Climate Experiment (GRACE) satellites reaches a value of ~ 1.19 mm a^{-1} from 2005 to 2011 for a total sea-level rise of ~ 2.4 mm a^{-1} [Chen and others, 2013], i.e. ~ 50 % of the total. This increasing contribution is due to three factors: 1) the earlier IPCC assessment was made without the critical new information from Argo (for steric component) and GRACE (for land-ice component); 2) the time period is different; 3) the melting of polar ice sheets, mountain glaciers and ice caps has accelerated in the last years [Chen and others, 2013].

According to the European programme *ice2sea*[4], which uses a range of ice-flow models and a medium-range IPCC AR4 emission scenario (A1B), the sea level is projected to rise by ~ 0.5 to 24 cm by 2100 due solely to Greenland and Antarctic ice sheets [ice2sea, 2013]. This amounts to ~ 3.5 up to 37 cm if mountain glaciers and ice caps are also considered. Led by American researchers, the *SeaRISE*[5] project gives a mean sea-level rise of ~ 30 cm by 2100 due to ice sheets, with a range among models of 76 cm [Bindschadler and others, 2013], according to an experiment approximating the IPCC AR5 RCP8.5 scenario[6], which is a more extreme scenario compared to A1B.

Nevertheless, different caveats concern these two projects. They both use a specific IPCC scenario: *ice2sea* projections use a mid-range scenario (A1B) and may not be appropriate for more severe scenarios, while *SeaRISE* employs a more extreme scenario (RCP8.5) that may be too dramatic. Second, both projects mainly assume a one-way coupling, i.e. global climate affects regional climate that impacts ice masses, so coupling and feedbacks between ice and atmospheric and ocean systems are not really included in the calculations. Concerning *ice2sea*, ice-sheet models do not cover the whole East Antarctic ice sheet, which may be a source of error in the projections even if East Antarctica will not greatly contribute to sea-level increase

---

[4] *ice2sea* is a European Framework Package (FP) 7 programme (2009-2013) aiming at estimating the future contribution of continental ice (i.e. ice sheets and glaciers) to sea-level rise for the next 200 years (`http://www.ice2sea.eu`).

[5] *SeaRISE* (Sea-level Response to Ice Sheet Evolution) is a community organized effort to estimate the upper bound of ice-sheet contributions to sea level in the next 100–200 years (`http://websrv.cs.umt.edu/isis/index.php/SeaRISE_Assessment`).

[6] RCP8.5 stands for Representative Concentration Pathway with a rising radiative forcing in the 21st century leading to 8.5 W m^{-2} by 2100 [Moss and others, 2010]. This scenario is characterized by increasing greenhouse gas emissions over time representative for scenarios in the literature leading to high greenhouse gas concentration levels.
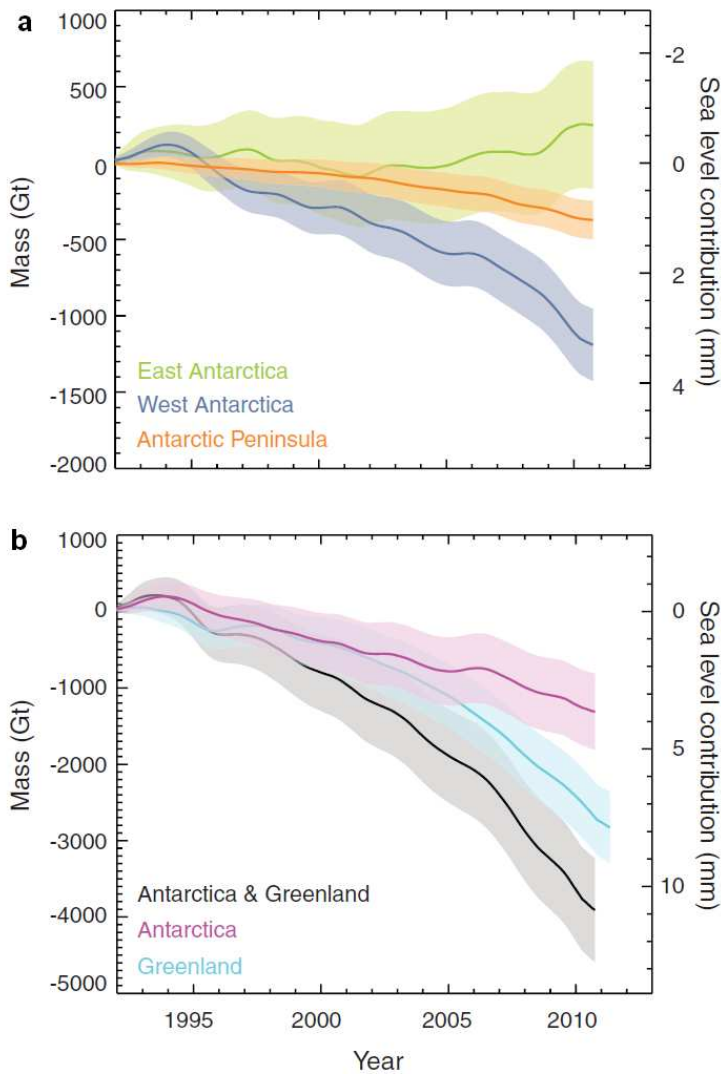
Figure 1.3: *Cumulative mass changes (left axis) and equivalent sea-level contribution (right axis, 1 mm sea-level rise corresponds to 360 Gt ice loss) in (a) the different regions of Antarctica, as well as (b) in the whole Antarctic and Greenland ice sheets. These mass changes result from a reconciliation of satellite measurements (radar, laser and gravimetry) and mass-budget method [Image credit: Figure 5 of Shepherd and others [2012]].*

[ice2sea, 2013]. *SeaRISE* also suffers from different caveats, one being that it compiles the results of 10 ice-sheet models but only four of them have an ice shelf. According to Pattyn and Durand [2013], none of them can cope with grounding-line migration over short time scales. Finally, *SeaRISE* results are only an estimate of ice-sheet response to environmental forcing (atmosphere, basal sliding, basal melting) and their ability to simulate the more dynamic changes recently observed is limited [Bindschadler and others, 2013].

1.2   Stability of West Antarctica

The Antarctic ice sheet and its ice shelves cover $\sim$ 14 million km^2 ($\sim$ 98 % of the Antarctic continent) and contain $\sim$ 27 million km^3 [Fretwell and others, 2013]. It is the largest ice mass on Earth. The mean ice thickness is about 1900 m with an average bed depth of 80 m below sea level [Fretwell and others, 2013]. While cold temperatures and very dry air dominate the interior of Antarctica, the coastal regions are much less extreme, although temperatures rarely rise above freezing point. The continent is divided in two ice sheets (West and East Antarctica) by the Transantarctic Mountains (Fig. 1.4). In some studies, the Antarctic Peninsula is also considered as a separate entity. Also shown in Figure 1.4 are the largest ice shelves (Ronne, Filchner, Ross and Amery).

Rapid ice-flow acceleration has been observed for some outlet glaciers in West Antarctica (especially in the Amundsen Sea Embayment [ASE]), with a large contribution coming from Pine Island Glacier (PIG) and Thwaites Glaciers (TG), leading to an important ice loss [Rignot and others, 2011]. The origin of this recent acceleration has been identified as an increase in melt rates underneath the ice shelves (what we call 'basal (or sub-ice shelf) melt rates' throughout this document) attached to these glaciers [Pritchard and others, 2012]. Figure 1.5 shows that the highest basal melt rates in Antarctica are located underneath small ice shelves (mainly in West Antarctica and Antarctic Peninsula), where the proportion of basal melting in the total ice mass loss is higher compared to iceberg calving. The bigger Ronne, Filchner, Ross and Amery ice shelves have smaller basal melt rates and a larger proportion of iceberg calving compared to basal melting.

The particularly high melt rates observed underneath ASE ice shelves have recently been attributed to warm Circumpolar Deep Water (CDW) penetrating deeply into cavities beneath those ice shelves [Jacobs and others, 2011, 2012; Pritchard and others, 2012; Steig and others, 2012]. This warm current carries important amount of heat that melts the base of the ice shelves. The strong direct influx of CDW in this region is thought to be due to a change in local wind stress near the continental shelf edge at a certain time of the year (fall and early winter) [Thoma and others, 2008; Steig and others, 2012], rather than an actual warming of the CDW.

Increased basal melt rates can lead to ice-shelf thinning and steepening near the grounding line, which is the boundary between the ice sheet and the ice shelf. Figure 1.6 shows rates
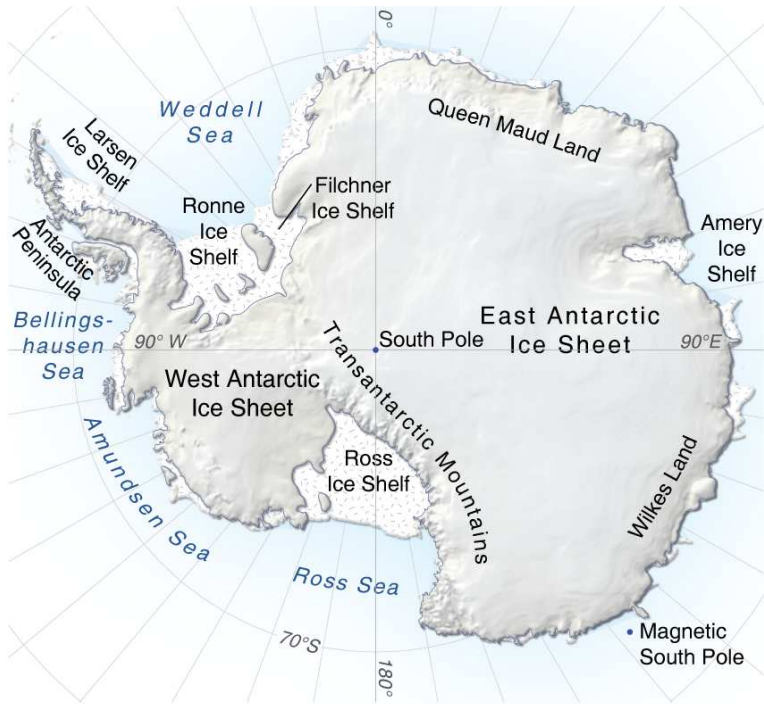
Figure 1.4: *Antarctica and its different regions [Image credit: Hugo Ahlenius, UNEP/GRID-Arendal [2007], `http://www.grida.no/graphicslib/detail/antarctica-topographic-map_ 8716`, 27/06/2013].*
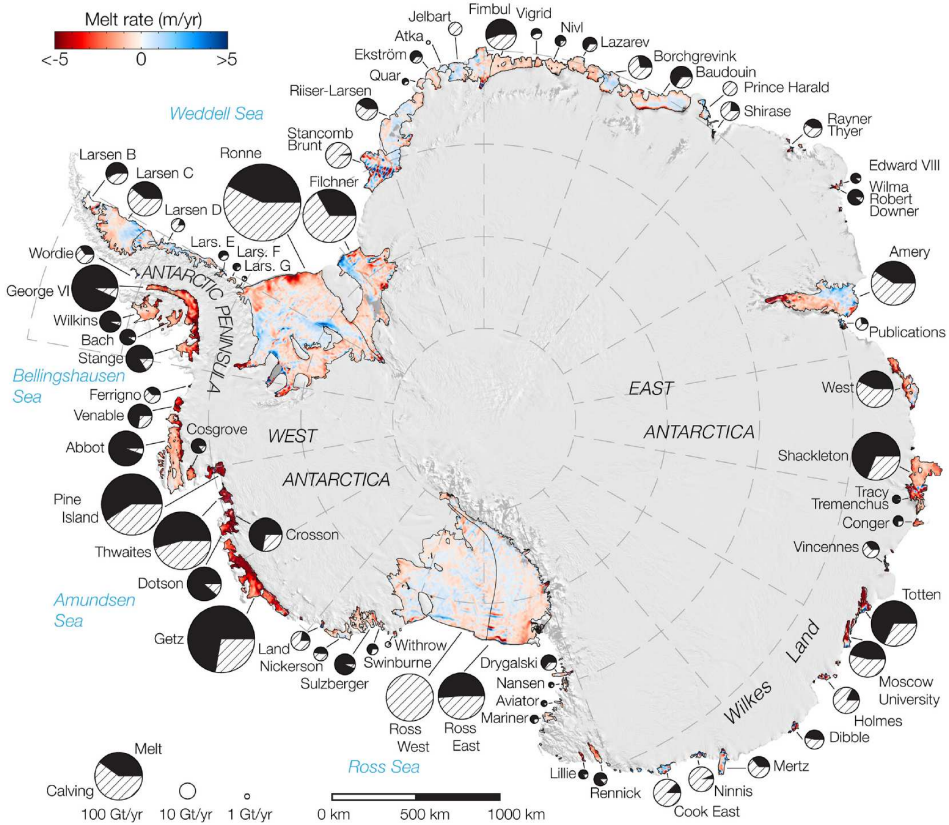
Figure 1.5: *Basal melt rates of Antarctic ice shelves calculated by Rignot and others [2013] using 2003-2008 ice-shelf thickening, 2007-2008 flux divergence and 1979—2010 surface accumulation, overlaid on a 2009 Moderate Resolution Imaging Spectroradiometer (MODIS) mosaic of Antarctica. Black lines show ice-shelf perimeters in 2007—2008. Each circular graph is proportional in area to the total ice mass loss measured from each ice shelf with the proportion of ice lost due to iceberg calving and basal melting denoted by hatched lines and in black respectively [Image credit: Figure 1 of Rignot and others [2013]].*
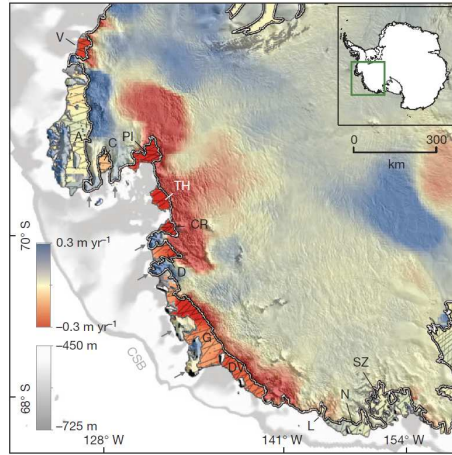
Figure 1.6: *Rates of surface elevation change on the ice shelves and grounded ice of ASE from 2003 to 2008. PI and TH stand for Pine Island and Thwaites Glaciers respectively [Image credit: Figure 3 of Pritchard and others [2012]].*

of surface elevation change on ice shelves and grounded ice in ASE from 2003 to 2008. This, in turn, reduces the buttressing effect provided by ice shelves to the inland outlet glaciers. The buttressing effect arises from friction between the ice shelves and their embayed walls or from regrounding on localized topographic highs in the bed, called 'pinning points' [Dupont and Alley, 2006]. Loss of buttressing results in faster discharge of grounded ice and retreat of the grounding line [Pritchard and others, 2012]. For example, due to high basal melt rates, the hinge line[7] of PIG retreated at a rate of ~ 1 km a^{-1} between 1992 and 2011 [Park and others, 2013]. Hellmer and others [2012] find that a massive increase in basal melt in the Filchner-Ronne Ice Shelf during the second half of this century is likely, based on ocean models driven by future carbon emission scenarios. The projected ice loss at the base of this ice shelf represents ~ 80 % of the present Antarctic surface mass balance, showing the importance of studying interactions between ice and ocean.

Along with these observations of glacier acceleration and grounding-line retreat, West Antarctica is potentially unstable due to its configuration, with a bedrock below sea level and sloping upward towards the ocean ('retrograde slope'). A marine ice sheet with a grounding line located on such a retrograde bed slope is unstable if the downstream ice shelf is freely floating, i.e. unbuttressed [Weertman, 1974; Thomas and Bentley, 1978; Schoof, 2007a; Joughin and Alley, 2011]. Figure 1.7 illustrates this marine ice-sheet instability, which is valid in flowline mode (where ice-shelf buttressing is not taken into account). In steady state, grounding-line ice flux q (red curve in Fig. 1.7a), which depends on grounding-line ice thickness, matches balance flux[8] ax (blue curve in Fig. 1.7a), i.e. $q = ax$. This occurs at three points in Figure

---

[7]The hinge line is the limit of tidal flexing of the glacier, corresponding to point F in Figure 1.10.

[8]The balance flux is the product of accumulation rate (constant here) and upstream catchment length [Schoof,

1.7: two steady states are stable (green vertical lines in Fig. 1.7a and green curves in Fig. 1.7b) and one steady state is unstable (yellow vertical line in Fig. 1.7a and red curve in Fig. 1.7b). If the grounding line is located on a bed sloping downward towards the ocean (green vertical lines), a perturbation inducing a retreat reduces ice thickness at the grounding line, leading to grounding-line flux lower than balance flux ($q < ax$). This causes the grounding line to advance and come back to its initial position. In the same way, if the grounding line advances, ice thickness increases and grounding-line flux becomes higher than balance flux ($q > ax$), leading to grounding-line retreat. This negative feedback corresponds to a stable steady state. The situation is different if the grounding line is located on a retrograde bed slope (bed sloping upward towards the ocean, yellow vertical line in Fig. 1.7a), where a retreat causes thickness and flux increases at the grounding line, which result in further grounding-line retreat because $q > ax$. Similarly, an advance lowers grounding-line flux so that it exceeds balance flux ($q < ax$), promoting further advance. This positive feedback corresponds to an unstable steady state.

In some specific bed configurations and using a three-dimensional (3D) ice-sheet model that takes into account buttressing effect, stable grounding-line positions are possible on retrograde bed slopes [Gudmundsson and others, 2012], due to ice-shelf buttressing [Gudmundsson, 2013]. Therefore, it is crucial to understand what are the exact mechanisms happening in the vicinity of the grounding line because ice discharge there controls ice-sheet stability. Before focusing on this small and important region in more details, we briefly describe the general laws used in ice-sheet modeling.

1.3   Ice-sheet modeling

Three conservation laws are commonly used in ice-sheet modeling [Primer, 2011]:

- conservation of mass: the time rate of mass change in a control volume equals the mass rate into the volume minus the mass rate out

- conservation of momentum: the time rate of momentum change in a control volume equals the momentum rate into the volume minus the momentum rate out

- conservation of internal energy: the energy retains a constant value in all the changes of the motion form.
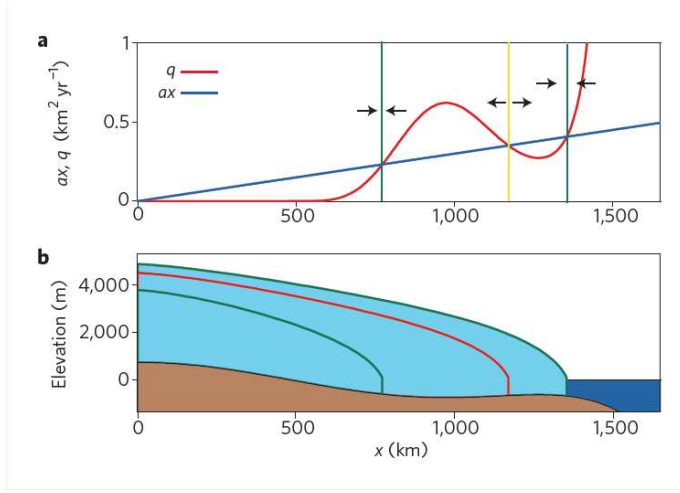
2007a].

Figure 1.7: *(a) Grounding-line flux q (red) and balance flux ax (blue) as a function of horizontal distance x obtained with the parameters of Table 1 in Schoof [2007a]. Vertical lines are steady-state grounding lines (green for stable and yellow for unstable) and arrows indicate likely directions of the grounding line between these steady states. (b) Corresponding steady-state ice sheet profiles (green for stable and red for unstable) [Image credit: Box 2 of Joughin and Alley [2011], adapted from Figure 6 of Schoof [2007a]].*

The balance equations of mass, momentum and internal energy read [Greve and Blatter, 2009]

$$\frac{\mathrm{d}\rho_i}{\mathrm{d}t} = -\rho_i \nabla \cdot \mathbf{v}, \tag{1.1}$$

$$\rho_i \frac{\mathrm{d}\mathbf{v}}{\mathrm{d}t} = \nabla \cdot \boldsymbol{\sigma} + \underbrace{\rho_i \mathbf{g}}_{\text{gravity}} - \underbrace{2\rho_i \boldsymbol{\Omega} \times \mathbf{v}}_{\text{Coriolis}}, \tag{1.2}$$

$$\rho_i \frac{\mathrm{d}e_{si}}{\mathrm{d}t} = -\nabla \cdot \mathbf{f}_h + \underbrace{\mathrm{tr}(\boldsymbol{\sigma} \cdot \mathbf{D})}_{\text{dissipation power}} + \rho_i r, \tag{1.3}$$

where $\mathrm{d}/\mathrm{d}t$ is the material derivative, ρ_i is the ice density, $\mathbf{v}$ is the ice velocity vector, $\boldsymbol{\sigma}$ is the Cauchy stress tensor, $\mathbf{g}$ is the gravitational acceleration, $\boldsymbol{\Omega}$ is the Earth angular velocity, e_{si} is the specific internal energy, $\mathbf{f}_h$ is the heat flux vector, $\mathbf{D}$ is the strain-rate tensor, r is the specific radiation power.

It is often assumed that ice is an incompressible material, so that ice density is constant ($\rho_i =$ const and $\mathrm{d}\rho_i/\mathrm{d}t = 0$). Furthermore, the acceleration $\rho_i \, \mathrm{d}\mathbf{v}/\mathrm{d}t$ and Coriolis terms in equation (1.2) are negligible for ice. Finally, we can insert constitutive equations for internal energy e_{si}, heat flux $\mathbf{f}_h$ and dissipation power $\mathrm{tr}(\boldsymbol{\sigma} \cdot \mathbf{D})$ in equation (1.3)[9]. Then, equations (1.1), (1.2) and

---

[9]These calculations are not detailed here but the curious reader can find the answers to his questions in Greve and Blatter [2009].

(1.3) respectively become

$$\nabla \cdot \mathbf{v} = 0, \tag{1.4}$$

$$\nabla \cdot \sigma + \rho_i \mathbf{g} = 0, \tag{1.5}$$

$$\rho_i c_p \frac{dT}{dt} = \nabla \cdot (k_i \nabla T) + \Phi, \tag{1.6}$$

where c_p and k_i are the heat capacity and thermal conductivity of ice respectively, T is the ice temperature, Φ is the internal frictional heating due to deformation.

Considering a Cartesian coordinate system (x,y,z) with x being the horizontal axis along ice flow, y the horizontal axis transverse to flow and z the vertical axis, and u, v and w being the velocity components in either direction, the mass conservation equation (1.4) can be rewritten as

$$\frac{\partial u}{\partial x} + \frac{\partial v}{\partial y} + \frac{\partial w}{\partial z} = 0. \tag{1.7}$$

Solving the momentum equation (1.5) is quite complex, which is why different approximations are made. The component form of equation (1.5) is detailed in Chapter 2 (Section 2.2.2), along with the different physical approximations. No thermomechanical coupling is performed in this thesis, so the temperature evolution equation (1.6) is not used.

Since ice flow is unaffected by hydrostatic pressure, deviatoric stress components τ_{ij} are used (rather than full stresses):

$$\tau_{ij} = \sigma_{ij} - \frac{1}{3}\delta_{ij}(\sigma_{xx} + \sigma_{yy} + \sigma_{zz}), \tag{1.8}$$

where i and j are indexes corresponding to x, y and z, δ_{ij} is the Kronecker delta ($\delta_{ij} = 1$ if $i = j$ and $\delta_{ij} = 0$ if $i \neq j$).

Glen's flow law [Paterson, 1994] is used as a constitutive equation to relate deviatoric stresses to strain rates

$$\tau_{ij} = 2\eta D_{ij}, \tag{1.9}$$

where the strain rate components are related to velocity gradients through $D_{ij} = (\partial v_i/\partial x_j + \partial v_j/\partial x_i)/2$. The effective viscosity η is given by

$$\eta = \frac{1}{2}A^{-1/n}D_e^{(1-n)/n}, \tag{1.10}$$

where A and n are the Glen's flow coefficient and exponent respectively ($n = 3$ in this study), D_e is the second invariant of the strain-rate tensor.

In the ice-sheet models used in the next chapters, ice velocity is derived from the momentum equation (1.5) taking into account Glen's flow law (1.9) and ice thickness is calculated from equation (1.7). The methodology as well as the different boundary conditions will be detailed
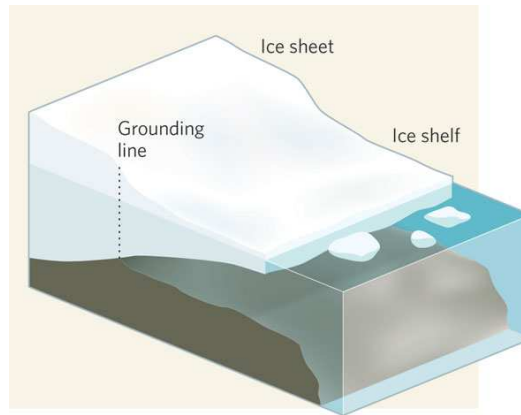
Figure 1.8: *Schematic illustration of a marine ice sheet, such as West Antarctica, with the grounded ice sheet (left), the ice shelf (right) and the grounding line (between both). The ice flows from upper left to lower right [Image credit: Figure 1 of Huybrechts [2009]].*

in the next chapters.

1.4 Modeling grounding-line migration

1.4.1 The grounding line as an interface between ice and ocean

The grounding line[10] is the junction between the grounded ice sheet and the floating ice shelf (Fig. 1.8) and marks the change from inland ice-sheet flow towards ice-shelf flow. Ice from the grounded ice sheet is discharged across the grounding line into ice shelves, from where icebergs break off (calving). In the ice sheet, the ice spreads under its own weight and the main stresses are vertical and basal shear stresses, while in the ice shelf, the ice spreads like a drop of oil on water and longitudinal stress is the force dominating ice flow. These different flow regimes lead to different horizontal ice-velocity profiles in the vertical: in the ice sheet, the velocity is higher at the surface and reduces while approaching the base, whereas in the ice shelf the velocity is almost equal for each vertical layer (Fig. 1.9). In the ice sheet, the ice velocity at the base does not have a zero value in the presence of basal sliding (this occurs if the basal temperature is at the pressure melting point).

At the boundary between both regions, i.e. the grounding line, the two different flow regimes meet (Fig. 1.9). That makes the grounding line a complex and key region in a marine ice sheet. The majority of ice-sheet models determine the grounding-line position by calculating

---

[10]In other languages: 'Ligne d'ancrage' in French (Belgium), 'Ligne d'échouage' in French (France), 'Scharnier lijn' in Dutch, 'Gründungslinie' in German, 'Línea de tierra' in Spanish, 'Linea di galleggiamento' in Italian, 'Linha de encalhe' in Portuguese, 'Grunnlinje' in Norwegian, $\gamma\epsilon\iota\omega\sigma\eta\varsigma\gamma\rho\alpha\mu\mu\eta$ in Greek.
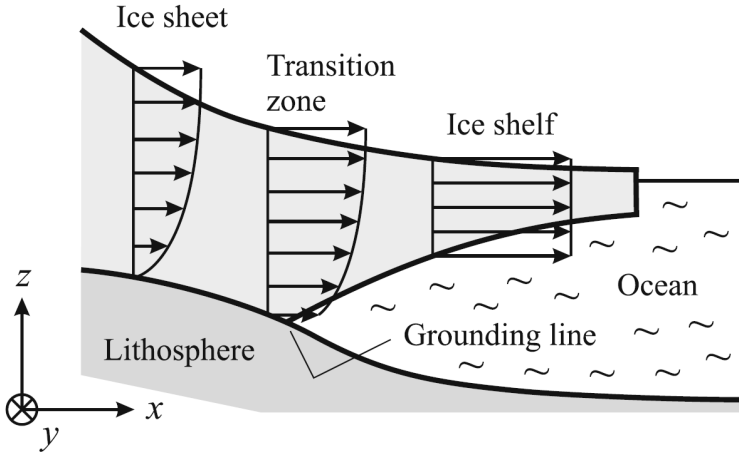
Figure 1.9: *Flow regimes in an ice-sheet/ice-shelf system with corresponding horizontal ice-velocity profiles (Image credit: Figure 6.2 of Greve and Blatter [2009]).*

the floating condition[11]:

$$\rho_i h = \rho_w (z_{sl} - b), \tag{1.11}$$

where ρ_w is the water density, h is the ice thickness, z_{sl} is the sea-level elevation, b is the bedrock elevation. In the ice sheet, the left term of equation (1.11) is higher than the right term, while in the ice shelf the left term is lower.

The zone around the grounding line (called 'grounding zone') is quite complex, as illustrated by Figure 1.10, where G is the grounding line used in this study. The exact length of the grounding zone varies depending on local ice thickness and properties, and local bedrock topography and properties.

1.4.2 Recent advances in grounding-line modeling

As demonstrated in Section 1.2, it is crucial to correctly represent the grounding-line behavior in order to make accurate Antarctic ice-loss projections. In Section 2.2, an overview of ice-sheet models that include grounding-line migration is given [Docquier and others, 2011]. To complete this overview, we mention below different model intercomparisons that have been performed in order to better understand the physical processes operating at the grounding line, as well as independent studies published after Docquier and others [2011] and related to the topic.

In the first intercomparion investigating grounding-line modeling (among other topics), the

---

[11]The full-Stokes model Elmer/Ice uses the contact problem, which will be detailed in Chapter 3.

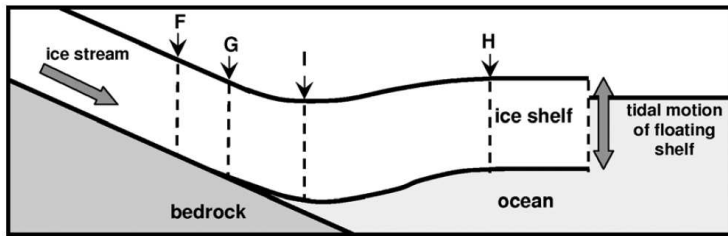**Figure 1.10:** *Schematic illustration of a grounding zone (F-H) as defined by Fricker and Padman [2006]. F is the limit of ice flexure from tidal movement; G is the limit of ice flotation; I is the inflexion point where ice is depressed below the hydrostatic level due to longitudinal stresses associated with the tide-induced bending; and H is the inshore limit of the hydrostatic zone of free-floating ice shelf, or the seaward limit of ice flexure [Image credit: Figure 1 of Fricker and Padman [2006]].*

European Ice Sheet Modeling INiTiative (EISMINT)[12] [Huybrechts and others, 1998], no consensus was reached on how numerical models should react near the grounding line in response to changing boundary conditions of sea level and surface mass balance changes. Furthermore, the intercomparison has not permitted to find out whether the differences in behavior are due to either the physical description of the model or the numerical approach. However, only five models contributed to the grounding-line experiments.

In the meantime, different studies have demonstrated not only the strong possibility of numerical artifacts in marine ice-sheet simulations, but also the importance of grid resolution and accurate representation of the grounding zone [Vieli and Payne, 2005; Pattyn and others, 2006; Hindmarsh, 2006; Schoof, 2007a]. These works are discussed in Chapter 2. They lead to the Marine Ice Sheet Model Intercomparison Project (MISMIP)[13] [Pattyn and others, 2012], which involves 14 flowline ice sheet-ice shelf models (27 realizations) that are compared on the basis of an idealized geometry and spatially-constant parameters. Different numerical approaches (fixed, moving, adaptive grids) and levels of physics (SIA, SSA, HOM, FS[14]) are used in this intercomparison in order to better understand grounding-line migration. Verification is done against a semi-analytical solution [Schoof, 2007a]. The accuracy of the physical approximations involved has not been determined in detail since only one full-Stokes model is involved, and the majority of models use the SSA. The only robust result concerning these approximations is that SIA models that do not include a boundary condition at the grounding line do not pass the tests. More information are provided about numerical approaches in MISMIP: moving grid models are probably the most reliable since no interpolation is involved, and fixed and adaptive grid models need to have sufficiently low grid sizes near the grounding line (several hundreds of meters). Not surprisingly, models that prescribe the flux

---

[12]`http://homepages.vub.ac.be/~phuybrec/eismint.html`.

[13]`http://homepages.ulb.ac.be/~fpattyn/mismip/`.

[14]SIA stands for Shallow-Ice Approximation, SSA for Shallow-Shelf Approximation, HOM for Higher-Order Model, FS for full-Stokes.

at the grounding line give steady-state grounding-line positions in close agreement with the semi-analytical solution since they use the boundary layer theory [Schoof, 2007a], but they do not perform as well in transient state.

The Marine Ice Sheet Model Intercomparison Project for planview models (MISMIP3D)[15] [Pattyn and others, 2013] uses a similar experimental set-up as MISMIP and takes the transverse direction into account. This intercompation includes the results of 17 marine ice-sheet models (33 realizations). Compared to the previous MISMIP, there is a larger spread in the level of physics, with 3 FS models, 1 HOM model (L1L2[16] more exactly), 8 SSA models, 3 hybrid (SIA/SSA) models prescribing the flux at the grounding line. The inclusion of vertical shearing in FS and L1L2 models results in steady-state grounding-line positions further upstream than SSA and hybrid models due to lower effective viscosity. Furthermore, SSA and SIA/SSA models are faster in their response than other models.

The major conclusions of MISMIP and MISMIP3D is that models applied to the Antarctic ice sheet should include longitudinal stresses across the grounding line and need a fine grid resolution in the grounding zone ($<$ 500 m) in order to accurately represent grounding-line migration, which is a necessary condition for projecting sea-level rise.

Beside those intercomparisons, a number of independent studies have been developed in the same time. The Potsdam Parallel Ice Sheet Model (PISM-PIK) [Winkelmann and others, 2011] is a hybrid marine ice-sheet model (SIA/SSA with SSA as a basal sliding condition in grounded regions) that is reversible with a grid size of 1 km but not with 16.6 km according to MISMIP3D results[17] [Pattyn and others, 2013]. However, this model has been improved since MISMIP3D and seems to be reversible with coarser grid sizes [Feldmann and others, submitted]. The validity of PISM-PIK against volume above flotation needs to be tested for this coarse resolution [Drouet and others, 2013; Pattyn and Durand, 2013]. Furthermore, Gladstone and others [2012b] assess the performance of grounding-line parameterizations with their flowline fixed-grid SSA model and show that a grid size of 1 km is enough with this kind of model to accurately simulate grounding-line positions of outlet glaciers such as PIG. The same flowline SSA model is coupled to an ice-shelf cavity circulation model [Olbers and Hellmer, 2010] and predicts a monotonic retreat of the grounding line of PIG over the next 200 years with large uncertainty in the retreat rate [Gladstone and others, 2012a]. Favier and others [2012] use the full-Stokes model Elmer/Ice and show that the contact established between an ice shelf and a pinning point after a sea-level fall is not lost once the sea level is reset to its initial value, indicating a stabilizing effect of the pinning point. Gudmundsson and others [2012] identify stable grounding-line positions on retrograde bed slopes using a 3D SSA model with a specific geometry, showing that marine ice-sheet instability may not exist when the buttressing effect is taken into account. Another study applies a 3D L1L2 model with adaptive mesh refinement

---

[15] http://homepages.ulb.ac.be/~fpattyn/mismip3d/.

[16] L1L2 stands for 'One-Layer Longitudinal Stresses Using D_{xx} at Surface' [Hindmarsh, 2004].

[17] A grid size of 20 km is used by Martin and others [2011] for simulating a dynamic equilibrium of Antarctica with PISM-PIK.

to PIG and shows a rapid deglaciation caused by sub-ice shelf melting [Cornford and others, 2013]. Finally, Jouvet and Graser [2013] superpose SIA and SSA velocity components by including the SIA component in the mass conservation and show that their method is insensitive to local refinements.

1.5   Thesis motivations

The majority of climate models predict warming across most of Antarctica over the next century if greenhouse gas concentrations continue to rise. It is very unlikely that a major disintegration of the Antarctic ice sheet will occur during the next few centuries. However, rapid changes have been observed in the last years over some parts of the continent, which indicates a sensitivity to climatic factors [Turner and Marshall, 2011; Turner and others, 2013]. There is particular concern about the West Antarctic ice sheet that is grounded below sea level. The stability of this ice sheet is strongly linked to the dynamics of the grounding line.

The major aim of this thesis is to improve our understanding of how grounding line migrates through the use of different ice-sheet models. This thesis has been conducted in the same time as MISMIP and MISMIP3D. While these two intercomparison projects encompass a large range of different ice-sheet models, this thesis focuses on finite-difference SSA ice-sheet models, one of them implementing the Schoof [2007a] boundary condition. The models used here are compared to a full-Stokes model and an SSA moving-grid model and verified against the Schoof [2007a] solution. Whereas a series of different studies have been performed on Pine Island Glacier, not many studies have concentrated their efforts on its neighbor, Thwaites Glacier, which is one of the fastest-flowing glaciers in ASE. Thus, one of the SSA models is applied to this glacier to test its grounding-line sensitivity.

The effect of spatial resolution on grounding-line migration is particularly important, so that will be a recurrent theme throughout this thesis. It is necessary to find the 'coarsest' model resolution that can render an accurate grounding-line behavior and a reasonable computation time. In this thesis, the focus is on uncertainties related to grounding-line migration and other uncertainties linked to atmospheric and ocean forcings are not taken into account.

This work is embedded within the European FP7 programme ice2sea (2009-2013)[18], aiming at estimating the contribution of ice sheets and glaciers to sea-level rise. We actively participated in this project through the Sub-Work Package 2.1 ('Grounding-line migration in ice sheet models') and as an early career member of the steering committee. This thesis is funded by the IceCubeDyn Project[19], aiming at studying ice dynamics from IceCube data, a 1 km^3 observatory at South Pole that contains more than 5000 neutrino sensors.

---

[18]`http://www.ice2sea.eu/`.
[19]`http://www.ulb.ac.be/recherche/presentation/fr-arcpattyn.html`.

1.6   Thesis structure

This thesis is composed of five chapters (excluding this introduction and the conclusions), among which two have been published and one has been recently submitted. These three peer-reviewed articles form part of ice2sea project.

Chapter 2, published in *Surveys in Geophysics* [Docquier and others, 2011], provides an overview of ice-sheet models that are used for simulating grounding-line migration. Those models differ through the numerical approach and the physical approximation used, as well as the way the grounding line is treated. Moreover, in that chapter, viscosity perturbations resembling the Marine Ice Sheet Model Intercomparison Project (MISMIP, Pattyn and others [2012]) experiments are performed with finite-difference flowline SIA and SSA models. Steady-state and transient results are discussed and compared to a semi-analytical solution [Schoof, 2007a].

In Chapter 3, which has been published in *The Cryosphere* [Drouet and others, 2013], four flowline ice-sheet models that have different physical and numerical approaches are compared through perturbations in ice-shelf buttressing. The latter is parameterized by modifying the calving front boundary condition. The purpose of those experiments is to analyze the short-term time response of the models and understand where the differences between models come from. Models are compared in terms of grounding-line position, migration rate and ice flux, surface elevation change rate, surface horizontal velocity, volume above flotation. Divergence from the semi-analytical solution [Schoof, 2007a] is also carefully discussed.

Chapter 4 shows results obtained with the same four models as in Chapter 3 but with a series of sea-level perturbations and a slightly different setup. We focus on much larger time scales than in the previous chapter. Initial steady-state ice sheet profiles, grounding-line position, migration rate, ice thickness and ice flux are compared between the four models.

Chapter 5, recently submitted to *Journal of Glaciology* [Docquier and others, submitted], presents the results of a flowline ice stream-ice shelf SSA model used to perform a number of sensitivity experiments applied to Thwaites Glacier (West Antarctica), one of the most remote glaciers in Antarctica. The aim is to analyze the grounding-line sensitivity of this glacier on centennial time scales. The influence of width and buttressing parameterizations is tested.

The analysis of Chapter 5 is extended in three dimensions in Chapter 6 using a 3D ice stream-ice shelf SSA model. The use of such a 3D model permits to directly include the buttressing effect without parameterizing and is useful to understand what the flowline model does not catch in Chapter 5. Different bedrock configurations are tested (full-plane observations, lateral extrusion and bedrock smoothing).

Finally, a summary of all chapters and limitations linked to the models and data is given in Chapter 7. A flow diagram of the thesis structure is depicted in Figure 1.11, where we identify a series of key words for each chapter.
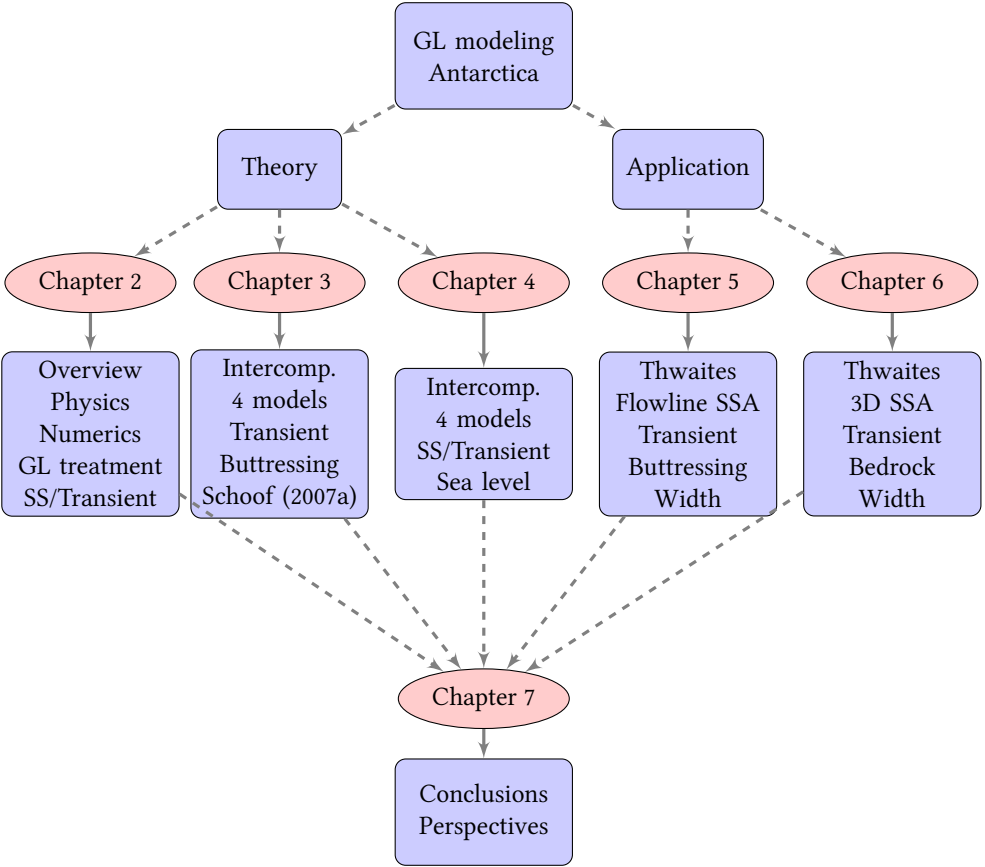
Figure 1.11: *Flow diagram representing the structure of the thesis with a series of key words for each chapter. 'GL' and 'SS' stand for 'grounding line' and 'steady state' respectively.*

2

Representing grounding-line dynamics in numerical ice-sheet models

Recent satellite observations of the Antarctic and Greenland ice sheets show accelerated ice flow and associated ice-sheet thinning along coastal outlet glaciers in contact with the ocean. Both processes are the result of grounding-line retreat due to melting at the grounding line (the grounding line is the contact of the ice sheet with the ocean, where it starts afloat and forms an ice shelf or ice tongue). Such rapid ice loss is not yet included in large-scale ice-sheet models used for IPCC projections, as most of the complex processes are poorly understood.

Here we report on the state-of-the art of grounding-line migration in marine ice sheets and address different ways in which grounding-line migration can be attributed and represented in ice-sheet models. Using one-dimensional ice flow models of the ice sheet/ice shelf system we carried out a number of sensitivity experiments with different spatial resolutions and stress approximations. These are verified with semi-analytical steady-state solutions. Results show that in large-scale finite-difference models, grounding-line migration is dependent on the numerical treatment (e.g. staggered/non-staggered grid) and the level of physics involved (e.g. shallow-ice/shallow-shelf approximation).[1]

Overview
Physics
Numerics
GL treatment
SS/Transient

2.1   Introduction

The West Antarctic Ice Sheet (WAIS) is currently losing ice at a considerable rate [Rignot and others, 2008; Chen and others, 2009; Velicogna, 2009; Rignot and others, 2011]. Pine Island (PIG) and Thwaites Glaciers, situated in the Amundsen Sea Embayment, are the main contributors to this WAIS mass loss [Shepherd and others, 2001]. PIG in particular has shown a nearly continuous acceleration [Joughin and others, 2003] and thinning [Wingham and others, 2009] during recent years. Recent evidence shows that this thinning is due to an inland grounding-line migration from the 1970s to present by 30 km [Jenkins and others, 2010].

Due to its marine configuration, i.e. its bedrock mostly lying below sea level, the stability of the WAIS has been a subject of much debate. Marine ice-sheet stability is mostly controlled by the dynamics of the grounding line, i.e. the junction between the grounded ice sheet and the floating ice shelf. This junction marks the change from inland ice-sheet flow, dominated by vertical shear and basal friction, toward ice-shelf flow, dominated by longitudinal stresses, and which is quintessential in understanding grounding-line dynamics. Weertman [1974] and Thomas and Bentley [1978] proposed that ice discharge through the grounding line should increase with ice thickness. Therefore, a marine ice sheet lying on an upward-sloping bed (toward the ocean), such as WAIS, is unstable. A slight retreat in grounding-line position could therefore lead to an increase in ice thickness, hence increased ice discharge at the grounding line. Ice-sheet thinning is then initiated and further retreat of the grounding line potentially occurs.

Hindmarsh [1993, 1996] argued that ice shelves should have a limited impact on ice-sheet dynamics, and that grounding-line migration is governed by grounded ice flux. He advocated the concept of neutral equilibrium, i.e., that a perturbation in grounding-line position should not lead to unstable retreat or advance for a foredeepened or upward-sloping bed, nor to a return to the original grounding-line position for a downward-sloping bed.

However, Schoof [2007a,b] re-confirmed the instability hypothesis formulated by Weertman [1974] and Thomas and Bentley [1978], on the basis of a boundary layer theory for the ice sheet / ice shelf transition. He demonstrated that (i) marine ice sheets do not exhibit neutral equilibrium, but have well-defined, discrete equilibrium profiles; (ii) steady grounding lines cannot be stable on upward-sloping beds; (iii) marine ice sheets with overdeepened beds can undergo hysteresis under variations in sea level, accumulation rate, basal slipperiness and ice viscosity. Robison and others [2009] confirmed the stability of the grounding line on a downward bed slope comparing fluid-mechanical experiments and model results (with time-dependent evolution of the grounding line), while Durand and others [2009a] demonstrated the instability of marine ice sheets on upsloping beds with a full-Stokes (Elmer/Ice) model.

The aim of this paper is to address the state-of-the-art of modeling the processes affecting marine ice-sheet stability and grounding-line migration. To this end, we give an overview of different numerical approaches and approximations used in ice-sheet models. A description

is given for a simple model that copes with grounding-line migration in a parameterized way. Numerical experiments are carried out to investigate the aspects of grid resolution and the time-dependent behavior and a discussion is given on the appropriate use of approximations and numerical approaches in large-scale ice-sheet models.

2.2 Grounding-line models: an overview

2.2.1 Numerical approaches

There are several numerical approaches in ice-sheet models to simulate grounding-line migration: fixed grid (FG), moving grid (MG) and adaptive techniques. They essentially differ in the way grounding lines are represented. The majority of models make use of the flotation criterion to separate grounded and floating ice:

$$\rho_i h = \rho_w (z_{sl} - b) \,, \tag{2.1}$$

where ρ_i and ρ_w are ice and water densities respectively, h is the ice thickness, z_{sl} is the sea level elevation, b is the bedrock elevation. In FG models, the grounding-line position is not defined explicitly but must fall between grid points where ice is grounded and floating. Large-scale ice-sheet models [Huybrechts, 1990; Ritz and others, 2001] use this strategy to simulate grounding-line migration. Moving grid (MG) models allow the grounding-line position to be followed continuously, i.e., the grounding line coincides exactly with a grid point [Hindmarsh, 1996; Hindmarsh and Le Meur, 2001].

Vieli and Payne [2005] showed that there is a strong dependency of FG models on numerics, that – when perturbed – FG models exhibit large changes in grounding-line migration, and that these changes are irreversible. Conversely, for MG models, changes in grounding-line position are generally small and reversible. However, the models based on shallow-ice approximation used by Vieli and Payne lack a second independent boundary condition that is needed to accurately represent grounding-line migration [see below; Schoof, 2007a; Durand and others, 2009a], and although MG models generally produce more consistent results, a major drawback remains the complexity to implement in a three-dimensional ice-sheet model [Vieli and Payne, 2005].

Adaptive models are a trade-off between FG and MG models. Durand and others [2009a] used the finite-element code Elmer/Ice to couple the Stokes equations with the evolution of two free surfaces, i.e., the upper interface (air/ice) and the bottom interface (ice/bed or ice/sea). They applied a mesh refinement around the grounding line. With this method, the total number of nodes is constant and only the horizontal distribution of the nodes is modified. Durand and others [2009a] need a grid size below 100 m at the grounding line in order to achieve consistent results.

Goldberg and others [2009] used adaptive refinement, i.e. cells are divided into smaller cells where extra resolution is required and groups of cells are coarsened into larger cells in regions where lower resolution suffices. The grounding line is represented either as lying at the boundary between entirely grounded and entirely floating cells or by interpolating the flotation condition between grid lines according to Pattyn and others [2006] (cells can be partially grounded in the latter case). Goldberg and others [2009] found that buttressing was not always sufficient to stabilize an ice sheet, but the collapse of the grounded portion was greatly delayed.

Katz and Worster [2010] presented a theory for grounding-line dynamics in three spatial dimensions. Although they incorporated internal shear and membrane stresses, a Newtonian viscosity was used and basal sliding neglected. They also used the 2D ice shelf proposed by Robison and others [2009], which is valid only when the grounding-line position is independent of the transverse direction.

Finally, FG models can be adapted in such a way that sub-grid grounding-line position and migration can be achieved through local interpolations and approximations. Pattyn and others [2006] determined grounding-line position at sub-grid resolution using the flotation criterion (2.1) and applied a basal friction function to mimic in a continuous way the transition zone between ice sheet and ice shelf. Gladstone and others [2010] used several interpolation schemes in combination with locally increased resolution to suit the same purpose.

2.2.2 Physical approximations

Linear momentum

The flow of an ice body is described by the linear momentum balance equation:

$$\rho_i \frac{d\mathbf{v}}{dt} = \nabla \cdot \boldsymbol{\sigma} + \rho_i \mathbf{g}, \tag{2.2}$$

where $\mathbf{v}$ is the velocity field, $\boldsymbol{\sigma}$ is the Cauchy stress tensor, and $\mathbf{g}$ is the gravitational acceleration. Neglecting acceleration terms and considering the gravitational acceleration only important in the vertical direction, we can write (2.2) in its component form (where x is the flow direction, y is the direction perpendicular to the flow and z is the vertical direction, positively upward):

$$\frac{\partial \sigma_{xx}}{\partial x} + \frac{\partial \sigma_{xy}}{\partial y} + \frac{\partial \sigma_{xz}}{\partial z} = 0, \tag{2.3}$$

$$\frac{\partial \sigma_{yx}}{\partial x} + \frac{\partial \sigma_{yy}}{\partial y} + \frac{\partial \sigma_{yz}}{\partial z} = 0, \tag{2.4}$$

$$\frac{\partial \sigma_{zx}}{\partial x} + \frac{\partial \sigma_{zy}}{\partial y} + \frac{\partial \sigma_{zz}}{\partial z} = \rho_i g. \tag{2.5}$$

Full-Stokes (FS) models [Durand and others, 2009a,b] solve the full system of linear momentum equations. Due to the considerable computational effort, approximations to these equations are often used, such as higher-order, shallow-shelf and shallow-ice approximations. They involve dropping terms from the momentum balance equations and simplifying the strain rate definitions.

Higher-order models (HOM) consider the hydrostatic approximation in the vertical direction by neglecting vertical resistive stresses, so that the linear momentum can be written [Herterich, 1987; Blatter, 1995; Pattyn, 2003]:

$$\frac{\partial \sigma_{xx}}{\partial x} + \frac{\partial \sigma_{xy}}{\partial y} + \frac{\partial \sigma_{xz}}{\partial z} = 0, \tag{2.6}$$

$$\frac{\partial \sigma_{yx}}{\partial x} + \frac{\partial \sigma_{yy}}{\partial y} + \frac{\partial \sigma_{yz}}{\partial z} = 0, \tag{2.7}$$

$$\frac{\partial \sigma_{zz}}{\partial z} = \rho_i g. \tag{2.8}$$

A further approximation, known as the shallow-shelf approximation (SSA), is obtained by neglecting vertical shear [MacAyeal, 1992; MacAyeal and others, 1996]. This is valid for ice shelves and ice streams characterized by a low basal drag:

$$\frac{\partial \sigma_{xx}}{\partial x} + \frac{\partial \sigma_{xy}}{\partial y} = 0, \tag{2.9}$$

$$\frac{\partial \sigma_{yx}}{\partial x} + \frac{\partial \sigma_{yy}}{\partial y} = 0, \tag{2.10}$$

$$\frac{\partial \sigma_{zz}}{\partial z} = \rho_i g. \tag{2.11}$$

For ice streams, an extra basal boundary condition is added, i.e., $\tau_b = \beta^2 u$, where τ_b is the basal shear stress, β^2 is a friction parameter, and u is the horizontal velocity ($\beta^2 = 0$ in ice shelves). The basal sliding law can also take a nonlinear form (see below).

The most common approximation is the shallow-ice approximation (SIA). This approximation incorporates only vertical shear stresses, which is valid for an ice mass with a small aspect ratio (i.e. thickness scale much smaller than length scale) :

$$\frac{\partial \tau_{xz}}{\partial z} = \rho_i g \frac{\partial s}{\partial x}, \qquad \frac{\partial \tau_{yz}}{\partial z} = \rho_i g \frac{\partial s}{\partial y}, \tag{2.12}$$

where τ_{xz} and τ_{yz} are the deviatoric vertical shear stresses and s is the surface elevation. Its main advantage is that all stress and velocity components are locally determined. However, the approximation is not valid for key areas such as ice divides and grounding lines [Hutter, 1983; Baral and others, 2001].

Transition zones

Besides being the limit of flotation, a grounding line is also the change from a shear-dominated ice flow to an ice flow dominated by longitudinal stretching.[2] The transition is never sharp, but gradual, and knowing the size of this transition zone is essential in understanding grounding-line dynamics and inland ice response to sudden changes at the grounding line.

Herterich [1987] calculated the flow within a small transition zone, where the grounded ice sheet is frozen to the bed. The length of the transition zone was found to be of the order of the ice thickness and increased when basal sliding was incorporated. However, the geometry of these experiments was fixed (i.e. no change of the free surface) and the results obtained strongly dependent on this assumption.

Therefore, Lestringant [1994] took in account free-surface changes using a mixed[3] finite-element method to solve the flow equations within two-dimensional sharp transition zones. He concluded that it was *impossible* to use reduced Stokes equations in the transition zone and that the ice sheet and ice shelf could be linked by a jump-boundary condition for the horizontal velocity. However, he assumed no drag effect coming from the sides, which means that the ice shelf does not affect the upstream flow.

Similar conclusions were reached by Pattyn [2000], using a two-dimensional flowline model on a fixed finite-difference grid in order to evaluate the impact of model resolution on ice dynamics near the grounding line. He demonstrated that the transition zone is smaller than the grid size at coarse resolutions (i.e. grid sizes of 20–40 km). At finer resolutions, the transition zone is larger than the grid size, and hence all stress components should be considered. As shown by Pattyn and others [2006], the transition zone length scale is roughly inverse to basal friction as $0 < \beta^2 < +\infty$. Marine ice sheets with large transition zones (low β^2 values), such as ice streams, seem highly sensitive to perturbations at the grounding line or reduction in buttressing compared to ice sheets with small transition zones (high β^2).

Hindmarsh [2004] presented a computational analysis of the accuracy of different approximations to the Stokes equations. He showed that the inclusion of longitudinal (or membrane) stresses increases accuracy at smaller wavelengths compared with the SIA. From his analysis, two longitudinal stress schemes, namely L1L2 (a single-layer scheme, i.e. two-dimensional) and LMLa [a multilayer scheme, i.e. three-dimensional; Pattyn, 2003], are adequate approximations. LMLa is slightly more accurate than L1L2, but the latter has the advantage that it needs less computational effort since it is two-dimensional. Hindmarsh [2006] proposed a boundary layer in these membrane stresses extending about 10 km from the grounding line.

The flow of an ice sheet or a glacier is an example of free surface thin film flow, which can be described by two types of models. Lubrication models are appropriate when shear stresses

---

[2]This is less valid in the case of an ice stream, where upstream of the grounding line longitudinal stress gradients may be dominant

[3]'Mixed' means that the computed unknowns are the horizontal and vertical velocities as well as pressure [Lestringant, 1994]

are dominant in the force balance and in the absence of wall slip. Conversely, membrane models are used in the case of dominant normal stresses and rapid wall slip. However, both rapid and slow slip can occur within the same ice mass (e.g. surges, ice streams). Therefore, hybrid lubrication/membrane models, such as HOM [Blatter, 1995; Pattyn, 2003], have been developed. Schoof and Hindmarsh [2010] established a theory for such hybrid models, what was missing until now. They developed asymptotic expansions for the solution to the Blatter equations in order to obtain a depth-integrated model that describes both fast and slow sliding.

2.2.3 Grounding-line migration

To accurately capture grounding-line migration, it is necessary to resolve the transition zone at a sufficiently fine resolution. Furthermore, besides the flotation criterion (2.1), an extra boundary condition is needed, i.e., longitudinal stresses should be evaluated at both sides of the grounding line. Schoof [2007a] proposed a semi-analytical solution for the ice flux across the grounding line q_g obeying both boundary conditions:

$$q_g = \left[\frac{\overline{A}(\rho_i g)^{n+1}(1 - \rho_i/\rho_w)^n}{4^n C} \right]^{\frac{1}{m+1}} \theta^{\frac{n}{m+1}} h_g^{\frac{m+n+3}{m+1}} , \qquad (2.13)$$

where $\overline{A}$ is the depth-averaged parameter in Glen's flow law, n is the Glen's flow law exponent, C is the basal sliding parameter, m is the basal sliding exponent, θ is the buttressing factor ($\theta = 1$ in this study), and h_g is the ice thickness at the grounding line. This implies that ice flux at the grounding line is sensitive to changes in the ice shelf, contrary to earlier findings by Hindmarsh [1993].

Pollard and DeConto [2009] incorporated this solution in a numerical ice-sheet model at coarse grid resolution by applying a heuristic rule: if the semi-analytical derived flux across the actual grounding line q_g from (2.13) is greater than the modeled flux through the last grounded grid point q_i, then q_g is imposed at that grid point. The velocity at the last grounded grid point u_i is calculated by dividing the analytical flux q_g by the ice thickness at that grid point h_i (derived from the numerical advection scheme). Otherwise, q_g is imposed one grid point further downstream (i.e. the first floating grid point) and the velocity at the first floating grid point u_{i+1} equals the analytical flux q_g divided by the ice thickness there h_{i+1}. The former is usually associated with grounding-line retreat, and the latter usually with grounding-line advance (Fig. 2.1):

$$q_g > q_i \quad : \quad q_i = q_g \quad \text{or} \quad u_i = \frac{q_g}{h_i} , \qquad (2.14)$$

$$q_g < q_i \quad : \quad q_{i+1} = q_g \quad \text{or} \quad u_{i+1} = \frac{q_g}{h_{i+1}} . \qquad (2.15)$$
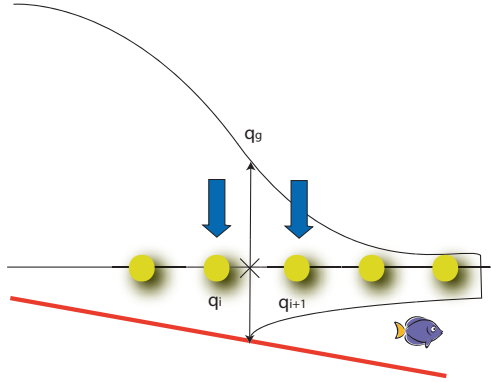
Figure 2.1: *Fixed-grid heuristic rule adapted from Pollard and DeConto [2009].*

The reason why the flux is imposed (and not the velocity) is that the equilibrated solutions in a finite-difference model have the same property as the semi-analytical Schoof solutions: namely, that the upstream snowfall integrated from the grounding line to the ice divide equals the flux across the grounding line. And since the latter is a function of the grounding-line ice thickness [Schoof, 2007a], which in turn depends on the grounding-line position (for a given sea level and bed profile), the equilibrium grounding-line position is determined by the above balance, and is independent of all other model dynamics (as long as the model conserved mass).

Both principles (Schoof boundary condition and Pollard and DeConto heuristic rule) form the base of a simple ice-sheet model developed in the next section.

2.3 A simple grounding-line model

2.3.1 Model description

The numerical ice-sheet model used here is a one-dimensional (vertically integrated) finite-difference flowline model. The grounded part is either based on the shallow-ice approximation (thereby including vertical shear stresses) or the shallow-shelf model (with inclusion of basal friction, i.e. a so-called L1L2 model). In any case, the floating part is according to the shallow-shelf approximation. Therefore, two models are used here, namely SIA/SSA (SIA for the sheet and SSA for the shelf) and SSA (SSA for the whole domain). The depth-averaged horizontal velocity in the ice sheet is calculated as follows:

$$\overline{u} = u_b + \frac{2}{n+2}\overline{A}h\,|\tau_d|^{n-1}\,\tau_d\,, \qquad\qquad (2.16)$$

where $\tau_d = -\rho_i g h \nabla s$ is the driving stress ($\tau_d \equiv \tau_b$ in the case of SIA). Basal velocity u_b is derived from a Weertman-type sliding law:

$$u_b = C^{-\frac{1}{m}} |\tau_d|^{\frac{1}{m}-1} \tau_d.$$ (2.17)

The shallow-shelf (SSA) model neglects vertical shearing and ice deformation is dominated by membrane stresses:

$$4\frac{\partial}{\partial x}\left\{\eta h \frac{\partial \bar{u}}{\partial x}\right\} + \beta^2 u_b = \rho_i g h \frac{\partial s}{\partial x},$$ (2.18)

where

$$\eta = \frac{1}{2}\bar{A}^{-\frac{1}{n}}\left\{\frac{\partial \bar{u}}{\partial x}\right\}^{\frac{1-n}{n}}$$ (2.19)

is the effective viscosity. Due to its depth-integrated nature, it follows that $u_b \equiv \bar{u}$ in (2.18). The basal friction parameter β^2 is then defined as:

$$\beta^2 = \left\{ \begin{array}{ll} C|\bar{u}|^{m-1} & : \quad x < x_g \\ 0 & : \quad x \geq x_g, \end{array} \right.$$

where x_g is the position of the grounding line. A symmetric ice divide is considered at the upstream boundary:

$$\frac{\partial(h+b)}{\partial x} = 0; \qquad \bar{u} = 0.$$

At the downstream boundary (ice shelf/ocean), the longitudinal stress gradient is balanced by the hydrostatic pressure of the ocean water [Paterson, 1994]:

$$\frac{\partial \bar{u}}{\partial x} = \bar{A}\left[\frac{1}{4}\rho g h\left(1 - \frac{\rho_i}{\rho_w}\right)\right]^n.$$ (2.20)

The mass conservation equation is integrated along the vertical to obtain the ice thickness evolution:

$$\frac{\partial h}{\partial t} + \frac{\partial(\bar{u}h)}{\partial x} = \dot{a},$$ (2.21)

where $\dot{a}$ is the accumulation rate.

There are several ways in which grounding-line migration can be treated in a finite-difference model [Gladstone and others, 2010]. One way is to determine the grounding-line position x_g by linear interpolation between the last grounded grid point position x_i and the first floating point x_{i+1} using the flotation criterion expressed in terms of height above flotation $h^\star$, i.e.

$$x_g = x_i - \frac{h_i^\star}{\nabla h^\star},$$ (2.22)

where

$$h_i^{\star} \quad = \quad b_i - z_{sl} + h_i \frac{\rho_i}{\rho_w}, \tag{2.23}$$

$$\nabla h^{\star} \quad = \quad \frac{h_{i+1}^{\star} - h_i^{\star}}{\Delta x}, \tag{2.24}$$

and where Δx is the grid size. Ice thickness at the grounding line h_g is then linearly interpolated from its known position x_g. We enabled grounding-line migration using (2.13) combined with the Pollard and DeConto heuristic rule (2.14) and (2.15).

2.3.2   Numerical implementation

The model was implemented on a fixed finite-difference grid, both in a staggered and a non-staggered version. For the staggered model, velocities are determined between grid points (u-grid), while for the non-staggered version velocities are calculated on the grid points where the ice-sheet geometry is available (h-grid). The mass conservation equation (2.21) is discretized using a semi-implicit scheme and coded as FTCS (forward in time, central in space). This gives for a staggered and a non-staggered grid, respectively

$$h_{i,t+1} \quad + \quad \frac{\Delta t}{2\Delta x} \left[u_{i+\frac{1}{2}} \left(h_{i+1,t+1} + h_{i,t+1} \right) - u_{i-\frac{1}{2}} \left(h_{i-1,t+1} + h_{i,t+1} \right) \right]$$
$$= \quad h_{i,t} + \dot{a}\Delta t \tag{2.25}$$

$$h_{i,t+1} \quad + \quad \frac{\Delta t}{2\Delta x} \left[u_{i+1} h_{i+1,t+1} - u_{i-1} h_{i-1,t+1} \right] = h_{i,t} + \dot{a}\Delta t \tag{2.26}$$

where indices $i = 1 : N$ are the grid nodes along the flowline, and index t denotes time. For the SIA model, (2.25)–(2.26) are written as a diffusive equation (see Huybrechts and others [1996] for a more detailed description and discussion). However, the combined diffusive-advective equations lead to mass loss across the grounding line with the non-staggered model, which is not the case with the staggered model, where mass is always conserved along the whole flowline irrespective of the physical model (SIA/SSA or SSA). The effect of mass loss across the grounding line is discussed in Pattyn and others [2006] and has been shown to have no qualitative impact on grounding-line migration.

2.3.3   Experiments

Vieli and Payne [2005] showed that marine ice-sheet FG models were highly sensitive to horizontal grid size. Large grid sizes, for instance, prevent grounding-line migration. Only small enough grid sizes lead to grounding-line advance [Huybrechts and others, 1998; Vieli and Payne, 2005; Durand and others, 2009b]. To test the grid size sensitivity, we carried out model experiments with different grid sizes, i.e. 50, 25, 12.5, and 5 km as well as for different

physical approximations (SIA/SSA and SSA) and numerical approaches (staggered and non-staggered grids). We compared our model results to the semi-analytical solution derived by Schoof [2007a].

The first experiment is a MISMIP variant[4] [Schoof and others, 2007]. A steady-state geometry is developed on a linearly downward-sloping bedrock defined by

$$b(x) = -100 - x, \tag{2.27}$$

where b is bedrock elevation (m a.s.l.) and x is distance from the ice divide (km). Other parameters and constants are given in Table 2.1. In the standard experiment, a value for Glen's flow law parameter of $A = 10^{-25}$ Pa^{-n} s^{-1} is used. A steady state is achieved after $\sim$40 000 years of integration. Starting from this steady-state configuration (further addressed to as **initial** state), the value for A is decreased (increasing viscosity), leading to an advance of the grounding line. This process is repeated for subsequent changes in A, ranging from 10^{-25} to 10^{-26} in steps of 2×10^{-26}, as well as the reverse process (starting from $A = 10^{-26}$ and decreasing the viscosity in steps of 2×10^{-26}). Each of these step changes takes $\sim$20 000 years to reach a steady state. What is referred to below as **final** state, is the steady state after complete advance and retreat and for the value of $A = 10^{-25}$ Pa^{-n} s^{-1}.

The second experiment corresponds to MISMIP Experiment 3a, where a steady-state geometry is allowed to develop on an overdeepened polynomial bedrock, defined by

$$b(x) = 729 - 2184.8 \times \left(\frac{x}{750 \text{ km}}\right)^2 + 1031.72 \times \left(\frac{x}{750 \text{ km}}\right)^4 -$$
$$151.72 \times \left(\frac{x}{750 \text{ km}}\right)^6. \tag{2.28}$$

The flow parameter A is varied stepwise between 3×10^{-25} and 2.5×10^{-26} Pa^{-n} s^{-1}. Other parameters are similar to those of the previous experiment, except for the domain length, taken as $L = 1800$ km and the basal sliding parameter set to $C = 7.624 \times 10^6$ Pa s^m m^{-m}.

In the third experiment, we used the same linearly downward-sloping bed (2.27) and same constants as in the first experiment above (Table 2.1). We started from an initial steady-state ice sheet with $A = 10^{-25}$ Pa^{-n} s^{-1}. The bulk viscosity of the ice sheet was increased by setting $A = 4 \times 10^{-26}$ Pa^{-n} s^{-1}, leading to a grounding-line advance, until a new steady state was reached. Subsequently, the viscosity was decreased by setting $A = 10^{-25}$ Pa^{-n} s^{-1}, invoking a grounding-line retreat to the initial state.

A major drawback of the Schoof solution is its validity restricted to steady-state solutions and not to transient states. However, grounding-line migration rate is a major issue when trying to understand marine ice-sheet response over decadal time scales (as needed in IPCC projections). The transient response of the grounding line should therefore be independent

---

[4]MISMIP: Marine Ice Sheet Model Intercomparison Project; `http://homepages.ulb.ac.be/~fpattyn/mismip/`

Table 2.1: *Constants and parameter settings for the first, third and fourth experiments*

Parameter	Description	Value	Unit
ρ_i	Ice density	900	kg m^{-3}
ρ_w	Water density	1000	kg m^{-3}
g	Gravitational acceleration	9.8	m s^{-2}
n	Glen's flow law exponent	3	
a	Accumulation rate	0.3	m a^{-1}
L	Domain length	1000	km
C	Basal friction coefficient	10^7	Pa s^m m^{-m}
m	Basal friction exponent	1/3	

of numerical parameters, such as grid resolution and time step, and should be coherent with theoretical developments. Therefore, we performed a fourth experiment to investigate the time-dependent response by evaluating ice fluxes across the grounding line with theoretical values (i.e. Schoof solution) and grounding-line migration rate during grounding-line advance and retreat for a staggered SSA model. We used the same setup and parameters as the third experiment above (i.e. linearly downward-sloping bed), except that we used 5 values of rate factor A instead of 3 in order to compare the transient behavior with the same viscosity for the advance and the retreat. These values are respectively $10^{-25}, 4 \times 10^{-26}, 10^{-26}, 4 \times 10^{-26}$ and 10^{-25} Pa^{-n} s^{-1}.

2.4   Results

2.4.1   Effect of grid resolution on steady-state grounding-line position

Downward-sloping bed

Figure 2.2 shows the steady-state profiles of the ice sheet and ice shelf along the flowline for both the linearly downward-sloping and the overdeepened bedrock profiles (staggered SSA model). Grounding-line advance is obtained when decreasing the value of A, and a retreat is invoked when A is increased to its initial value. Advance and retreat steady-state profiles are hardly discernible, as both are lying close together. According to theory [Schoof, 2007a], they should overlap, which defies neutral equilibrium of grounding-line positions.

When analyzing the differences between final (after perturbation of A) and initial steady-state grounding-line positions as well as the differences between final steady-state grounding-line positions and Schoof semi-analytical solution for the whole suite of grid resolutions as well as for the different physical and numerical approximations, it becomes clear that staggered grid models perform generally well in reproducing advance and retreat of the grounding line

(a) Downward-sloping bed

(b) Overdeepened bed

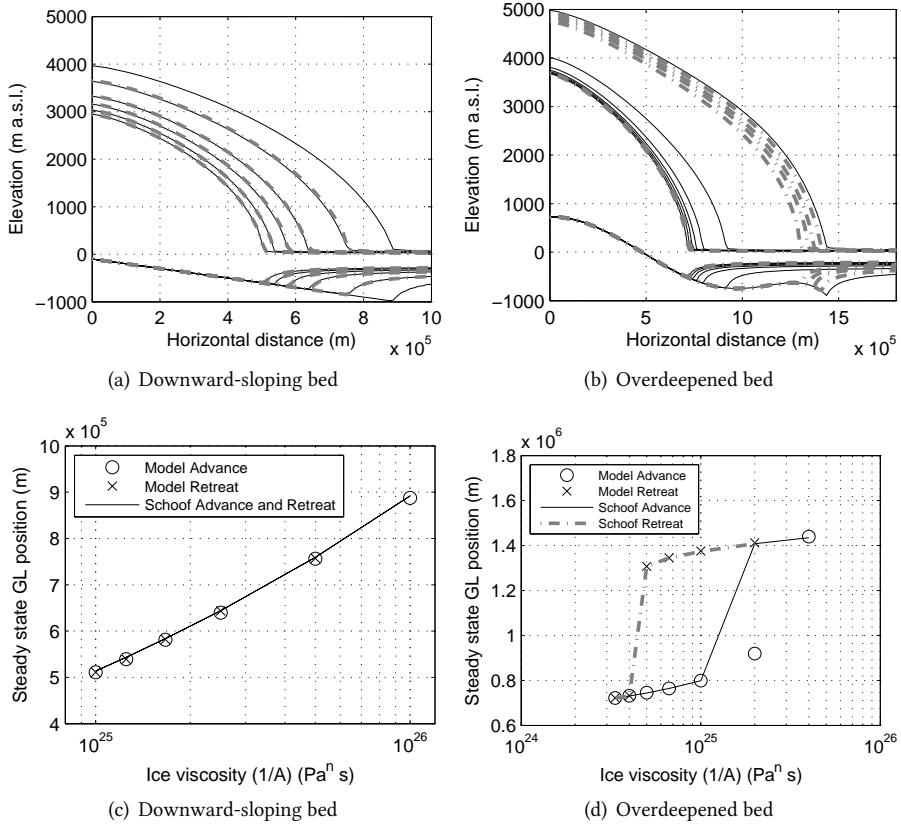(c) Downward-sloping bed

(d) Overdeepened bed

Figure 2.2: *Steady-state profiles (solid black curve: advance; dashed gray curve: retreat) of the ice sheet on a downward-sloping bed (a and c) and on an overdeepened bed (b and d) for the SSA model on a staggered grid (first and second experiments). Grid size is 12.5 km in both cases. GL means 'grounding line'.*

with high accuracy (Table 2.2). Especially the SSA staggered grid model displays differences between grounding-line positions of the order of meters to tens of meters, which is a fraction of the grid size. Furthermore, there is no apparent relation between the accuracy and grid resolution. The same conclusions can be drawn for the SIA/SSA staggered grid model, albeit that differences are an order of magnitude larger, but still small compared to the grid size. The non-staggered grid model, on the contrary, shows the largest discrepancies in which differences are of the order of magnitude of the grid size (and therefore decreasing with decreasing grid size). Similar tests were also performed with staggered SSA and SIA/SSA models that do not include the Schoof boundary condition (not shown). They also reveal large discrepancies between the advance and retreat steady-state positions and in the majority of the experiments the grounding line hardly retreats when A is set to its initial value.

In summary, all staggered grid models that are forced with the Schoof boundary condition converge to the same steady-state grounding-line position irrespective of the horizontal grid size used. Models that are either non-staggered or do not include the boundary condition converge only to the same advance-retreat position for sufficiently small grid sizes, which is considered a deficiency of fixed-grid finite-difference models [Vieli and Payne, 2005; Durand and others, 2009b; Gladstone and others, 2010]. Results also depend on model type, i.e. the SSA model gives better results (difference between final and initial grounding-line positions is less) compared to SIA/SSA (Table 2.2).

Even though modeled grounding-line position is unique for each set of parameter values, deviations from the Schoof semi-analytical solution may occur. These differences decrease with decreasing grid size (Table 2.2). Since the Schoof semi-analytical solution is based on boundary layer theory, these positions do not necessarily have to coincide with the steady-state positions for the different model types, as other physics are involved. Nevertheless, the difference is not more than a couple of kilometers for the staggered grid models, since all models are forced with the boundary condition from Schoof [2007a]. In concordance with the above results, SIA/SSA models show a larger deviation from the Schoof solution and the non-staggered model deviates with several tens of kilometers.

Overdeepened bed

For an overdeepened bed, multiple steady states occur for the same value of A as a function of the initial geometry of the ice sheet. This is due to the fact that no steady states are found on upward-sloping beds [Schoof, 2007a], leading to hysteresis (Figures 2.2(b) and 2.2(d)). In general, conclusions reached in Section 2.4.1 are also valid here, i.e. initial and final grounding-line positions show differences of the order of meters to tens of meters with the staggered SSA model, while large deviations – also related to grid size, occur for either SIA/SSA and non-staggered grid models (not shown).

Table 2.2: *Absolute differences between final (after perturbation of A) and initial steady-state grounding-line (GL) positions ($\Delta FI = |GL_{\text{Final}} - GL_{\text{Initial}}|$) and absolute differences between final steady-state GL positions and Schoof semi-analytical solution ($\Delta FS = |GL_{\text{Final}} - GL_{\text{Schoof}}|$) as a function of grid size for the SSA staggered grid model, SIA/SSA staggered grid model and SIA/SSA non-staggered grid model. Instead of performing only one model run per grid size, we performed a series of model runs for a 'nominal' grid size in which the initial grid size was slightly altered by adding/subtracting 1 or 2 grid points for the whole flowline, thereby keeping the flowline length constant. Standard deviation (σ) is indicated in brackets. These results correspond to the third experiment (linearly downward-sloping bedrock and 3 A values).*

Physical approx.	Grid type	Grid size (m)	Runs	ΔFI (σ) (m)	ΔFS (σ) (m)
SSA	staggered	50000	4	3.17 (3.74)	7020 (3018)
SSA	staggered	25000	4	28.01 (38.05)	4567 (1287)
SSA	staggered	12500	4	6.54 (9.27)	3194 (793)
SSA	staggered	5000	2	0.94 (0.32)	2015 (231)
SIA/SSA	staggered	50000	2	127.39 (116.48)	9616 (1405)
SIA/SSA	staggered	25000	2	165.26 (36.83)	5750 (476)
SIA/SSA	staggered	12500	1	65.57 (0)	2905 (0)
SIA/SSA	non-staggered	50000	5	58610 (15388)	73243 (8378)
SIA/SSA	non-staggered	25000	5	25901 (7974)	54154 (4602)
SIA/SSA	non-staggered	12500	5	8983 (2367)	43904 (2365)
SIA/SSA	non-staggered	5000	5	1413 (1144)	37529 (712)

2.4.2 Grounding-line migration rate

Figure 2.3 displays the grounding-line flux as a function of time during the advance (Figure 2.3(a)) and the retreat (Figure 2.3(b)) compared to the flux determined from (2.13). Since the value of rate factor A is the same for both advance and retreat, the ice flux converges towards the same value in Figures 2.3(a) and 2.3(b). Both solutions show a series of distinct jumps in time that are mainly due to the intrinsic discrete nature of the heuristic rule in (2.14)-(2.15), which causes flips between grid points for arbitrarily small changes of ice flux. These discrete steps cannot be removed despite the interpolating grounding-line function (2.22). For an advancing ice sheet, the difference between the modeled and semi-analytical fluxes is relatively small. However, during retreat sudden high amplitude increases in grounding-line flux occur with the SSA model. The peaks can be visualized in more detail in Figure 2.3(d), where ice fluxes are plotted against grounding-line ice thickness. Nevertheless, after these jumps the modeled fluxes converge toward the fluxes determined from (2.13). Since the Schoof flux given by (2.13) is valid for steady-state conditions and derived from boundary layer theory, deviations from this semi-analytical flux during a transient state do not indicate whether the model results are pertinent or not.

A sound way of evaluating grounding-line migration rate is to compare the migration rate obtained with the model with the one calculated from differentiating the flotation criterion [Hindmarsh, 1993], i.e.

$$\frac{\mathrm{d}x_g}{\mathrm{d}t} = -\frac{\dot{a} - \frac{\partial q}{\partial x}}{\frac{\partial h}{\partial x} + \frac{\rho_w}{\rho_i}\frac{\partial b}{\partial x}} \tag{2.29}$$

We solved (2.29) numerically by calculating both the flux divergence and the thickness gradient with a three-point upstream difference scheme centered on the sub-grid grounding-line position x_g (Figures 2.3(e) and 2.3(f)). A distinction is made based on the heuristic rule (2.14) or (2.15). Circles in the scatterplot correspond to the case where the grounding-line flux is larger than the flux obtained from (2.13), generally leading to a grounding-line advance. Crosses correspond to the inverse case (grounding-line flux smaller than the flux obtained from (2.13)). For both advance and retreat experiments, grounding-line changes in either direction occur, albeit that negative migration rates are generally absent for the advancing case (Figure 2.3(e)).

In general there are many more 'retreat' points (crosses) than there are 'advance' points (circles). The heuristic rule compares the modeled ice flux to the theoretical flux and adapts the modeled velocity field accordingly. Any 'advance' flux condition will alter the flow field considerably, and result in an important change in grounding-line position as well as in glacier geometry. However, during the following time steps the flux at the grounding line will be too low compared to the theoretical one and slight adjustments to the jump in grounding-line position are made (retreat), to compensate for the larger initial jump. These changes happen evidently on sub-grid level, leading to a negative migration rate. Therefore, during an advance phase, small 'retreat' changes can be observed, simply to counterbalance large changes due to the imposition of the grounding-line flux. This also explains why during an advance
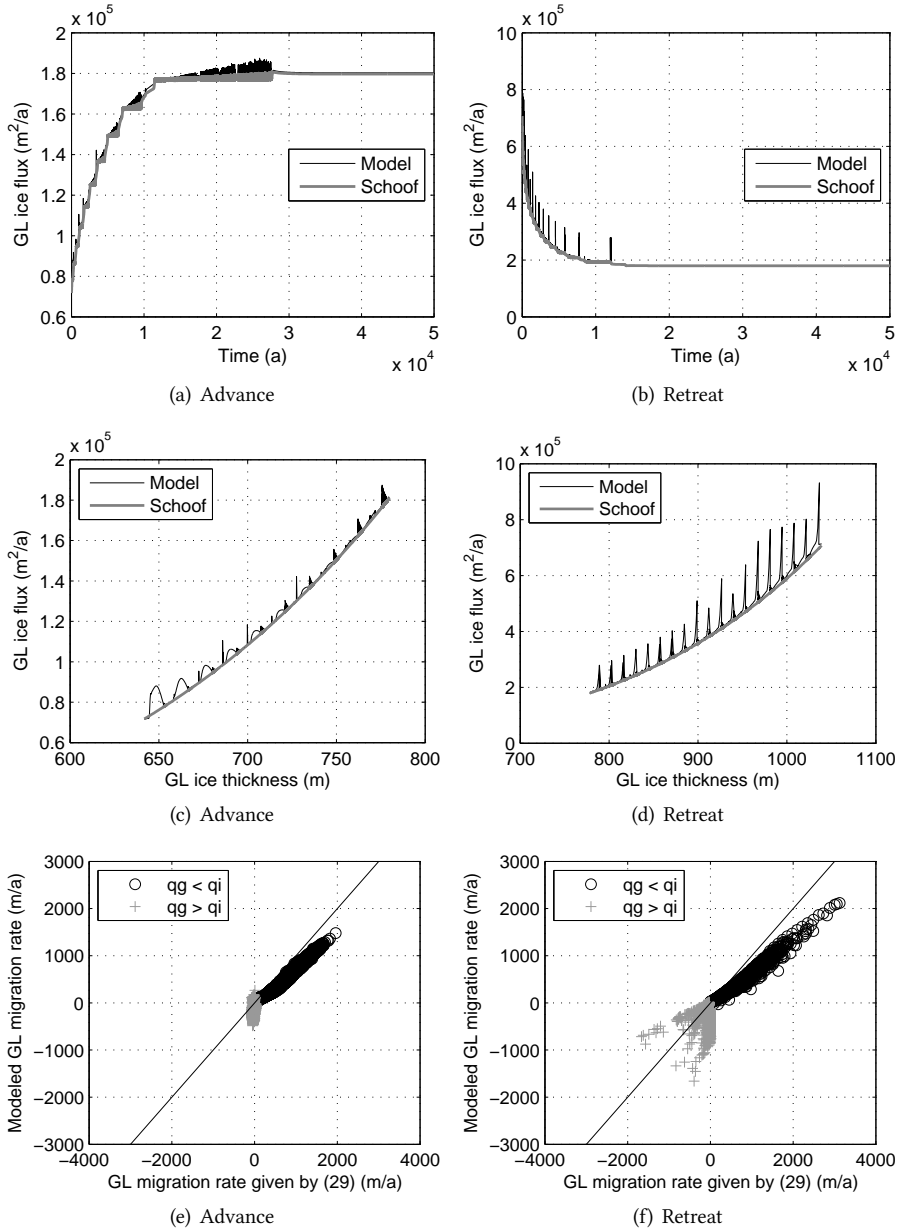
Figure 2.3: *Modeled grounding-line (GL) flux compared to Schoof GL flux as a function of time (a and b) and GL ice thickness (c and d) (fourth experiment). Modeled GL migration rate (dx_g/dt) is also plotted against GL migration rate given by (2.29). Left plots show the advance stage (A decreases from 10^{-25} to 4×10^{-26} Pa^{-n} s^{-1}), while right plots show the retreat stage (A increases from 10^{-26} to 4×10^{-26} Pa^{-n} s^{-1}). Grid size is 12.5 km.*

phase small episodes of grounding-line retreat can be observed, while according to theory, this should be zero (Figure 2.3(e)). Both Figures 2.3(e) and 2.3(f) show that modeled advance rates correspond well with the theoretical value, but are slightly underestimated, while the modeled retreat rates show a larger discrepancy, probably related to this so-called counterbalancing effect.

A similar experiment was carried out for a smaller grid size (6.25 km, Figure 2.4). The behavior is coherent in the sense that due to the higher resolution, jumps in grounding-line flux occur more often, but they are of smaller amplitude. The comparison of modeled grounding-line migration rates with the calculated ones leads to a similar graph as in the previous experiment. Migration rates are comparable and invariant for the grid size applied, albeit slightly lower than those determined from (2.29).

2.5   Discussion and Outlook

Representing grounding-line migration in numerical ice-sheet models remains an arduous task, not only because of the complexity of the physics involved (change from shear dominated flow to flow dominated by longitudinal pulling or stretching), the geometry of the problem (a grounding line is difficult to identify within a numerical model as it does not always coincides with a grid node), the computational challenge (solving a complex set of equations on a high-resolution mesh), but also the difficulty to observe and attribute the process of grounding-line migration due to different interacting mechanisms, such as sub-shelf melting, loss of buttressing, inland ice flow acceleration due to basal sliding, ice thinning, etc. All these processes may cause grounding-line retreat, but a number of them are at the same time a result of grounding-line retreat as well, hence leading to a series of feedbacks. Therefore, observations alone are not sufficient to disentangle the mechanisms involved. Nowadays, the gap in our understanding has been filled by advances in time-dependent observations, numerical modeling and tools for model verification.

Only recently the debate on grounding-line stability has moved onto the next level with the mathematical proof on grounding-line steady-state position as a function of ice flux and topography [Schoof, 2007a], leading to a verification and intercomparison exercise for numerical ice-sheet models [Schoof and others, 2007]. In this paper we compared numerical results obtained with simple ice-sheet models against the semi-analytical solutions proposed by Schoof and others [2007], revealing the necessity of having numerical models with sound numerical treatments and proper physical approximations. Although the semi-analytical solution is only valid for steady states, the transient behavior of the model has been analyzed by different means.

The results presented in this paper are obtained with a couple of simple ice sheet/ice shelf models that capture the essence of grounding-line migration by including the heuristic rule proposed by Pollard and DeConto [2009]. The latter assures that modeled grounding-line
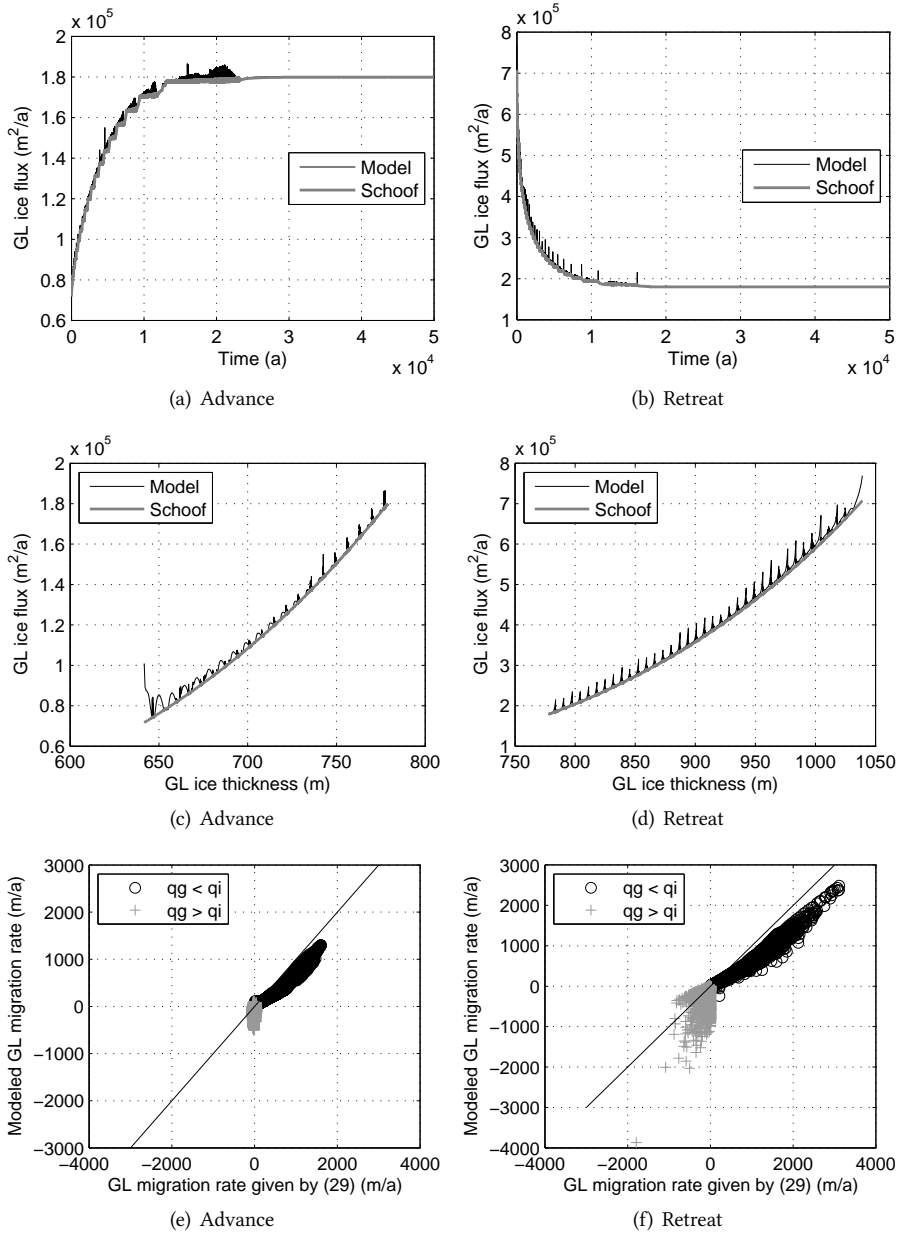
Figure 2.4: *Same as figure 2.3 with a grid size of 6.25 km.*

positions are in accord with the steady-state grounding-line positions given by Schoof [2007a]. Ice-sheet models on a staggered grid perform well and lead to high accuracy on steady-state grounding-line position (comparing advancing to retreating ice sheets). Non-staggered grid models lead to larger differences and accuracy increases with decreasing grid size. This poorer performance may be related to mass loss occurring at the grounding line while coupling a diffusive with an advective scheme, as discussed in Pattyn and others [2006].

The time-dependent response of these models remains influenced by the parameterization scheme of grounding-line migration, leading to sudden changes in grounding-line ice flux whenever a jump from one grid point to another occurs, despite the sub-grid representation of grounding-line position in the model. However, the bulk response in grounding-line migration rate is coherent when compared with those expected from differentiating the flotation criterion at the grounding line [Hindmarsh, 1993], albeit that modeled migration rates are generally underestimated.

A major drawback of the models presented in this paper is their limitation along a flow-line. Although buttressing effects can be included in a parameterized way [Vieli and Payne, 2005; Pattyn and others, 2006], real three-dimensional effects are lacking. A number of three-dimensional models that cope with grounding-line migration in a verified way have been developed or are in the process of development [Pollard and DeConto, 2009; Goldberg and others, 2009; Robison and others, 2009; Katz and Worster, 2010], where the Pollard and De-Conto model incorporates the heuristic rule as in the above experiments. A more detailed comparison with higher-order and full-Stokes models should be carried out in order to remove any bias towards the use of such types of models. International efforts, such as *ice2sea*[5] or *SeaRISE*,[6] are pushing the ice-sheet model community to developing better and physically-based numerical ice-sheet models for future sea-level change projections. Once such models are fully available, a physically-based assessment will be possible, making the use of selective grounding-line migration scenarios obsolete.

2.6   Supplementary information

The supplementary information below was not published in the article.

2.6.1   Staggered grid

On a staggered grid, the velocity components are stored at the cell faces and the scalar variables, such as ice thickness and viscosity, are stored at the central nodes (Fig. 2.5). This is

---

[5]ice2sea is a science programme that is funded by the European Union Framework-7 scheme and will improve projections of the contribution of ice to future sea-level rise, `http://www.ice2sea.eu`

[6]SeaRISE (Sea-level Response to Ice Sheet Evolution) is a community organized effort to estimate the upper bound of ice-sheet contributions to sea level in the next 100–200 years, `http://websrv.cs.umt.edu/isis/index.php/ SeaRISE_Assessment`
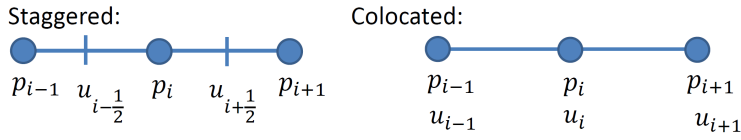
Staggered:

p_{i-1} $u_{i-\frac{1}{2}}$ p_i $u_{i+\frac{1}{2}}$ p_{i+1}

Colocated:

p_{i-1} p_i p_{i+1}
u_{i-1} u_i u_{i+1}

Figure 2.5: *Schematic illustration of staggered (left) and collocated (right) grids, where p is the scalar variable (e.g. ice thickness) and u is the velocity [Image credit: C. Batty [2011], Columbia University,* `http://www.cs.columbia.edu/~batty/teaching/general/Fluids2.pdf`*, 26/06/2013]/*

different from a collocated grid arrangement, where all variables are defined at the same location at the central nodes. Even if more complicated to implement, a staggered grid allows for more accurate formulation of partial differential equations (such as Stokes and continuity equations) with finite differences [Morinishi and others, 1998]. It is a simple way to avoid odd-even decoupling between scalar variables and velocity, a discretization error that can occur on collocated grids and lead to unstable, high frequency errors in velocity. In brief, a staggered grid is numerically more stable than a collocated grid.

2.6.2 No heuristic rule

Not using the heuristic rule at the grounding line [Schoof, 2007a; Pollard and DeConto, 2009] gives results that strongly depend on the model grid size. Figure 2.6 shows the initial steady-state grounding-line positions provided by the SSA staggered grid model without the heuristic rule for different grid sizes by performing the third experiment of this chapter. These results were not shown in Docquier and others [2011].
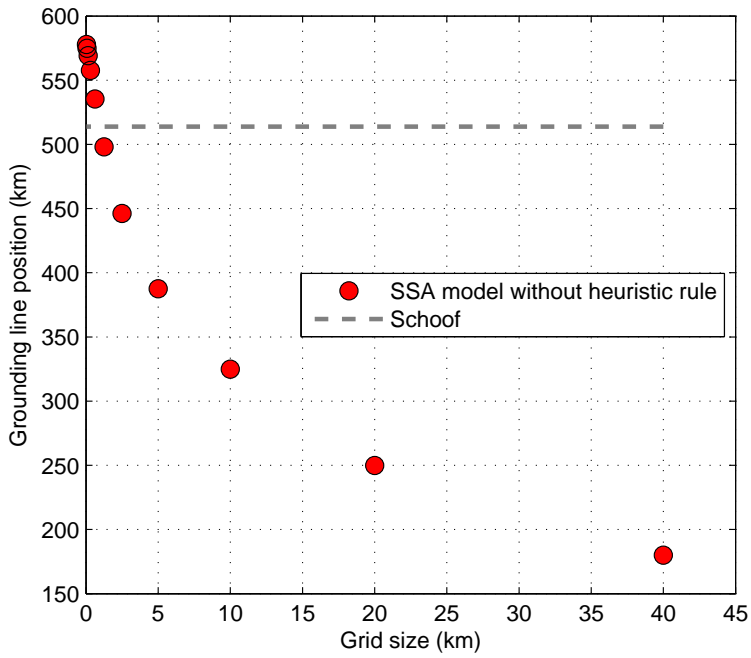
Figure 2.6: *Initial steady-state grounding-line position as a function of grid size (results of the third experiment) with the SSA staggered grid model (without heuristic rule).*

3

Grounding-line transient response in marine ice-sheet models

Marine ice-sheet stability is mostly controlled by the dynamics of the grounding line, i.e., the junction between the grounded ice sheet and the floating ice shelf. Grounding-line migration has been investigated in the framework of MISMIP (Marine Ice Sheet Model Intercomparison Project), which mainly aimed at investigating steady-state solutions. Here we focus on transient behavior, executing short-term simulations (200 years) of a steady ice sheet perturbed by the release of the buttressing restraint exerted by the ice shelf on the grounded ice upstream. The transient grounding-line behavior of four different flowline ice-sheet models has been compared. The models differ in the physics implemented (full-Stokes and Shallow-Shelf Approximation), the numerical approach, as well as the grounding-line treatment. Their overall response to the loss of buttressing is found to be broadly consistent in terms of grounding-line position, rate of surface elevation change and surface velocity. However, still small differences appear for these latter variables, and they can lead to large discrepancies ($> 100\%$) observed in terms of ice-sheet contribution to sea level when cumulated over time. Despite the recent important improvements of marine ice-sheet models in their ability to compute steady-state configurations, our results question the capacity of these models to compute short-term reliable sea-level rise projections.[1]

Intercomp. - 4 models
Transient - Buttressing
Schoof (2007a)

3.1   Introduction

A range of observational methodologies have shown that significant loss of Antarctic ice mass has occurred over the past decade [Wingham and others, 2006; Rignot and others, 2008; Velicogna, 2009; Rignot and others, 2011; Pritchard and others, 2012]. Increased basal melt of ice shelves appears to be the primary control on Antarctic ice-sheet loss. Its resultant thinning induces a reduction of the buttressing force, i.e. the mechanical effect of the ice shelf on the state of stress of grounded ice, which leads to an acceleration of outlet glaciers [Rignot and others, 2008; Pritchard and others, 2012]. The dynamical response of the grounding line (GL), where ice loses contact with bed and, downstream, begins to float over the ocean, is an essential control on the mass balance of a marine ice-sheet. In particular, a rigorous mathematical description of the long-standing hypothesis of marine ice-sheet instability [Weertman, 1974] has been recently given by Schoof [2007a], for a flowline type ice sheet without buttressing.

While observations are crucial in diagnosing the state of balance of an ice sheet, extrapolation of current trends is a limited technique in predicting ice-sheet future behavior. Ice-sheet models are therefore the central tool in forecasting the evolution of ice masses and, more particularly, their future contribution to the ongoing sea-level rise (SLR). A large suite of ice sheet models has been developed in recent years. Increasing complexity has been regularly added, enabling progressive improvements from 1D flowline models based on shallow ice approximations to full numerical solutions of the Stokes equations for an actual 3D geometry [Morlighem and others, 2010; Gillet-Chaulet and Durand, 2010; Larour and others, 2012; Gillet-Chaulet and others, 2012]. However, implementing GL migration in ice flow models still represents a challenge to be faced by the community of ice sheet modellers [Vieli and Payne, 2005; Pattyn and others, 2012, 2013].

As mentioned above, Schoof [2007a] developed a boundary-layer theory establishing the relation between ice flux and ice thickness at the GL, which can be implemented as a boundary condition in ice-flow models. The boundary layer is a zone of acceleration, generally a few tens of kilometres in extent [Hindmarsh, 2006; Schoof, 2007a] for high-slip cases such as we consider, where the stress regime adjusts from being shear-dominated to extension-dominated. This theoretical development demonstrated the uniqueness of steady solutions of marine ice sheets resting on a downward sloping bedrock and their unstable behavior on an upward sloping region. Based on the Schoof [2007a] results, an intercomparison effort compared the behavior of the GL evolution of 26 different models on a flowline, as part of the Marine Ice Sheet Model Intercomparison Project [MISMIP, Pattyn and others, 2012], which was essentially designed to compare models with the semi-analytical solution proposed by Schoof [2007a]. However, Schoof's flux formula is derived on the assumption of near-steady-state, and its ability to represent transient behavior has not been fully investigated. This issue was briefly touched upon during the MISMIP experiments [Pattyn and others, 2012], but it was not the primary focus of investigation.

The MISMIP experiments showed a broad range of behavior of numerical implementations

in response to an instantaneous global change of the ice rheology, with some quantitative consistency between different numerical formulations. The MISMIP experiments highlighted, along with Schoof's studies, the importance of obtaining high accuracy in the numerical solution in the boundary layer near the GL, which in practice means the use of high resolution or high accuracy methods, which has the consequence that the numerical approach used is of significant issue.

Short term predictions of rapid change in the Antarctic Ice Sheet necessarily involve transient processes, and the ability of marine ice-sheet models to represent these requires quantification. Therefore, we conduct a model intercomparison dealing with rapid change in order to evaluate the transient behavior of different models. A particular aim is to investigate the divergence of ice-sheet models from the Schoof [2007a] solution during these very short time scale processes. Furthermore, owing to the use of different physical approximations and numerical approaches, we expect that the same experiment carried out with different ice-sheet models may give different results. Therefore, another aim of this study is to quantify these differences and understand their origin.

In contrast to the original MISMIP experiment, here we choose to investigate the physically more reasonable transient forcing of a decrease in ice-shelf buttressing. This is implemented by means of a flowline model with grounded part and a floating ice shelf. As is common with previous studies [Nick and others, 2009; Price and others, 2011; Williams and others, 2012], buttressing is implemented by varying the force applied at the calving front (downstream end) of the ice shelf. This is not an exact representation of how ice shelves generate back-pressure [Gagliardini and others, 2010], but since our primary focus is on how a release in back-pressure at the GL forces GL motion, this is sufficient for our purposes.

A recent study [Williams and others, 2012] has shown that the shallow-ice approximation, besides being invalid at short wavelength, is also invalid at sub-decadal to decadal forcing frequencies. This highlights the need to consider the nature of the mechanical model deployed in transient studies. Ice-sheet modeling has previously mainly been achievable with vertically-integrated mechanical representations of the appropriate governing Stokes equations. With recent advances, one of the models deployed solves the Stokes equations, while the others solve the vertically-integrated shallow-shelf approximation (SSA) [Morland, 1987; MacAyeal, 1992]. The four models differ thus in the mechanical model as well as in the numerical approach used. They are briefly outlined here, with more details to follow below.

The first one is the finite-element full-Stokes Elmer/Ice model, denoted **FS-AG** for Full-Stokes - Adaptive Grid, firstly presented in Durand and others [2009b] (http://elmerice.elmerfem.org). In this application, an adaptive grid refinement is used. This model is computationally two dimensional in this flowline representation. The three remaining models solve the SSA, and are therefore vertically integrated and thus computationally one-dimensional. **SSA-FG**, for SSA-Fixed Grid, and **SSA-H-FG**, for SSA-Heuristic-Fixed Grid, use a fixed grid with a resolution of 50 m and 10 km, respectively. The GL migration of **SSA-H-FG** is computed according

Table 3.1: *Summary table of model characteristics: LGGE stands for Laboratoire de Glaciologie et de Géophysique de l'Environnement, CSC - IT for Science, ULB for Université Libre de Bruxelles, and BAS for British Antarctic Survey.*

	FS-AG	SSA-H-FG	SSA-FG	SSA-PSMG
Affiliation	LGGE/CSC	ULB	ULB	BAS
	[Durand and others, 2009a]	[Docquier and others, 2011]		
Physics	Full-Stokes	SSA	SSA	SSA
Numerics	Finite Element	Finite Difference	Finite Difference	Pseudo-spectral
Vertically integrated	No	Yes	Yes	Yes
Grid	Adaptive	Fixed and Staggered	Fixed and Staggered	Moving
Resolution	GL: 50 m; divide: 10 km	10 km	50 m	3km
Time step	0.1 yr	0.1 yr	0.1 yr	1 yr
GL	Contact problem	Heuristic rule	Flotation	Margin tracking
		[Pollard and DeConto, 2009]		

to the Pollard and DeConto [2009] heuristic rule that implements the Schoof [2007a] boundary condition [Docquier and others, 2011]. The last model solves the SSA equations using pseudo-spectral method [Fornberg, 1996; Hindmarsh, 2012] on a moving grid, and will be denoted **SSA-PSMG** for SSA - Pseudo-Spectral Moving Grid. For this model, grounded ice and floating ice shelf are solved on two coupled domains, with continuity of stress and velocity across the grounding-line guaranteed. The first two models approach the problem of modeling the flow in the boundary layer by increased resolution, the third model uses a coarse resolution and a heuristic rule at the GL, and the last model addresses this issue by using high-accuracy spectral methods and explicit grounding-line motion formula [Hindmarsh and Le Meur, 2001]. All models have successfully participated in the MISMIP benchmark [Pattyn and others, 2012], exhibiting unique stable positions on downward sloping beds, unstable GL positions on retrograde slopes and related hysteresis behavior over an undulated bedrock.

Details and numerical characteristics of the four models are summarised in Tab. 3.1. In Section 3.2, specificities of the models are further described. The setup of the proposed experiments is outlined in Section 3.3 and corresponding results are discussed in Section 3.4 before we conclude in Section 3.5.

3.2 Model description

3.2.1 Governing equations

The problem consists of solving a gravity driven flow of incompressible and isothermal ice sliding over a rigid bedrock noted $b(x)$. The ice is considered as a nonlinear viscous material,

following the behavior of the Glen's flow law [Glen, 1955]:

$$\tau = 2\eta D, \tag{3.1}$$

where τ is the deviatoric stress tensor, D is the strain rate tensor defined as $D_{ij} = (\partial_j u_i + \partial_i u_j)/2$ and $u = (u, w)$ is the velocity vector. The effective viscosity η is defined as follows:

$$\eta = \frac{A^{-1/n}}{2} D_e^{(1-n)/n}, \tag{3.2}$$

where A and n are the Glen's law parameter and flow law exponent respectively, and D_e is the strain-rate invariant defined as $D_e^2 = 2D_{ij}D_{ij}$.

The ice flow is computed by solving the Stokes problem, expressed by the mass conservation equation in the case of incompressibility

$$\mathrm{tr}\,(D) = \mathrm{div}(u) = 0, \tag{3.3}$$

and the linear momentum balance equation

$$\mathrm{div}(\sigma) + \rho_i g = 0, \tag{3.4}$$

where $\sigma = \tau - pI$ is the Cauchy stress tensor with $p = -\mathrm{tr}\,\sigma/3$ the isotropic pressure, ρ_i the ice density and g the gravity vector.

Both the upper ice/atmosphere interface $z = z_s(x,t)$ and the lower ice/bedrock or ocean interface $z = z_b(x,t)$ are allowed to evolve following an advection equation:

$$\frac{\partial z_i}{\partial t} + u_i \frac{\partial z_i}{\partial x} - w_i = a_i \quad i = s, b, \tag{3.5}$$

where (u_i, w_i) is the surface velocity ($i = s$) or the basal velocity ($i = b$). For this application, the mass flux at the surface (i.e., surface mass balance) is constant and uniform ($a_s(x,t) = a_s$, see Tab. 3.2) and $a_b = 0$.

3.2.2 Boundary conditions

The geometry is restricted to a two-dimensional flowline along the x-direction and the z-axis is the vertically upward direction. The upstream boundary of the domain $x = 0$ is taken to be a symmetry axis (ice divide), where we impose the horizontal velocity $u(x = 0) = 0$. The downstream boundary, $x = x_f$ corresponds to the calving front. The position of the calving front x_f is fixed, and the GL position x_g is delimited by $0 \leq x_g \leq x_f$. In what follows, we assume a constant sea level, set to $z = 0$.

Table 3.2: *Parameters of initial steady state*

Parameter	Description	Value	Unit
b	Bed elevation	-x/1000	m
ρ_i	Ice density	900	kg m^{-3}
ρ_w	Water density	1000	kg m^{-3}
g	Gravitational acceleration	9.8	m s^{-2}
A	Glen's law coefficient	1.5×10^{-25}	Pa^{-3} s^{-1}
n	Glen's law exponent	3	
C	Basal friction parameter	10^6	Pa m$^{-1/3}$ s$^{1/3}$
m	Basal friction exponent	1/3	
a_s	Accumulation rate	0.3	m a^{-1}
C_F	Buttressing parameter	0.4	

The upper ice surface $z = z_s(x,t)$ is in contact with the atmosphere, where pressure is negligible with respect to involved stresses inside the ice body. This is a stress free surface, implying the following condition:

$$\sigma \cdot n|_{z_s} = 0, \tag{3.6}$$

where n is the outward pointing unit normal vector.

The lower surface $z = z_b(x,t)$ is either in contact with the bedrock or with the ocean, and two different boundary conditions will be applied for the Stokes problem on these two different interfaces, defined as:

$$\begin{cases} \begin{cases} z_b(x,t) > b(x) & \text{or} \\ z_b(x,t) = b(x) & \text{and} -\sigma_{nn}|_{z_b} \le p_w \end{cases} & \text{Ice/Ocean interface,} \\ z_b(x,t) = b(x) & \text{and} -\sigma_{nn}|_{z_b} > p_w & \text{Ice/Bedrock interface.} \end{cases} \tag{3.7}$$

In Eq. (3.7), the water pressure $p_w = p_w(z,t)$ is defined as:

$$p_w(z,t) = \begin{cases} -\rho_w g z & \text{if} \quad z \le 0 \\ 0 & \text{if} \quad z > 0 \end{cases} \tag{3.8}$$

where ρ_w is the water density.

Where the ice is in contact with the ocean (first condition in Eq. (3.7)), the following Neumann boundary condition applies for the Stokes equations:

$$\sigma \cdot n = -p_w n. \tag{3.9}$$

Where the ice is in contact with the bedrock (second condition in Eq. (3.7)), a no-penetration

condition is imposed as well as a friction law, such as

$$u \cdot n = 0, \tag{3.10}$$

$$\tau_b = t \cdot (\sigma \cdot n)|_b = C u_b^m,$$

where τ_b is the tangential component of the traction, t is the tangent vector to the bedrock, u_b is the sliding velocity, C is the friction parameter and m is the friction law exponent (see Tab. 3.2 for the adopted values).

3.2.3 Shallow-shelf/shelfy stream approximation (SSA)

As mentioned previously, three of the four models use the Shallow-Shelf Approximation (SSA) which is a vertically integrated approximation of the Stokes Eqs. (3.3) and (3.4). The horizontal velocity $u(x)$ is obtained by solving the following equations [Morland, 1987; MacAyeal, 1992]:

$$\begin{cases} 2\dfrac{\partial (h\tau_{xx})}{\partial x} - C u^m = \rho_i g h \dfrac{\partial z_s}{\partial x} & 0 \leq x \leq x_g, \text{ for the grounded part,} \\[2ex] 2\dfrac{\partial (h\tau_{xx})}{\partial x} = \gamma h \dfrac{\partial h}{\partial x} & x_g < x \leq x_f, \text{ for the floating part.} \end{cases} \tag{3.11}$$

where $h = h(x)$ is the ice thickness, $\tau_{xx} = 2\eta \partial_x u$ is the longitudinal deviatoric stress and u is the horizontal velocity in the flow direction. The effective viscosity, η, is computed as in (3.2), where $D_e \approx \partial_x u$. The parameter γ is defined as:

$$\gamma = \rho_i g \left(1 - \frac{\rho_i}{\rho_w} \right). \tag{3.12}$$

According to the SSA approximation, ice deformation is dominated by membrane stresses and vertical shear within the ice is neglected. For the SSA model, the only boundary condition is $u(x = 0) = 0$ at the ice divide, whereas the boundary condition at the lower surface is already implicitly included in the set of equations (3.11) and the boundary condition at the calving front is defined in section 3.2.5.

The lower surface z_b is determined from the no-penetration condition and the floating condition:

$$\begin{cases} z_b(x,t) = b(x) & \text{for } x \leq x_g, \\ z_b(x,t) = -h\rho_i/\rho_w > b(x) & \text{for } x > x_g. \end{cases} \tag{3.13}$$

The upper surface $z_s = z_b + h$ is deduced from the vertically-integrated mass conservation equation giving h as

$$\frac{\partial h}{\partial t} + \frac{\partial (hu)}{\partial x} = a_s. \tag{3.14}$$

3.2.4   Grounding-line treatment

The implementation of GL treatment differs from one model to the other. In this section we define for each model the specificities regarding the treatment of the GL.

The **FS-AG** model solves the contact problem between the ice and the bedrock. During a time step, the contact condition (3.7) is tested at each node of the mesh and the bottom boundary conditions (3.9) or (3.10) are imposed accordingly. More details about this method and its implementation can be found in Durand and others [2009a]. The consistency of this GL implementation strongly depends on the grid resolution, and a grid size lower than 100 m is needed to obtain reliable results [Durand and others, 2009b]. In order to reach this resolution while considering a reasonable number of mesh nodes, an adaptive mesh refinement around the GL is applied: the horizontal distribution of nodes is updated at every time step, such that finer elements are concentrated around the GL.

For the **SSA-FG** model the grid points are kept fixed in time and the last grounded grid point is determined through the flotation criterion, *i.e.* by solving the following equation:

$$F = h_g + b(x_g) \frac{\rho_w}{\rho_i} = 0. \tag{3.15}$$

The GL position x_g is given with sub-grid precision between the last grounded grid point and the first floating point following the method proposed by Pattyn and others [2006].

The GL position is also determined with sub-grid precision following Pattyn and others [2006] for the **SSA-H-FG**, but while **SSA-FG** uses the flotation criterion as a boundary condition at the GL, the **SSA-H-FG** model makes use of an additional boundary condition based on the semi-analytical solution of Schoof [2007a]. The ice flux at the GL q_g is calculated as a function of ice thickness at the GL h_g:

$$q_g = \left(\frac{A\rho_i g \gamma^n}{4^n C} \right)^{\frac{1}{m+1}} \theta^{\frac{n}{m+1}} h_g^{\frac{m+n+3}{m+1}}, \tag{3.16}$$

and is used in a heuristic rule to enable GL migration [Pollard and DeConto, 2009]. This parameterization allows relatively coarse resolutions to be used (10 km in this study) and gives steady-state results of GL position that are independent of the chosen resolution and agree well with the semi-analytical solution given by Schoof [2007a] [Docquier and others, 2011]. In Eq. (3.16), the coefficient θ accounts for buttressing and is defined as

$$\theta = \frac{4\tau_{xx}|_{x_g}}{\gamma h_g}. \tag{3.17}$$

The numerical approach used by the pseudo-spectral **SSA-PSMG** model consists in explicitly

calculating the rate of GL migration, $\dot{x}_g$, according to the following explicit formula [Hindmarsh and Le Meur, 2001]

$$\dot{x}_g = -\frac{\partial_t F}{\partial_x F}, \tag{3.18}$$

where F is given by Eq. (3.15). At each time step, a new position is computed and the grid moves accordingly, so that the GL coincides exactly with a grid point [Hindmarsh, 1993]. Moving grids have the ability to ensure that a grid-point always coincides with the GL, allowing easy representation of gradients at this location, but are not always convenient to implement.

3.2.5 Calving front boundary condition and the specification of buttressing

The experiments we propose are driven by changes in the buttressing force. One approach could have consisted of applying lateral friction on the ice shelf following the method of Gagliardini and others [2010], but the total buttressing force would then have been function of the ice-shelf area and ice-shelf velocities, and therefore different for all models. In order to ensure the same buttressing force for all models, we follow the method proposed by Price and others [2011], in which the inward force at the calving front is modified by a factor, noted C_F in our study.

For vertically integrated models, the horizontal force acting on the calving front is entirely due to the hydrostatic water pressure and the longitudinal deviatoric stress at the front is given by MacAyeal and others [1996]:

$$\tau_{xx}|_{x_f} = \frac{\gamma}{4} h_f, \tag{3.19}$$

where h_f is the ice thickness at the calving front. In the case of the vertically integrated models **SSA-FG**, **SSA-H-FG** and **SSA-PSMG**, a factor C_F is then used to modify longitudinal deviatoric stress (3.19), which becomes:

$$\tau_{xx}|_{x_f} = C_F \frac{\gamma}{4} h_f. \tag{3.20}$$

A value of $C_F = 1$ means that the longitudinal deviatoric stress at the calving front is opposed solely by water pressure, corresponding to no buttressing. Values less than one induce a lower extensional longitudinal deviatoric stress at the front, simulating the effect of buttressing. Note that this procedure implies an additional *force* applied at the calving front; this results in a varying contribution of the butressing to the *stress* as the ice thickens upstream.

Moreover, for **SSA-H-FG**, the buttressing parameter C_F is by construction incorporated in the boundary condition at the GL. This boundary condition relates the ice flux q_g to the ice

thickness h_g at the GL and includes the buttressing factor θ as defined by Eq. (3.17). From the SSA equations in the ice shelf, we derive (see Appendix A) the relation that links θ and C_F through both the ice thickness at the GL h_g and the ice thickness at the calving front h_f:

$$\theta = 1 - (1 - C_F)\left(\frac{h_f}{h_g}\right)^2.$$ (3.21)

The other two SSA models solve for the longitudinal variation of τ_{xx} in the ice shelf to compute the value at the GL.

For the **FS-AG** model, the hydrostatic pressure $p_w(z)$ is imposed along the ice column in contact with the sea, so that the longitudinal Cauchy stress is not uniform on this boundary. This non-uniform stress induces a bending of the ice shelf near the front. To avoid an increase of this bending when adding the buttressing, the stress condition at the front is modified by adding a uniform buttressing stress p_b, such that

$$\sigma_{xx}|_{x_f}(z,t) = p_w(z) + p_b(t).$$ (3.22)

Using Eqs. (3.22) and (3.20), and assuming the equality of the mean longitudinal Cauchy stress for both parameterisations, the buttressing stress to be applied at the front of the full-Stokes model is obtained as a function of C_F (see Appendix B), such as

$$p_b = \frac{\rho_w g z_b^2}{2\rho_i h_f}(\rho_w - \rho_i)(C_F - 1).$$ (3.23)

Note that p_b has to be computed at each time step since it depends on the ice thickness at the front, which is not constant.

3.3 Experimental setup

We consider an ice sheet resting on a downward sloping bedrock, with the calving front fixed at 1000 km, as shown in Fig. 3.1. The GL never advances as far as this in the experiments. The flow parameters summarised in Tab. 3.2 are used by each model in order to calculate a steady-state geometry. The steady state is obtained with a buttressed ice shelf ($C_F = 0.4$).

Computed steady surfaces are in good agreement between models, exhibiting only a slight difference in GL position of less than 20 km (see Fig. 3.1).

We chose the simpler, stable case of a forward slope for the simple reason that computing comparable initial starting conditions on the unstable reverse slope is a practical impossibility. GL retreat rates are governed by the water depth and the buttressing, and we chose values that were physically acceptable and also produced physically reasonable retreat rates.
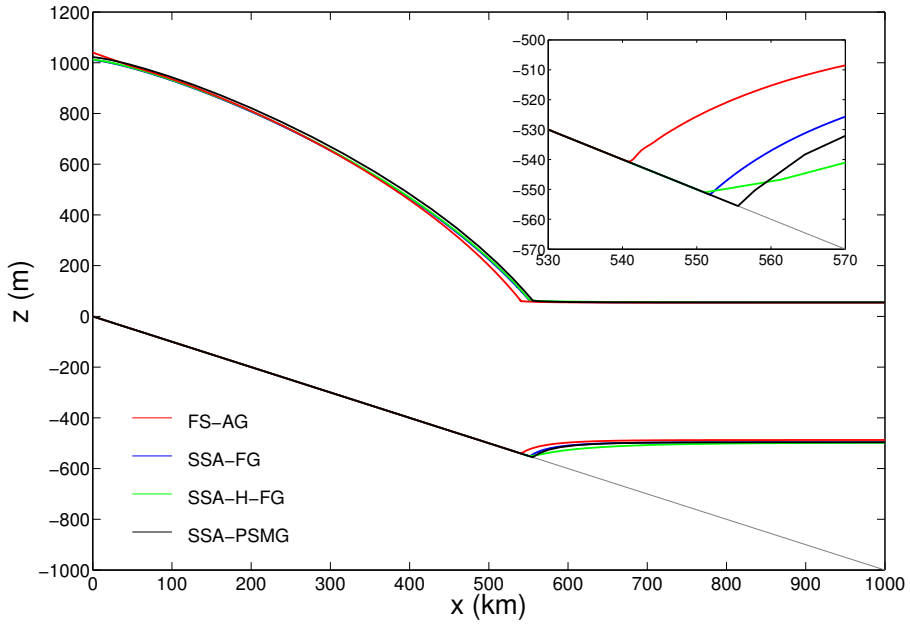
Figure 3.1: *Initial steady-state geometry ($C_F = 0.4$) for all models. The inset emphasizes the differences in GL position.* **SSA-H-FG** *lower surface has a quite different shape with respect to the three other models due to its coarser resolution (10 km).*

Table 3.3: *GL position for the intial steady state ($C_F = 0.4$) and for the different perturbations for each model after 200 years. The difference between the initial steady state and the perturbed state is given in brackets. All values are in km.*

	FS-AG	SSA-FG	SSA-H-FG	SSA-PSMG
C_F=0.4	540.5	551.8	554.1	556.1
C_F=0.5	523.8 (16.7)	534.7 (17.1)	530.4 (23.8)	539.2 (16.9)
C_F=0.8	482.0 (58.5)	488.5 (63.3)	474.8 (79.3)	495.2 (60.9)
C_F=1	463.7 (76.8)	468.9 (82.9)	454.3 (99.8)	476.8 (79.3)

Ice-sheet geometry is subsequently perturbed by a release of the initial buttressing force. This process, arising from increased melt of the ice shelf, appears to be responsible for the observed acceleration of Antarctic outlet glacier [Wingham and others, 2006; Rignot and others, 2008; Pritchard and others, 2012]. Starting from the steady geometries obtained with initial factor $C_F = 0.4$, the buttressing force is decreased at $t = 0$ (i.e. C_F increases) and kept constant during the simulation. Since we focus on the transient behavior, simulations are run during 200 years. Three different amplitudes of the perturbation are investigated with corresponding modified values of $C_F = 0.5, 0.8$ and 1.

3.4   Results and discussion

3.4.1   Transient behavior of direct observable variables on actual ice sheets

We first evaluate the response of the various models regarding the variables that are currently observed over actual ice sheets, namely GL position (Fig. 3.2), surface elevation change (Fig. 3.3) and surface velocity (Fig. 3.4).

As expected, release of buttressing induces a GL retreat, and the greater the release, the larger the amount and rate of retreat [Gagliardini and others, 2010]. Retreat can reach up to almost 100 km in 200 years following a complete loss of buttressing restraint ($C_F = 1$, see Fig. 3.2 and Tab. 3.3). The different models show a similar trend regarding the temporal evolution of GL position (left panels in Fig. 3.2). However, owing to the various initial steady-state profiles, the GL position differs between models. For the three perturbations, **SSA-H-FG** shows the highest GL retreat compared to the initial position, followed by **SSA-FG**, then **SSA-PSMG**, and finally **FS-AG** (Tab. 3.3).

The evolution of the GL position of **SSA-H-FG** has a step-like behavior due to the model grid size (10 km).

Rates of GL migration (right panels in Fig. 3.2) for **SSA-PSMG** and **SSA-FG** exhibit a very
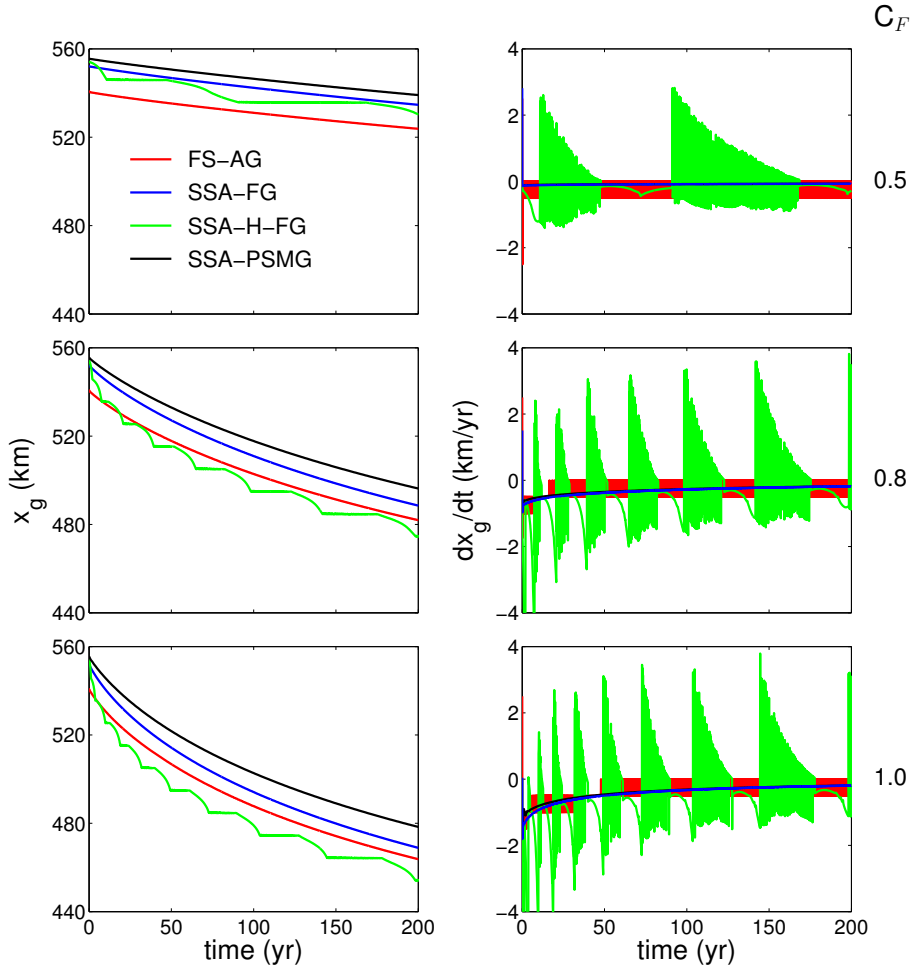
Figure 3.2: *Grounding-line position x_g (left) and migration rate dx_g/dt (right) as a function of time for the four models and for the three buttressing values ($C_F = 0.5$ on the first line, $C_F = 0.8$ on the second line and $C_F = 1$ on the third line).*
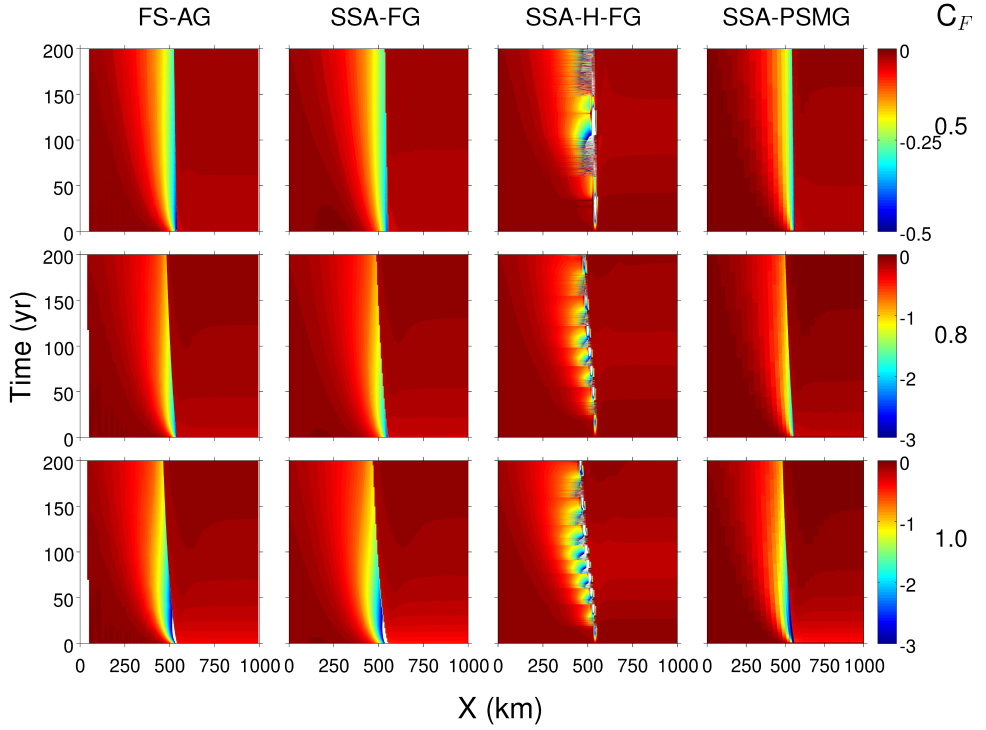
Figure 3.3: *Rate of surface elevation change (m yr^{-1}) as a function of time and horizontal distance (x = 0 corresponds to the ice divide and $x_f = 1000$ km is the calving front) for the three buttressing values (lines) and for the four models (columns).*

Figure 3.4: *Surface horizontal velocity (km yr^{-1}) as a function of time and horizontal distance (x = 0 corresponds to the ice divide and $x_f = 1000$ km is the calving front) for the three buttressing values (lines) and for the four models (columns).*
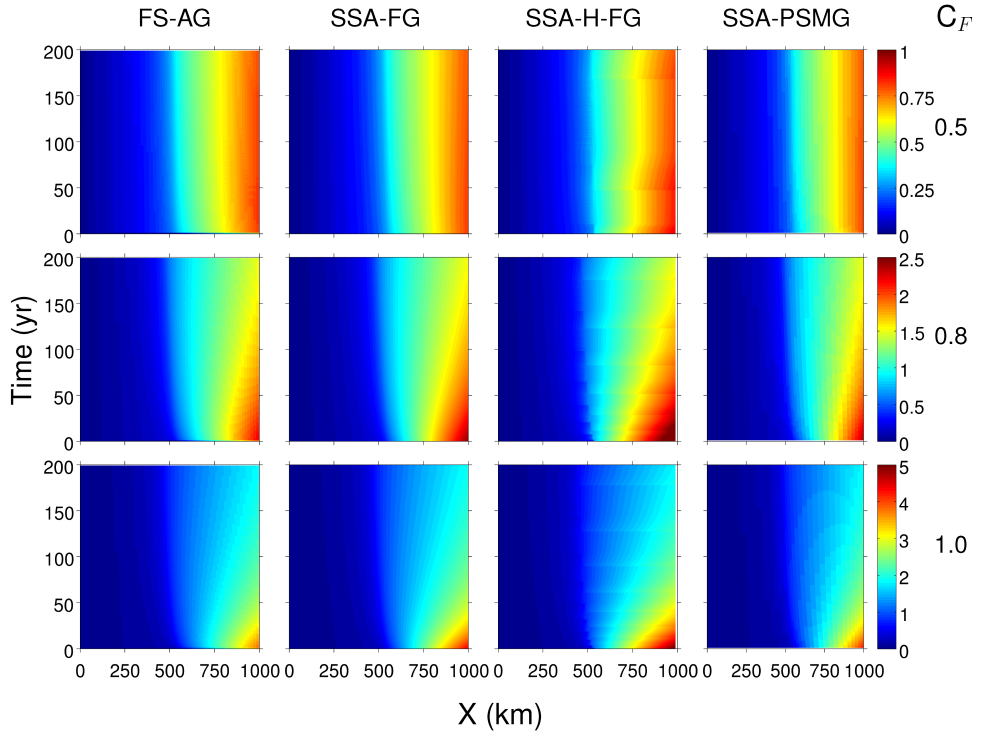
similar pattern, *i.e.* a high retreat rate value in the beginning of the perturbation and then a convergence towards a zero-value. Moreover, the greater the perturbation (higher value of C_F), the larger the retreat rates in the beginning of the perturbation. The smooth decrease of the migration rate computed by **SSA-PSMG** is due to the explicit way the GL migration is computed (see model description above). Because the **SSA-FG** interpolates the GL position between the last grounded point and the first floating point [Pattyn and others, 2006], it also ensures a smooth description of GL migration rate. However, **FS-AG** and **SSA-H-FG** show discontinuous GL migration rate induced by numerical artefacts: both models give results that are affected by their grid size. The stepped patterns obtained with **FS-AG** are due to high frequency oscillation between two successive nodes during GL migration: the GL retreats, then stays at the same position during one time step, then retreats, etc. so that the GL migration rate oscillates with an amplitude of 500 m a^{-1} (i.e. grid size divided by time step). The numerical noise found in **SSA-H-FG** is due to a combination of both the grid size effect and *single-cell dithering*, i.e., flipping back and forth between upstream and downstream grid points [Pollard and DeConto, 2012]. As a general trend, the GL retreats by 10 km steps as a consequence of the model resolution (grid size effect). At some discrete GL positions (every 10 km), the rate of GL migration varies significantly due to the heuristic rule used in the model (flux imposed either upstream or downstream the GL), so that the GL slightly advances and retreats within the same grid cell (single-cell dithering). In summary, the GL retreats by 10 km (corresponding to the model resolution) and reaches a discrete position where it oscillates within the same grid cell, and then retreats before reaching another discrete position again, etc...

Rates of surface elevation change through time and distance from the ice divide are presented in Fig. 3.3 for the various models and perturbations. The horizontal surface velocity is similarly plotted (see Fig. 3.4). The largest perturbation ($C_F = 1$) exhibits rates of surface elevation change of a few meters per year in the beginning, with horizontal velocities above one kilometer per year. Together with GL migration rates of the order of a kilometer per year (Fig. 3.2), those are in general agreement with the obervation for currently recessing glaciers of West Antarctica, and Pine Island Glacier in particular [Rignot, 1998; Rignot and others, 2011]. That confirms the relevance of the amplitude of the perturbations applied. Rates of surface elevation change are quite similar between the four models (Fig. 3.3). The highest thinning rates appear in the vicinity of the GL at the beginning of the perturbation. Similarly, the surface velocities steadily decrease during the simulation (Fig. 3.4). High frequency and small amplitude numerical noise in **FS-AG** appear not to significantly affect the surface response. However, with **SSA-H-FG** the high frequency and amplitude variabilities drastically affect the surface thinning rate and velocities over short time scales (*i.e.* about a decade).

We deliberately chose a low spatial resolution (uniform 10 km along the flowline) for the **SSA-H-FG** model compared with other models. Indeed, in contrast to other approaches, such type of models produces consistent steady geometries at low spatial resolution [Docquier and others, 2011], which is the main motivation for applying such parameterizations in large-scale

ice-sheet models. One can also note that ice-sheet models using a flux boundary condition at the grounding line with a similar resolution are currently used on centennial time scale to estimate Antarctic evolution [Bindschadler and others, 2013]. For the numerical approaches of **SSA-FG** and **FS-AG**, they are known to fail to compute consistent steady geometries whether a too large resolution is used (Durand et al, 2009). This would therefore have no sense to investigate their transient behaviors with too coarse a mesh. To our opinion, this justifies our choice of different mesh sizes from one model to the other according to the (i) capacity of each model to correctly compute steady states at a given resolution, (ii) the mesh size currently used to predict ice-sheet short-term response. However, evaluating their performance with similar numerics on controlled experiments remains to be done. Increasing the resolution (down to 500 m) for the **SSA-H-FG** model allows removal of high frequency numerical artefacts, but the general trend of variables such as GL migration rate and surface elevation changes over 200 years does not depend on resolution (data not shown). Moreover, refining the grid size significantly increases its numerical cost, so that the major advantage of this model is lost, as well as its applicability to large-scale ice-sheet models.

3.4.2 Divergence from the boundary-layer solution

Despite the numerical noise exhibited by **SSA-H-FG** and **FS-AG** models, the evolution of the geometry during the simulations appears very similar for all four models. However, the boundary layer theory implemented in the **SSA-H-FG** model hypothesizes near-steady conditions and its ability to represent transients requires evaluation. In Fig. 3.5, the flux at the GL is plotted as a function of the instantaneous ice thickness at the GL for all models and simulations. By construction, **SSA-H-FG** essentially follows the boundary layer prescription. This can most clearly be seen for the case $C_F = 1$ (see the bottom of Fig. 3.5) where the close correspondence of the curves of Schoof [2007a] and **SSA-H-FG** is evident. This correspondence is not as clear for the other perturbations, since the **SSA-H-FG** boundary condition for the flux now relies on a parameterization of θ, which in turn depends on the quantity h_f/h_g (see Eq. 3.21). Since this ratio varies in time, the steady-state condition of the Schoof condition is not fulfilled.

Interestingly, and despite their very different physical and numerical approaches, all the other models show very similar behavior, with the boundary layer theory result attained after some time. This is most obvious for the largest perturbation ($C_F = 1$) but also clearly visible for the weaker perturbations ($C_F = 0.8$ and 0.5). However, during the highly transient phase, for a given ice thickness at the GL, the ice flux is substantially overestimated by the boundary layer theory, consequently overestimating the outflow during the whole period of 200 years.
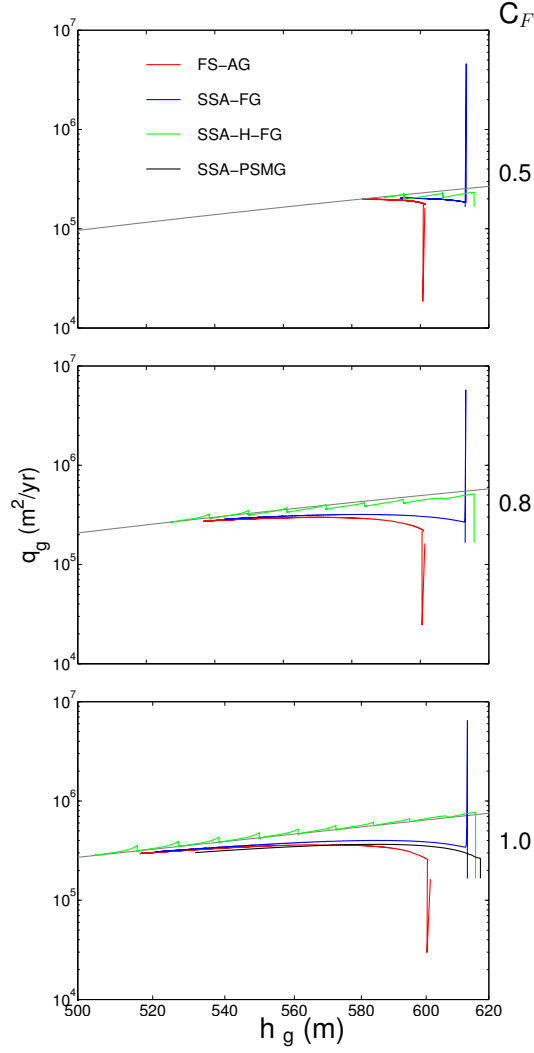
Figure 3.5: *GL ice flux q_g as a function of GL ice thickness h_g for the four models and for the three different buttressing values, compared with the Schoof [2007a] solution (in grey).*

3.4.3   Changes in Volume Above Flotation (ΔVAF)

From the perspective of projecting the future contribution of Antarctica to sea-level rise (SLR), the change in Volume Above Flotation (ΔVAF = VAF(t) - VAF($t = 0$)) is certainly a pertinent variable to investigate. Indeed, plotting ΔVAF (Fig.3.6) has the advantage of integrating through time both the contribution coming from outflow at the GL and the consequence of grounding-line retreat in terms of ice release. In our case, this also allows the investigation of the spread in the transient behavior of the various models in response to similar perturbations. We also plotted the evolution of ΔVAF for each model relative to ΔVAF computed by **FS-AG** as it directly emphasizes the difference between models (Fig.3.6). Choice of FS-AG model as a reference was arbitrary.

As anticipated, **SSA-H-FG** shows the greatest change in VAF compared with other models. Relative to **FS-AG**, **SSA-H-FG** overestimates the contribution to SLR by more than 100 % during the first 50 years of the simulation, which decreases to a 40 % overestimation after 200 years. **SSA-FG** shows a similar pattern with a smaller overestimation (about 15 % after 200 years). On the other hand, **SSA-PSMG** briefly underestimates the change in VAF relative to **FS-AG** at the beginning of the perturbation, but after 20 years the contribution of the models to SLR is remarkably similar to the one computed by **FS-AG**, with relative difference below 5 %. It seems striking that response in terms of relative ΔVAF is extremely similar from one perturbation to the other, while the response of the models is highly modulated by the amplitude of the perturbation. This particularity may allow in the future to weight the response of a model according to the physics implemented in.

This intercomparison strongly suggests that models prescribing flux at the GL according to the boundary layer theory most probably overestimate ice discharge, with significant difference at the very beginning of the transient simulation. It also clearly shows that the rate of contribution to SLR significantly differs from one model to the other, even for a relatively simple and constrained experiment. When extrapolated to the current imbalance of the Antarctic ice sheet, this would have important consequences. According to Rignot and others [2011], the Antarctic ice sheet drained about 100 Gt/yr in 2000 with an increasing acceleration trend in mass loss of 14.5 Gt/yr^2. Following that trend, the Antarctic ice sheet have contributed by 4.6 mm of SLR between 2000 and 2010. Assuming ice-sheet models were capable of describing exactly the ice dynamical conditions in 2000, and also assuming the parameters forcing enhanced ice discharge to be properly known, we can compute a broad scale of uncertainties on predicted SLR arising from the use of the four different models. If we arbitrarily consider the **FS-AG model** as the one that would give the SLR prediction of 4.6 mm in 2010 after a given perturbation, the use of the other models would lead to an erroneous contribution to SLR between 3 mm (under estimation of 30 % by **SSA-PSMG**) and 18 mm (over estimation of 300 % by **SSA-H-FG**). Furthermore, as ice sheets are still in a transient phase (*i.e.*, perturbations are sustained through time) the discrepancy of the models would eventually increase with time integration. Of course, these assertions have to be moderated by the fact that the complexity
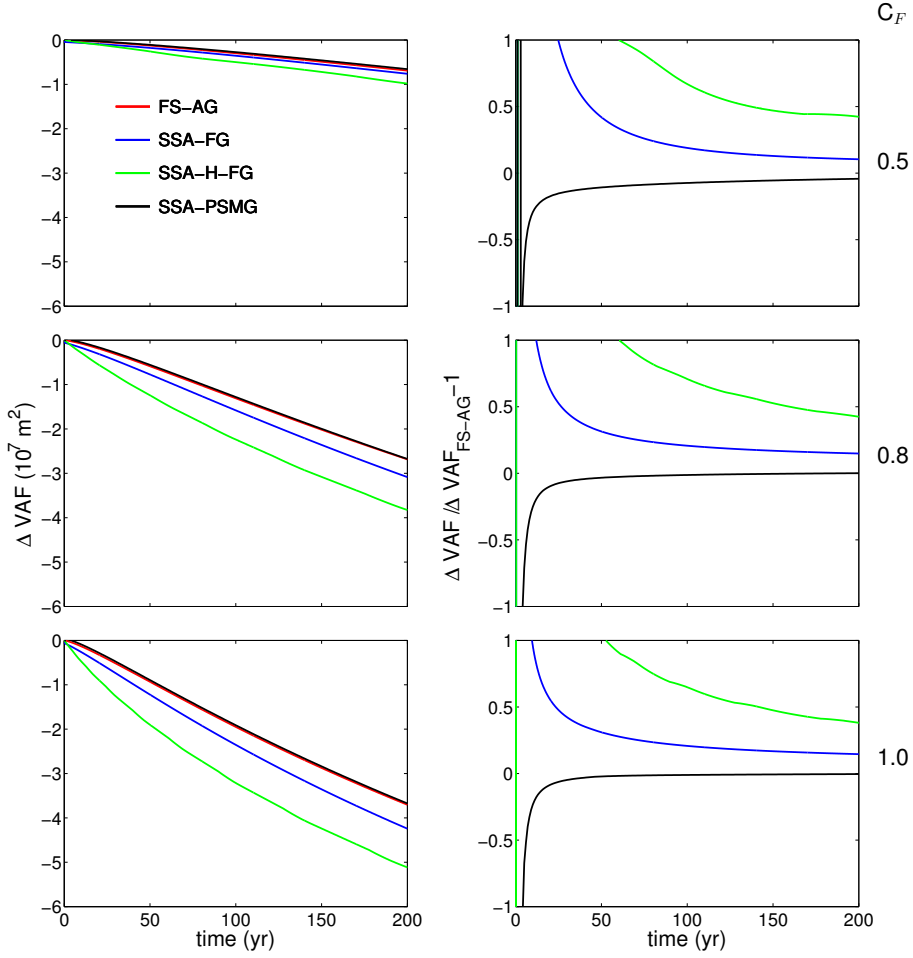
Figure 3.6: *Temporal evolution of the variation of Volume above Flotation (ΔVAF) for each model (left) and, expressed relative to **FS-AG** (Δ VAF$_{FS-AG}$) for the three remaining models (right), for the three butressing values (lines).*

of actual 3D geometries could mitigate the discrepancy between model results, which is the focus of future research.

3.5 Conclusions

We have computed the transient response of four flowline ice-sheet models to a reduction in the buttressing force exerted by an ice shelf onto the upstream grounded ice sheet. The intensity of buttressing perturbations was chosen in order to reproduce changes in geometry that are comparable to those observed on current ice sheets. Compared with MISMIP, we investigated the transient response in more detail and applied a perturbation that reflects direct mechanical forcing.

The dynamics (or momentum balance) are implemented in a different way in the different models (from SSA to the solution of the full-Stokes equations), while the models differ in their numerical treatment as well (finite difference and finite element). One of the models includes the heuristic rule of Pollard and DeConto [2009], *i.e.* the flux-thickness relation proposed by Schoof [2007a] is imposed at the GL. All models have successfully participated in the MISMIP benchmark [Pattyn and others, 2012], exhibiting unique stable positions on downward sloping beds, unstable GL positions on retrograde slopes and related hysteresis behavior over an undulated bedrock.

Surprisingly, and despite the different physics and numerics implemented, all models broadly give similar results in terms of changes in surface geometry and migration of the GL. However, discrepancies remain in between models. Particularly, the **SSA-H-FG** model which directly implements the boundary layer theory exhibits faster grounding-line retreat and larger surface thinning (Fig.3.2 and Fig.3.3). Once cumulated over years, this leads to significant differences in predicted discharge. Moreover, the prescription of flux at the GL introduces high frequency, large amplitude numerical noise deteriorating the surface change signal over decadal time scales. Finally, it seems that, at least in these experiments, the boundary layer theory overestimates the discharge during the transient evolution. As a consequence, models that prescribe the flux at the GL should be used with particular caution when dealing with small spatial and temporal scales.

Estimation of the contribution to SLR through numerical modeling still exhibits large uncertainties, with results from different models showing > 100 % spread on a decadal time-scale and still around 40 % two hundred years after the initial change in buttressing. There may be a large uncertainty in models that are seeking to establish reliable projection of coming contribution of Antarctic ice sheet to SLR. Further model intercomparison must be pursued to better constrain the rate of discharge, and intercomparisons on specific Antarctic outlet glaciers should be encouraged in the near future.

3.6   Appendix A

In this Appendix the relation between the buttressing factors θ in Eq. (3.17) and C_F in Eq. (3.20) is derived. The ice-shelf equation is

$$2\frac{\partial\left(h\tau_{xx}\right)}{\partial x} = \frac{\gamma}{2}\frac{\partial\left(h^2\right)}{\partial x}, \tag{3.24}$$

where h is the ice thickness along the ice shelf. The longitudinal deviatoric stress within the ice shelf is then obtained as

$$\tau_{xx} = \frac{\gamma}{4}h - \frac{B}{h}, \tag{3.25}$$

where B is the back-force at the calving front. Evaluatting this at $x = x_f$ and using (3.20), we obtain

$$\tau_{xx}|_{x_f} = C_F\frac{\gamma}{4}h_f = \frac{\gamma}{4}h_f - \frac{B}{h_f}, \tag{3.26}$$

yielding

$$B = (1 - C_F)\frac{\gamma}{4}h_f^2, \tag{3.27}$$

and

$$\tau_{xx} = \frac{\gamma}{4}\left(h - (1 - C_F)\frac{h_f^2}{h}\right). \tag{3.28}$$

Now, at the GL $x = x_g$, by definition of θ (3.17):

$$\tau_{xx}|_{x_g} = \theta\frac{\gamma}{4}h_g, \tag{3.29}$$

so that

$$\theta = 1 - (1 - C_F)\left(\frac{h_f}{h_g}\right)^2. \tag{3.30}$$

3.7   Appendix B

In this appendix, we demonstrate how is obtained the buttressing pressure $p_b(t)$ in Eq.(3.22) giving the front-stress for the **FS-AG** model. We need to find $p_b(t)$ such that the mean longitudinal Cauchy stress be the same for all models. This equality is expressed as follows:

$$\bar{\sigma}_{xx}^{SSA} = \bar{\sigma}_{xx}^{FS} \tag{3.31}$$

where $\bar{\sigma}_{xx}^{SSA}$ and $\bar{\sigma}_{xx}^{FS}$ are the longitudinal Cauchy stress of SSA models and **FS-AG** model, respectively.

The mean longitudinal Cauchy stress for SSA models reads:

$$\bar{\sigma}_{xx}^{SSA} = 2\bar{\tau}_{xx} + \bar{\sigma}_{zz} \tag{3.32}$$

where $\bar{\sigma}_{zz} = -\dfrac{\rho_i g h_f}{2}$ and $\bar{\tau}_{xx}$ is given by Eq. (3.20).

The longitudinal Cauchy stress for **FS-AG** model, given by Eq.(3.22), and once integrated over the ice column gives:

$$\bar{\sigma}_{xx}^{FS} = -\frac{\rho_w g z_b^2}{2h_f} + p_b \tag{3.33}$$

Using Eq. (3.32) for SSA models and Eq. (3.33) for **FS-AG**, Eq. (3.31) leads to

$$2C_F \frac{\gamma}{4} h_f - \frac{\rho_i g h_f}{2} = -\frac{\rho_w g z_b^2}{2h_f} + p_b \tag{3.34}$$

Using the flotation condition $\rho_i h_f = \rho_w z_b$, and after simplifications, p_b can be isolated and deduced as

$$p_b = \frac{\rho_w g z_b^2}{2\rho_i h_f} (\rho_w - \rho_i)(C_F - 1). \tag{3.35}$$

3.8   Supplementary results

Some additional results that were not published in the article above are presented below.

3.8.1   Reversibility test with SSA-FG

Steady-state GL positions are unique on a downward-sloping bedrock in the absence of ice-shelf buttressing [Schoof, 2007a]. Hence, perturbing the ice sheet-ice shelf system and subsequently resetting the parameters to their initial values should give a final steady GL position identical to the initial position. Any difference may therefore be a numerical artifact, most likely due to under-resolution [Pattyn and others, 2012, 2013]. It is a necessary condition for an ice-sheet model to be able of reproducing such a reversibility within a certain error range in order to show a realistic transient behavior.

The reversibility of the GL simulated by SSA-H-FG has already been shown in Docquier and others [2011]. To test the reversibility of SSA-FG, the third experiment of Docquier and others [2011] is performed, where a linearly downward-sloping bed (2.27) is used as well as the constants of Table 2.1. We start from an initial steady-state ice sheet with $A = 10^{-25}$ Pa^{-3} s^{-1} (x_{g1} is the initial steady-state GL position). The bulk viscosity of the ice sheet is increased by setting $A = 4 \times 10^{-26}$ Pa^{-3} s^{-1}, leading to a GL advance, until a new steady state is reached
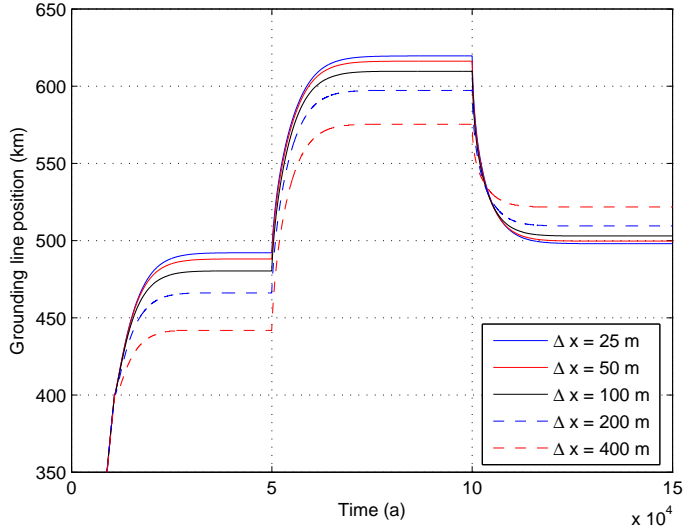
Figure 3.7: *GL position as a function of time for SSA-FG with different grid sizes corresponding to the third experiment of Docquier and others [2011].*

(x_{g2}). Subsequently, the viscosity is decreased by resetting $A = 10^{-25}$ Pa^{-3} s^{-1}, invoking a GL retreat to the initial state (x_{g3}). To ensure steady state, we run the model 50 ka for each A value, so that the model is run 150 ka in total.

Results of this test show that the smaller the grid size the better the GL reversibility (smaller difference between x_{g3} and x_{g1}) (Figs. 3.7 and 3.8, and Tab. 3.4). Figure 3.8 clearly shows the convergence of the GL reversibility with smaller grid sizes. Since the GL advances by about 130 km when the viscosity increases ($x_{g2} - x_{g1}$), a reversibility of 11.5 km obtained with a grid size Δx = 50 m is considered sufficient for transient modeling studies. Table 3.4 shows that the results differ in a very minor way when using a model time step of 5 years instead of 1 year.

3.8.2 GL migration rate with SSA-H-FG

In order to better understand the behavior of the GL with SSA-H-FG for the buttressing experiments described in the paper above, it is worth realizing a diagram relating GL migration rate to GL position (Fig. 3.9). The beginning (end) of the perturbations corresponds to the right (left respectively) part of this diagram. Whatever the perturbation in C_F, there are two main effects provoking the numerical noise associated with this model:

1. **Grid size effect**: the GL retreats by 10 km steps (which corresponds to the model resolution).
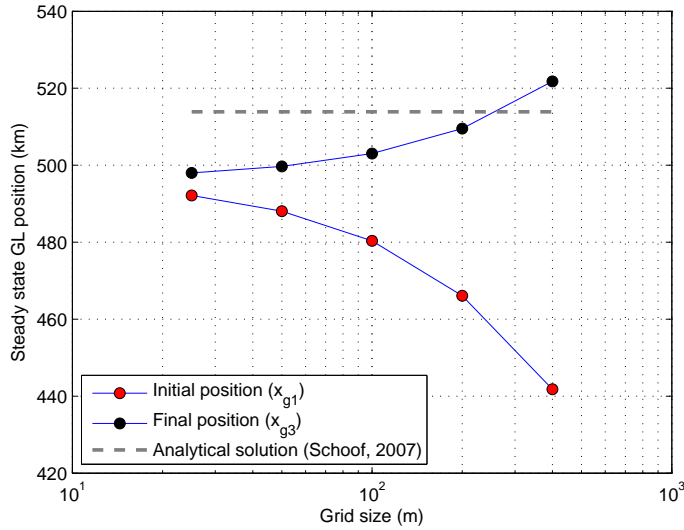
Figure 3.8: *Initial (x_{g1}) and final (x_{g3}) steady-state GL positions as a function of grid size for SSA-FG corresponding to the third experiment of Docquier and others [2011].*

Table 3.4: *GL positions corresponding to initial steady state (x_{g1}), steady state after viscosity perturbation (x_{g2}), and final steady state by resetting the viscosity to its initial value (x_{g3}). Also shown are differences between final and initial steady-state GL positions ($\Delta FI = |x_{g3} - x_{g1}|$). These are the results obtained with the semi-analytical solution [Schoof, 2007a], the SSA-H-FG model (mean of different resolutions), and the SSA-FG model with different grid sizes. They correspond to the third experiment of Docquier and others [2011].*

| Model	Grid size (m)	Time step (a)	x_{g1} (m)	x_{g2} (m)	x_{g3} (m)	ΔFI (m)
Analytical solution			513 868	644 001	513 868	0
SSA-H-FG	mean	1	509 167	638 364	509 188	21
SSA-FG	25	1	492 162	619 638	498 013	5 851
SSA-FG	25	5	492 212	619 638	497 963	5 751
SSA-FG	50	1	488 075	616 275	499 675	11 600
SSA-FG	50	5	488 175	616 325	499 675	11 500
SSA-FG	100	1	480 350	609 650	503 050	22 700
SSA-FG	100	5	480 350	609 650	502 852	22 502
SSA-FG	200	1	466 100	597 300	509 501	43 401
SSA-FG	200	5	466 100	597 499	508 905	42 805
SSA-FG	400	1	441 800	575 399	521 801	80 001
SSA-FG	400	5	441 800	575 399	518 624	76 824
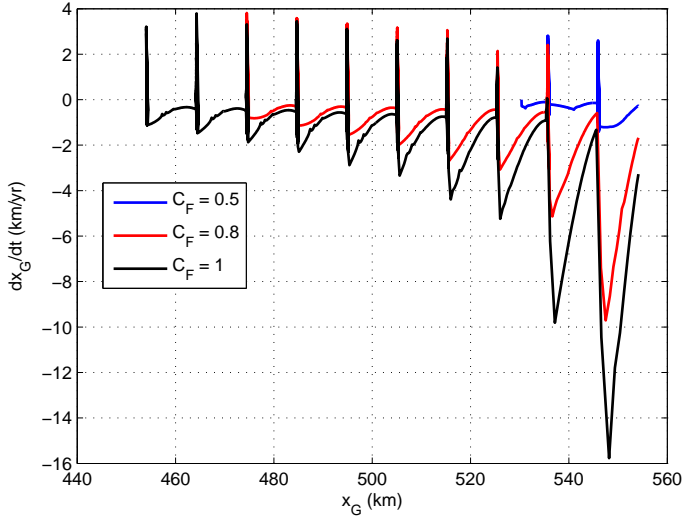
Figure 3.9: *GL migration rate dx_g/dt as a function of GL position x_g for SSA-H-FG and the three buttressing values (C_F=0.5, C_F=0.8 and C_F=1).*

2. '**Single-cell dithering**' (mentioned by Pollard and DeConto [2012]): every 10 km, the GL flips back and forth within the same grid cell due to the heuristic rule used in the model (flux imposed either upstream or downstream the GL), explaining the advance rates.

The general behavior of the GL with this model is summarized as follows: the GL retreats by a distance corresponding to the grid size and reaches a discrete position where it flips back and forth within the same grid cell, and then retreats before reaching another discrete position again, etc. Figure 3.9 also shows that the higher the buttressing loss ($C_F = 1$) the higher the GL retreat rates.

3.8.3   Volume above flotation with SSA-H-FG

One of the reviewers of this paper made the following comment: 'In any case, 10-km resolution only leaves a few grid points to resolve the relatively small length scales here, as apparent in the slope of basal ice within approx. 20 km of the GL (inset, Figure 3.1). Maybe the SSA-H-FG model discrepancies are due mainly to this coarseness, and not to intrinsic physics and parameterizations.'

We answered the comment this way: 'Simulations with much finer resolutions (1.25, 2.5 and 5 km) have been done using the SSA-H-FG model to check whether the resolution or the physics implemented is responsible of the disagreement with other models. As can be seen in Figure

3.10, despite a fine resolution the transient response in terms of ice discharge is extremely similar for coarse (10 km) and fine (1.25 km) meshes. So, this is the implementation of the boundary layer theory that is responsible of the too fast response. This is now discussed in the paper (p.11).'
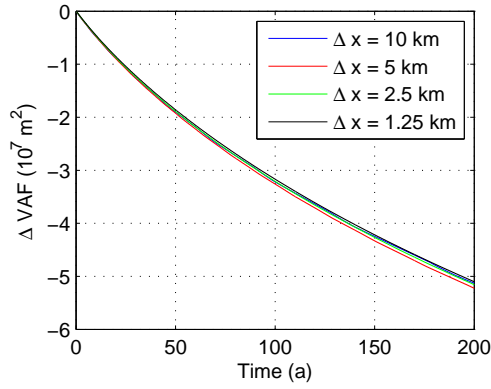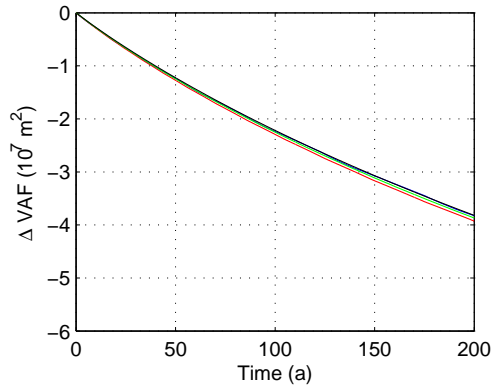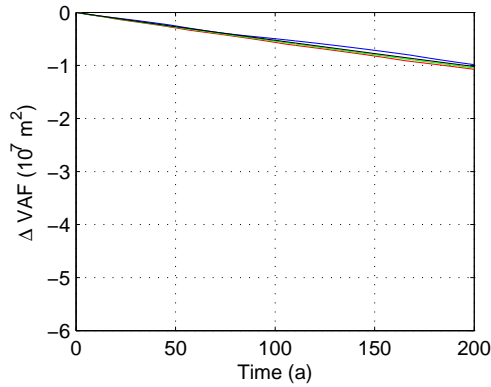
(a) $C_F = 1$

(b) $C_F = 0.8$

(c) $C_F = 0.5$

Figure 3.10: *Change in VAF as a function of time for SSA-H-FG with spatial resolutions of 10, 5, 2.5 and 1.25 km.*

4

Grounding-line migration on long time scales

A major deficiency of the Marine Ice Sheet Model Intercomparison Project (MISMIP) experiments was the limited data output every 50 years, which is insufficient for a proper transient analysis [Pattyn and others, 2012]. Furthermore, in order to render the perturbations more realistic, we performed experiments starting from a slightly different geometry than the MISMIP setup and perturbed the ice sheet by changes in sea level. The aim of this study is to compare the behavior of flowline models that have different physical and numerical approaches with respect to dynamical processes at the grounding line in steady-state and transient phases. We show that: (1) different steady-state ice-sheet profiles are obtained with the same initial setup, partly due to the inclusion of vertical shear stress in the full-Stokes model; (2) the overall response of the different ice-sheet models to the sea-level perturbations is found similar in terms of grounding-line position, ice thickness and ice flux; (3) SSA-H-FG and FS-AG have an oscillating behavior due partly to the grid size for both models and to the heuristic rule for the former model; (4) the implementation of the heuristic rule at the grounding line (linear interpolation of ice flux) by VUB1 model improves the results in terms of grounding-line migration. [1]

Intercomp.
4 models
SS/Transient
Sea level
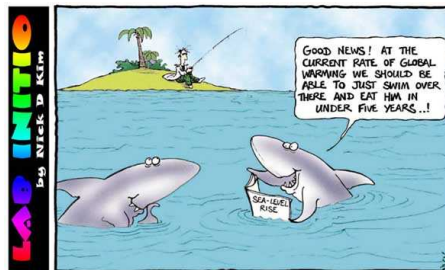
4.1   Introduction

The experiments presented in this chapter are a follow-up of the Marine Ice Sheet Model Intercomparison Project (MISMIP, Pattyn and others [2012]) and were performed prior to the buttressing experiments described in the previous chapter (Chap. 3) with the same group of people (ULB, LGGE and BAS). However, we decided to include this chapter here because the previous chapter, in which the same models are used, has been published in a journal. The aim of the experiments is to compare grounding-line steady-state and transient behaviors between different flowline ice-sheet models, i.e. the full-Stokes finite-element model Elmer/Ice [Durand and others, 2009a], two finite-difference fixed-grid models using the Shallow-Shelf Approximation (SSA), one with the Pollard and DeConto [2009] heuristic rule [Docquier and others, 2011] and the other one without this rule [Drouet and others, 2013], and an SSA Pseudo-Spectral Moving Grid (PSMG) model. Those four ice-sheet models, which differ through the implemented physics, the numerical approach, as well as the grounding-line treatment, are respectively labeled FS-AG, SSA-H-FG, SSA-FG and SSA-PSMG, as in Drouet and others [2013]. The only difference with Drouet and others [2013] is that the model time steps are 0.5, 1, 5 and 10 years for FS-AG, SSA-H-FG, SSA-FG and SSA-PSMG respectively. Results are verified against the Schoof [2007a] semi-analytical solution.

A major deficiency of the MISMIP experiments was the data rendering every 50 years, which is insufficient for a proper transient analysis. Furthermore, moving grid models did not output all grounding-line flux data as was requested for fixed and adaptive grid models. Therefore, a more extensive output scheme is proposed here with output every time step (instead of fixed time intervals). Moreover, in the MISMIP experiments, the grounding line advanced and retreated following a perturbation in the Glen's flow parameter A. Here, the grounding line migrates with a perturbation in sea level. The initial geometry of the experiments is slightly different from MISMIP and a sea-level perturbation is applied (100 m). The grounding line advances in the case of a 100 m sea-level fall and retreats in the case of a 100 m sea-level rise.

Section 4.2 gives the parameter setting, Section 4.3 describes the experiments, and Section 4.4 discusses the main results.

4.2   Parameter setting

The parameters used to perform these experiments are given in Table 4.1, similar to Drouet and others [2013], except that basal friction coefficient $C = 10^7$ Pa m$^{-1/3}$ s$^{1/3}$ and buttressing factor $C_F = 1$ (kept to this value in all experiments). This means that friction at the bed is higher (lower basal sliding) and no buttressing is exerted by the ice shelf.

The basal sliding law is given by $\tau_b = C |u_b|^{m-1} u_b$ where τ_b is the basal shear stress, u_b is the basal velocity and m is the basal friction exponent, as in Drouet and others [2013].

Table 4.1: *Model parameters*

Parameter	Description	Value	Unit
b	Bed elevation	-x/1000	m
ρ_i	Ice density	900	kg m^{-3}
ρ_w	Water density	1000	kg m^{-3}
g	Gravitational acceleration	9.8	m s^{-2}
A	Glen's law coefficient	1.5×10^{-25}	Pa^{-3} s^{-1}
n	Glen's law exponent	3	
C	Basal friction parameter	10^7	Pa m$^{-1/3}$ s$^{1/3}$
m	Basal friction exponent	1/3	
a_s	Accumulation rate	0.3	m a^{-1}
C_F	Buttressing parameter	1	

4.3 Experiments

From the parameter setting of Table 4.1, the models are first run to build a steady-state ice sheet. Figure 4.1 gives the modeled steady-state geometries, as well as the semi-analytical solution given by Schoof [2007a]. The different results obtained with the four models will be analyzed later (Section 4.4). From this initial steady state, three main types of perturbations are applied.

The first type of perturbation consists of lowering or raising the sea level by 100 m in one step with three different forcing rates[2] r_{sl}, i.e. 50, 10 and 2 mm a^{-1}. With the forcing rate of 50 mm a^{-1}, the 100 m sea-level perturbation is completed within 2000 years. A forcing rate of 10 mm a^{-1} corresponds to a 10 000 year perturbation, and a forcing rate of 2 mm a^{-1} corresponds to 50 000 years. Six experiments are included in this type of perturbation, i.e. a 100 m sea-level fall/rise with a forcing rate of 50 mm a^{-1}, a 100 m sea-level fall/rise with a forcing rate of 10 mm a^{-1}, and a 100 m sea-level fall/rise with a forcing rate of 2 mm a^{-1}.

In the second type of perturbation, the sea level is lowered or raised by 100 m in two steps, so that there is a sea-level variation of 50 m first, then a relaxation, then a variation of 50 m, and finally a steady state is completed. The same forcing rates as for the first type of perturbation are used here, so that there are also six experiments for this type (sea-level fall/rise and three different forcing rates).

The third type of perturbation consists of varying the sea level by 100 m in four steps of 25 m with the same scheme of forcing-relaxation as in the second type of perturbation. There are also six experiments for this type, corresponding to the same forcing rates as in the two types

---

[2]The observed rate of global sea-level rise from 1993 to 2009 amounts to 3.3 mm a^{-1} [Nicholls and Cazenave, 2010]. Two of the forcing rates r_{sl} are much higher than this value but the ice-sheet response to sea-level change is very slow, so the r_{sl} values were chosen to provide enough changes in the ice-sheet dimensions.
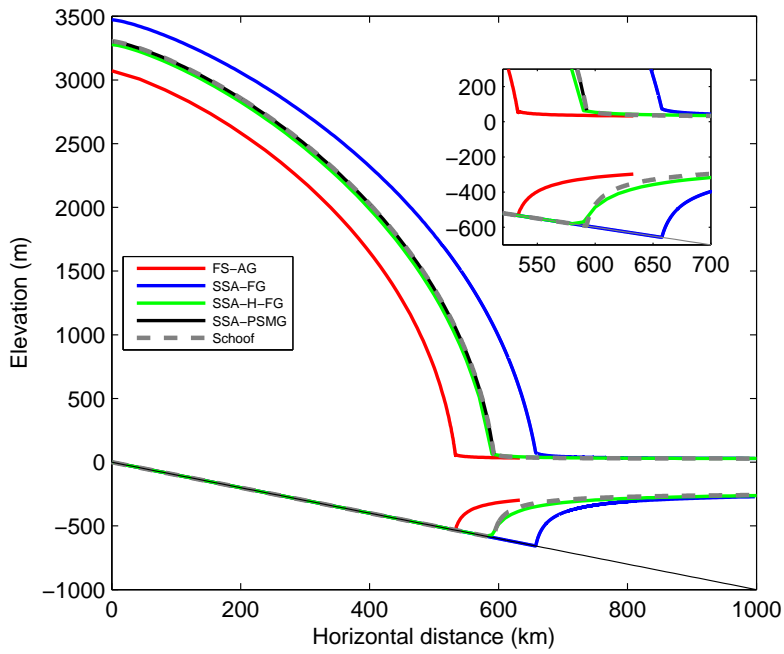
Figure 4.1: *Initial steady-state geometry for all models. The inset emphasizes the differences in grounding-line position.*
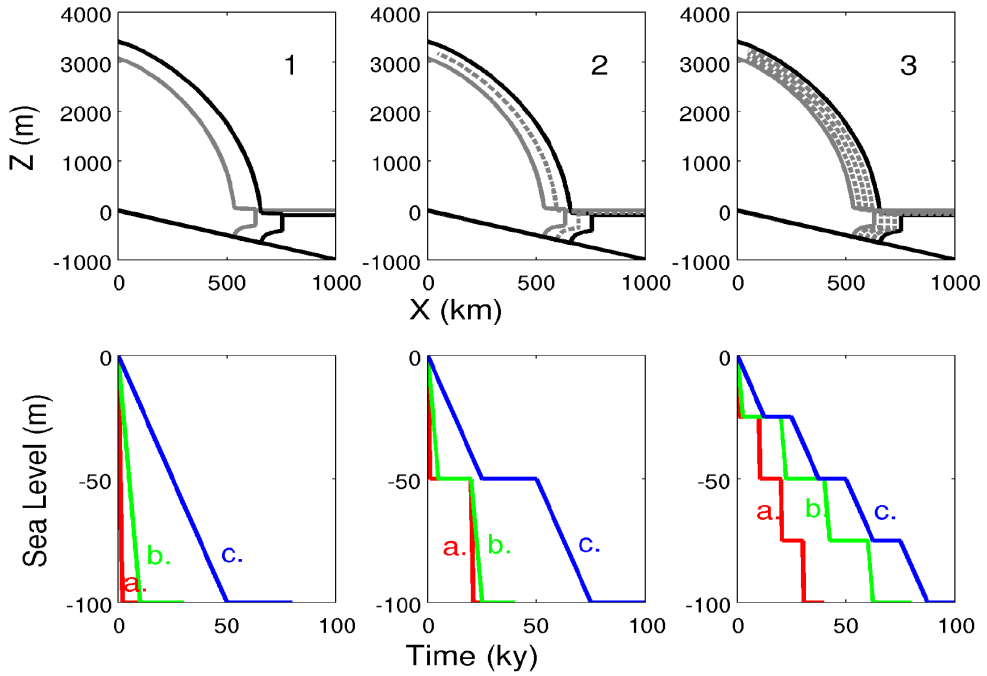
Figure 4.2: *Sea-level fall experiments. The first row shows the initial (solid gray line), the intermediate (dashed gray lines) and the final (solid black line) steady-state ice-sheet profiles along the flowline (Z is the elevation), while the second row provides the sea-level evolution as a function of time (a: $r_{sl} = 50$ mm a^{-1}; b: $r_{sl} = 10$ mm a^{-1}; c: $r_{sl} = 2$ mm a^{-1}). The first column corresponds to the one-step perturbations, the second column to the 2-step perturbations and the third column to the 4-step perturbations [Figure created by A.S. Drouet].*

above.

In total, there are 18 experiments. Figure 4.2 shows a scheme of the 9 sea-level fall experiments. In the end of the perturbations, the models are run to reach a final steady state.

An equation was developed by A.S. Drouet and G. Durand to calculate the sea level z_{sl} at each time step t of the perturbation:

$$z_{sl} = f\left(k_1\left[(t - \left\lfloor \frac{t}{t_f} \right\rfloor t_f)r_{sl} + \left\lfloor \frac{t}{t_s} \right\rfloor r_{sl}t_f\right] + k_2\left\lfloor \frac{t}{t_s} \right\rfloor r_{sl}t_f + k_3\left[\left\lfloor \frac{t}{t_s} \right\rfloor + 1\right]r_{sl}t_f\right) \quad (4.1)$$

where k_1, k_2 and k_3 are coefficients that take into account the number of steps to reach 100 m sea-level variation, t_f is the time during which the forcing is applied, t_s is the subtotal time (forcing + relaxation), f is a coefficient equal to 1 or -1 depending on whether sea level rises

Table 4.2: *Sea-level parameters*

Exp.	r_{sl} (mm a^{-1})	t_f (a)	t_s (a)	Δz_{sl} (m)	f	t_t (a)
Adv11	50	2 000	2 000	-100	-1	100 000
Adv12	50	1000	20 000	-100	-1	120 000
Adv13	50	500	20 000	-100	-1	160 000
Adv21	10	10 000	10 000	-100	-1	100 000
Adv22	10	5 000	20 000	-100	-1	120 000
Adv23	10	2 500	20 000	-100	-1	160 000
Adv31	2	50 000	50 000	-100	-1	150 000
Adv32	2	25 000	50 000	-100	-1	200 000
Adv33	2	12 500	25 000	-100	-1	200 000
Ret11	50	2 000	2 000	100	1	100 000
Ret12	50	1000	20 000	100	1	120 000
Ret13	50	500	20 000	100	1	160 000
Ret21	10	10 000	10 000	100	1	100 000
Ret22	10	5 000	20 000	100	1	120 000
Ret23	10	2 500	20 000	100	1	160 000
Ret31	2	50 000	50 000	100	1	150 000
Ret32	2	25 000	50 000	100	1	200 000
Ret33	2	12 500	25 000	100	1	200 000

or falls respectively.

The values you need to change in the equation are given in Table 4.2 for each experiment, where Δz_{sl} is the total sea-level variation and t_t is the total modeling time, i.e. the time needed to compute the whole experiment with SSA-H-FG and SSA-FG. In the name of experiment (Exp.), 'Adv' means 'grounding-line advance' (i.e. sea-level fall) and 'Ret' stands for 'grounding-line retreat' (i.e. sea-level rise). The first figure after 'Adv'/'Ret' is the forcing rate (1: 50 mm a^{-1}, 2: 10 mm a^{-1}, and 3: 2 mm a^{-1}). The second figure corresponds to the number of steps to reach 100 m sea-level variation (1: 1 step, 2: 2 steps, and 3: 4 steps).

The different steps to perform the simulations are:

1. Use the parameter values from Table 4.1.

2. If possible, use a domain length of 1000 km.

3. Run the model to reach an initial steady state.

4. Perturb the initial steady state by injecting the parameters of Table 4.2 in equation (4.1).

5. Run the model to reach a final steady state.

4.4 Results and discussion

4.4.1 Initial steady state

The initial steady-state geometry is slightly different from one model to the other (Fig. 4.1). The grounding lines provided by SSA-H-FG and SSA-PSMG lie very close to the semi-analytical solution [Schoof, 2007a], while FS-AG grounding line is more than 50 km upstream relative to the grounding line x_s given by Schoof [2007a], and SSA-FG grounding line is more than 50 km downstream. The most upstream position provided by FS-AG, already observed in Chapter 3 ($\sim$ 10 km relative to x_s, see Fig. 3.1) and in Durand and others [2009b] ($>$ 100 km relative to x_s), is probably due to vertical shear stress. FS-AG is a full-Stokes model and includes vertical shear stress, which reduces the effective viscosity, resulting in faster flow, a smaller ice cap and a grounding-line position further upstream. This important result has been recently confirmed by MISMIP3D experiments [Pattyn and others, 2013].

4.4.2 Sea-level perturbations

The global response of sea-level perturbations is very similar for all models with overall grounding-line advance/retreat of $\sim$ 120 km, grounding-line ice thickening/thinning of $\sim$ 30 m, grounding-line ice flux increase/decrease of $\sim$ 40 000 m^2 a^{-1}. SSA-H-FG and SSA-PSMG lie very close to each other, while FS-AG and SSA-FG have lower and higher grounding-line positions, ice thicknesses and fluxes respectively, due to the different initial steady-state ice-sheet profiles. Only results of Exps. Adv11, Ret11, Adv21 and Ret21, corresponding to high (50 mm a^{-1}) and medium (10 mm a^{-1}) forcing rates in one step, are shown in Figures 4.3, 4.4, 4.5 and 4.6 respectively. With lower forcing rate, more time is needed to reach a steady state, but the same results are obtained in the end of the simulations (Fig. 4.7). Perturbing the ice sheet in two or four steps does not change the main results compared to one-step perturbations. All models show a decrease/increase in grounding-line ice thickness (Figs. 4.3(b), 4.4(b), 4.5(b) and 4.6(b)) and flux (Figs. 4.3(c), 4.4(c), 4.5(c) and 4.6(c)) during the forcing stage of the perturbations, followed by an increase/decrease during the relaxation, when sea level falls/rises respectively.

A closer look at the time-dependent response shows differences from one model to the other (Figs. 4.3, 4.4, 4.5, 4.6). Oscillating behavior in grounding-line position, ice thickness and ice flux is present for SSA-H-FG and FS-AG, due to the grid size used for both models and to the heuristic rule for the former model (see Subsection 3.8.2). SSA-FG also presents some flicks due to the grid size but with a much smaller amplitude than SSA-H-FG and FS-AG. SSA-PSMG has a very smooth time-dependent behavior owing to its moving grid. The general patterns in grounding-line change rate are rather similar between the four models with a much higher amplitude for SSA-H-FG concerning grounding-line migration rate (Figs. 4.3(e), 4.4(e), 4.5(e)

and 4.6(e)) and for FS-AG concerning rate of grounding-line ice thickness change (Figs. 4.3(f), 4.4(f), 4.5(f) and 4.6(f)).

A comparison to the semi-analytical solution provided by Schoof [2007a] is also performed (gray curve in Figs. 4.3(d), 4.4(d), 4.5(d), 4.6(d)). All models show a quasi-linear relationship between grounding-line ice flux and ice thickness, with a general trend of going away from the Schoof [2007a] solution and coming back to it.

4.4.3   Improvement of the Pollard and DeConto [2009] heuristic rule

As seen in the results above and in the previous chapter (Chap. 3), the inclusion of the Pollard and DeConto [2009] heuristic rule to enable grounding-line migration with a coarse grid, as in SSA-H-FG model ($\Delta x = 10$ km), gives accurate steady-state results but high amplitude flicks in the time-dependent response. An improvement of this heuristic rule has been performed in VUB1 model [Fürst, 2013]. VUB1 already participated in MISMIP3D [Pattyn and others, 2013] and is an SIA model with SSA for basal sliding in the grounded part, which uses a finite-difference fixed staggered grid (like SSA-H-FG) and 30 vertical layers. The heuristic approach to impose the grounding-line flux is not pursued in the same way as Pollard and DeConto [2009] and Docquier and others [2011] (i.e. SSA-H-FG). Rather than imposing the flux on the adjacent grid point, a linear interpolation of the retrieved grounding-line flux is performed to obtain velocities on the first grounded and first floating grid points. The interpolated velocities obtained from these fluxes and ice thicknesses serve as boundary conditions for basal sliding and for the ice-shelf velocities.

J. Fürst (from the VUB in Brussels) kindly performed Exp. Adv11 with VUB1 model and $\Delta x = 2.5$ km and shared the results with us. They are plotted in Figure 4.8 together with SSA-H-FG results using $\Delta x = 10$ km (same grid size as in Fig. 4.3) and $\Delta x = 2.5$ km (to get the same grid size as VUB1). Initial steady-state geometry is very close to the semi-analytical solution [Schoof, 2007a], especially when using a grid size of $\Delta x = 2.5$ km (Fig. 4.8(a)). The general behavior of grounding-line position (Fig. 4.8(b)), ice thickness (Fig. 4.8(d)) and ice flux (Fig. 4.8(e)) is similar, VUB1 model having slightly higher values in the end of the simulation. Figure 4.8(c) shows that the grounding-line migration is smoother with VUB1 due to the 'interpolated' heuristic rule and that a finer grid size provides more jumps (but smoother behavior) in the same time window.

4.5   Conclusions

Different steady-state ice-sheet profiles are obtained with the same initial setup, partly due to the inclusion of vertical shear stress in the full-Stokes model. Furthermore, the overall response of the different ice-sheet models to the sea-level perturbations is found similar in terms of grounding-line position, ice thickness and ice flux. However, differences between
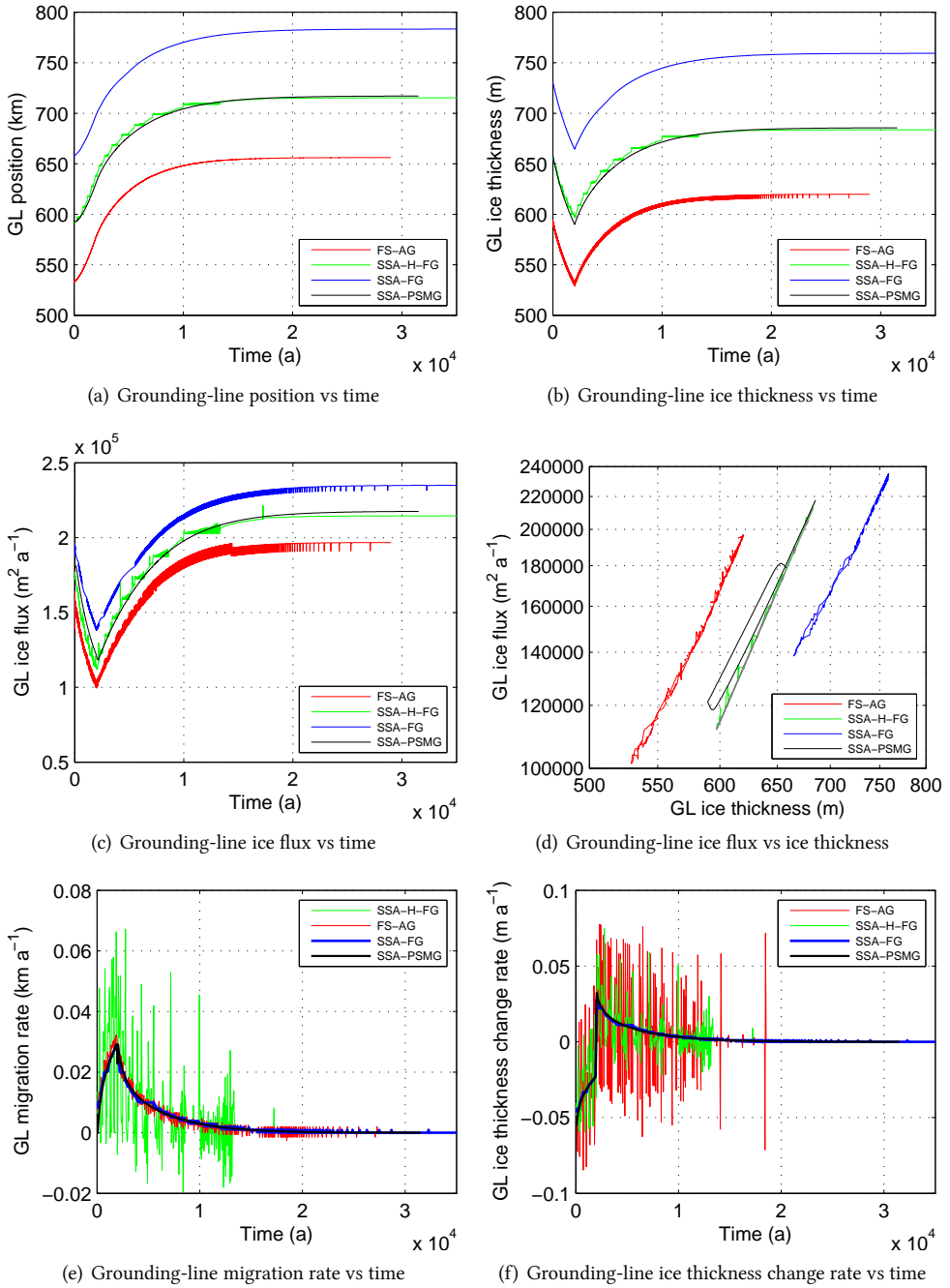
(a) Grounding-line position vs time

(b) Grounding-line ice thickness vs time

(c) Grounding-line ice flux vs time

(d) Grounding-line ice flux vs ice thickness

(e) Grounding-line migration rate vs time

(f) Grounding-line ice thickness change rate vs time

Figure 4.3: *Results of Exp. Adv11 (one-step sea-level fall perturbation with r_{sl} = 50 mm a^{-1}). The gray curve in (d) is the semi-analytical solution [Schoof, 2007a].*
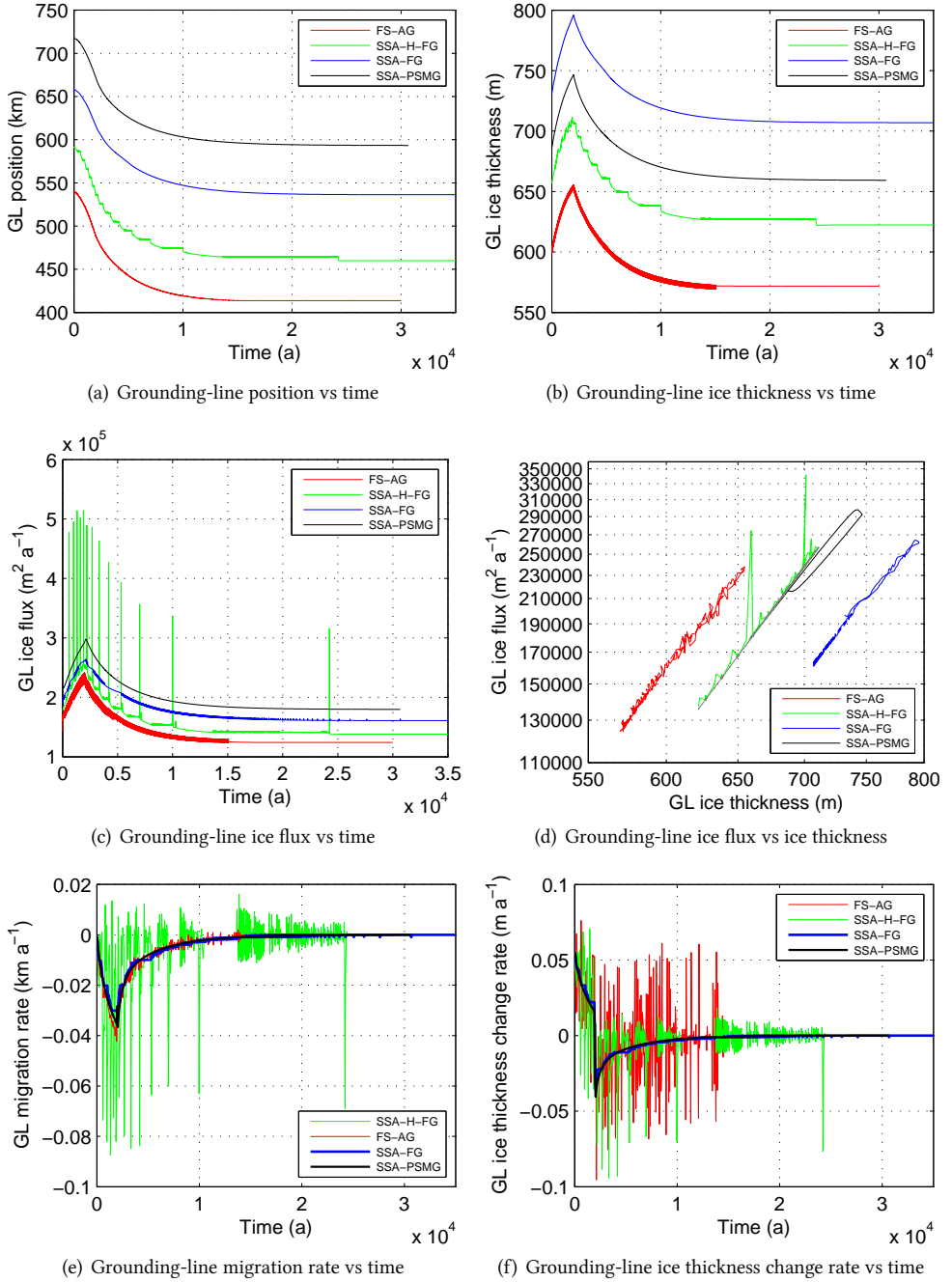
(a) Grounding-line position vs time

(b) Grounding-line ice thickness vs time

(c) Grounding-line ice flux vs time

(d) Grounding-line ice flux vs ice thickness

(e) Grounding-line migration rate vs time

(f) Grounding-line ice thickness change rate vs time

Figure 4.4: *Results of Exp. Ret11 (one-step sea-level rise perturbation with $r_{sl} = 50$ mm a^{-1}). The gray curve in (d) is the semi-analytical solution [Schoof, 2007a].*
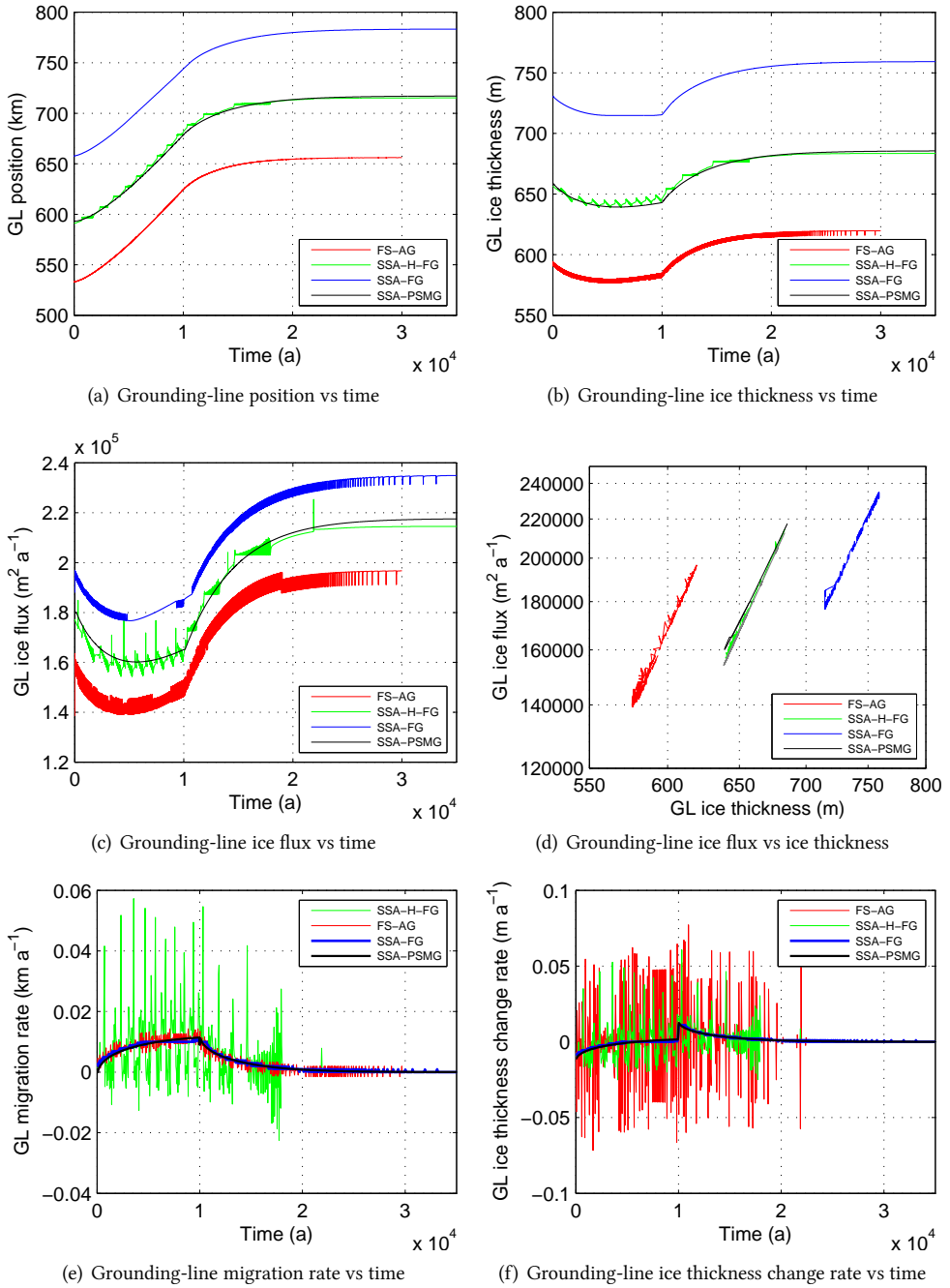
(a) Grounding-line position vs time

(b) Grounding-line ice thickness vs time

(c) Grounding-line ice flux vs time

(d) Grounding-line ice flux vs ice thickness

(e) Grounding-line migration rate vs time

(f) Grounding-line ice thickness change rate vs time

Figure 4.5: *Results of Exp. Adv21 (one-step sea-level fall perturbation with $r_{sl} = 10$ mm a^{-1}). The gray curve in (d) is the semi-analytical solution [Schoof, 2007a].*
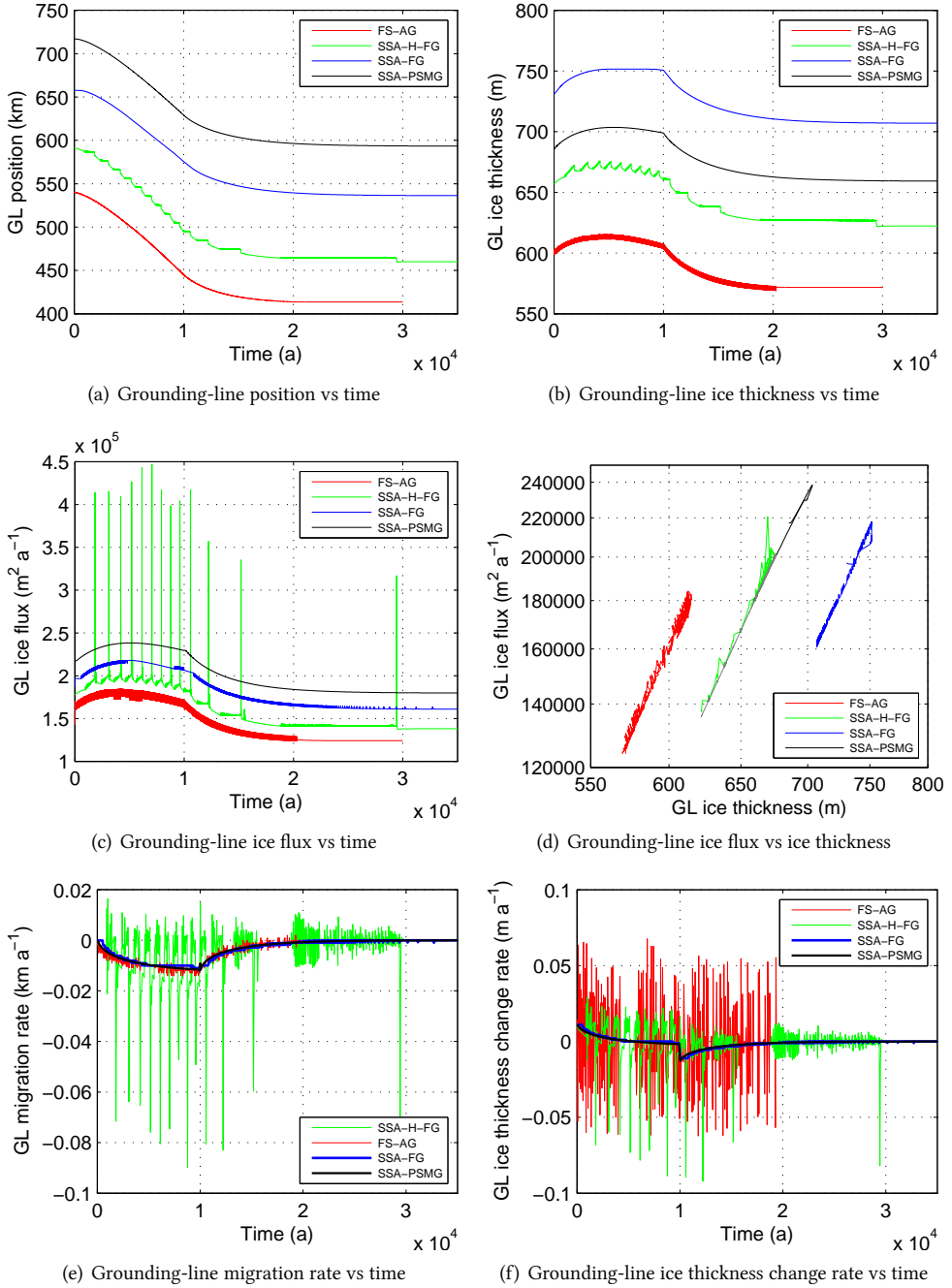
(a) Grounding-line position vs time

(b) Grounding-line ice thickness vs time

(c) Grounding-line ice flux vs time

(d) Grounding-line ice flux vs ice thickness

(e) Grounding-line migration rate vs time

(f) Grounding-line ice thickness change rate vs time

Figure 4.6: *Results of Exp. Ret21 (one-step sea-level rise perturbation with r_{sl} = 10 mm a^{-1}). The gray curve in (d) is the semi-analytical solution [Schoof, 2007a].*

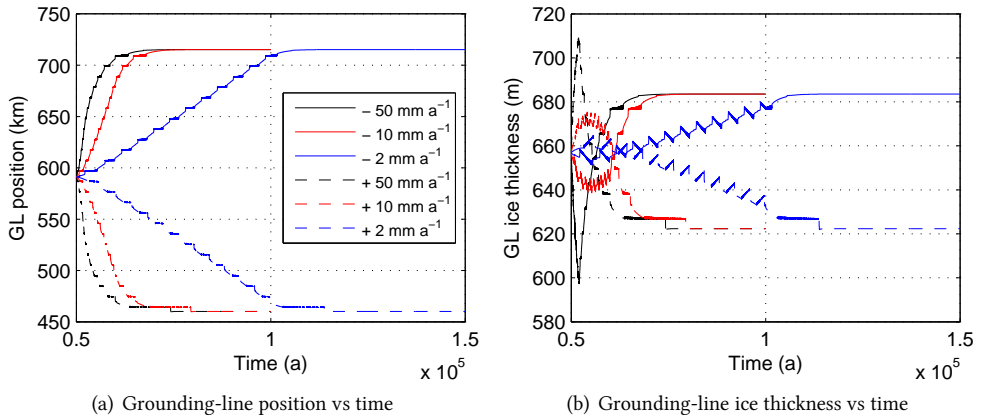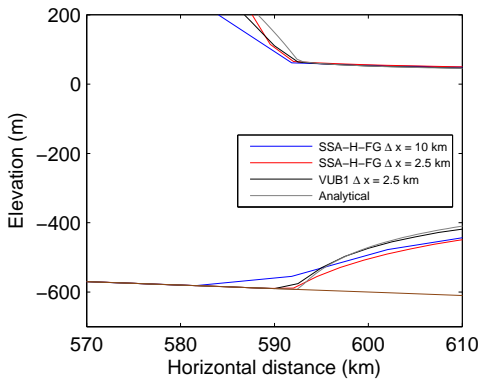(a) Grounding-line position vs time   (b) Grounding-line ice thickness vs time

Figure 4.7: *Grounding-line (GL) (a) position, and (b) ice thickness obtained with SSA-H-FG for the 6 sea-level perturbations corresponding to the first type (sea-level fall and rise in one step).*

models occur with respect to the grounding-line migration rate and thickness change rate (partly explained by the grid size and numerical approaches used). We also find that the implementation of the heuristic rule at the grounding line by VUB1 improves the results in terms of grounding-line migration. Varying the sea level does not provide large grounding-line advances or retreats. That has led us to perform experiments where the buttressing effect is varied instead of sea level (Chap. 3).

We finally emphasize that this study does not take deformational and gravitational effects into account. Using a gravitational sea-level model coupled to a flowline ice sheet-ice shelf model, Gomez and others [2012] find that the sea-level fall at the grounding line associated with a retreating ice sheet acts to slow the retreat.
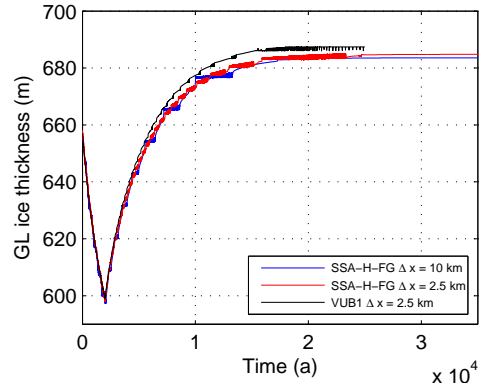
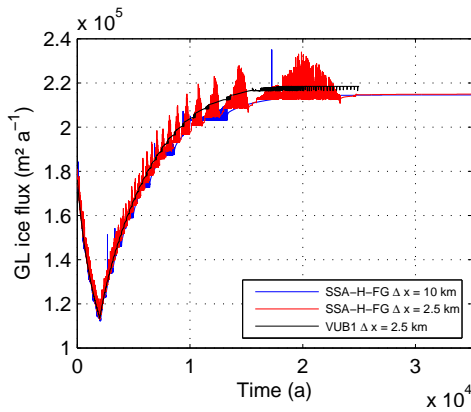(a) Zoom in initial steady-state geometry around the grounding line
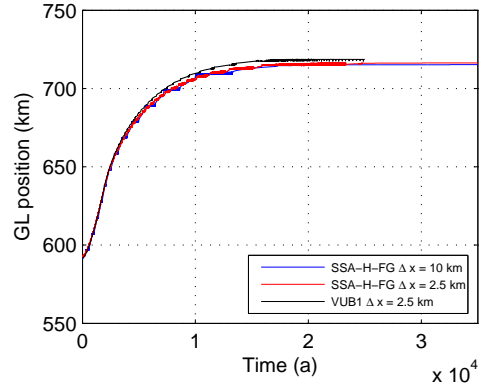
(b) Grounding-line position vs time
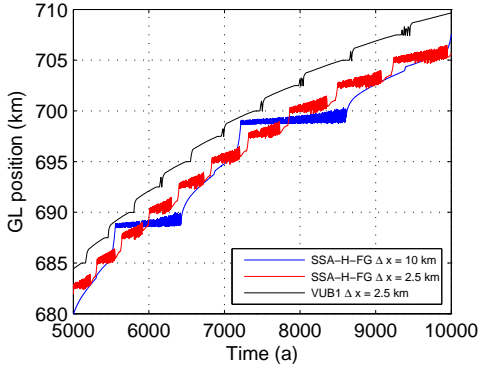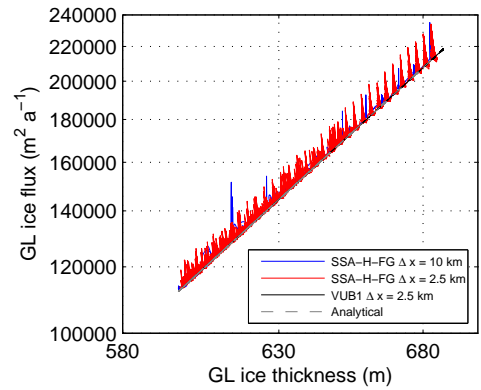
(c) Grounding-line position vs time (zoom)

(d) Grounding-line ice thickness vs time

(e) Grounding-line ice flux vs time

(f) Grounding-line ice flux vs ice thickness

Figure 4.8: *Results of Exp. Adv11 with SSA-H-FG (Δx = 10 and 2.5 km) and VUB1 (one-step sea-level fall perturbation with r_{sl} = 50 mm a^{-1}). VUB1 results were provided by J. Fürst (VUB, Brussels).*

5

Thwaites Glacier grounding-line retreat (flowline modeling)

Major ice loss has recently been observed along coastal outlet glaciers of the West Antarctic Ice Sheet, mainly due to basal melting below the ice shelves. However, uncertainties remain with respect to the behavior of this marine ice sheet implying significant errors in estimating sea-level rise. The stability of a marine ice sheet is controlled by the dynamics of the grounding line, which is the boundary between the grounded ice sheet and the floating ice shelf. Here we use a flowline ice stream-ice shelf model and perform a number of sensitivity experiments applied to Thwaites Glacier to analyze its grounding-line sensitivity on centennial time scales. This glacier is among the fastest and largest ice streams in Antarctica and is a major contributor to current sea-level rise. In the absence of width and buttressing effects, the grounding line retreats at a rate of about 1.5 km a^{-1} in 200 years. With variable glacier width implemented in the model, flow convergence slows the retreat of Thwaites grounding line (0.3 - 1.2 km a^{-1}). The parameterization of ice-shelf buttressing according to different observed scenarios further reduces the glacier retreat and can even lead to a slight advance in the most buttressed case.[1]

---
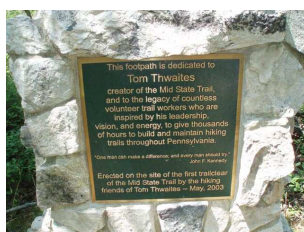
[1]This chapter has been submitted (except Section 5.5, *Supplementary information*) as: Docquier, D., D. Pollard and F. Pattyn. Thwaites Glacier grounding-line retreat: Influence of width and buttressing parameterizations, Submitted to *Journal of Glaciology*.

Own contribution in the paper: writing of publication; literature review; interpolation of data onto model grid; implementation of glacier width in continuity equation; design of experiments; performance of all model runs; interpretation of results; creation of all figures; short stay in Penn State in October-November 2012 to collaborate with DP; presentation of results at AGU 2012; follow-up of C. Delvaux's master thesis [Delvaux, 2013].

5.1   Introduction

Recent satellite observations and techniques, such as satellite laser altimetry, time-variable gravity, and the mass-budget method, have shown that the West Antarctic Ice Sheet (WAIS) has been losing ice at a considerable rate over the recent decades [Rignot and others, 2008; Chen and others, 2009; Rignot and others, 2011; Pritchard and others, 2012]. The primary cause of this recent loss appears to be increased sub-ice shelf melt. Partly due to a shift in wind patterns, substantial volumes of circumpolar deep water penetrate underneath the floating ice shelves of the Amundsen Sea Embayment (ASE) [Thoma and others, 2008; Pritchard and others, 2012]. The subsequent high basal melt rates lead to a thinning of the ice shelves, which reduces their restraint (the so-called 'buttressing effect') on inland glaciers [Dupont and Alley, 2005]. Loss of buttressing has increased the flow rate of inland outlet glaciers and thus grounded ice-sheet loss, contributing to sea-level rise [Rignot and others, 2011].

WAIS has a bed well below sea level and generally sloping upwards towards the ocean ('retrograde' bed slope). In such a situation, the grounding line, defined as the boundary between the grounded ice sheet and the floating ice shelf, is unstable if the ice shelf is freely floating, at least in flowline models with no transverse variations [Weertman, 1974; Schoof, 2007a]. Attention has been paid to WAIS due to this possible instability and to the observational evidence that glaciers have been retreating inland.

Located in the ASE, Thwaites Glacier (TG) is one of the largest, fastest-flowing and fastest-thinning glaciers of the WAIS. Together with Pine Island Glacier (PIG), it drains ∼20% of the WAIS and significantly contributes to current Antarctic ice-sheet loss and thus sea-level rise [Rignot and others, 2008]. TG has two distinct floating ice masses: TG Tongue, downstream of the central area of fastest flow and providing limited buttressing to the inland ice [Rignot, 2008; Parizek and others, 2013], and the eastern ice shelf, where the velocities are much lower than in the tongue due to the presence of a pinning point [Tinto and Bell, 2011]. In 2010, a major part of TG Tongue calved, although there is still an ice melange linking the new iceberg (> 2000 km^2) and the smaller remaining ice tongue [MacGregor and others, 2012]. If the eastern ice shelf would calve, as TG Tongue did in 2010, the buttressing provided by the pinning point would be lost.

Several modeling efforts have been carried out on PIG, and to a lesser extent on TG. Joughin and others [2010a] 3D Shallow-Shelf Approximation (SSA) model indicates that the grounding-line retreat rate of PIG should diminish soon but the glacier will continue to lose mass at rates comparable to the present. In another study of PIG, Gladstone and others [2012a] couple their flowline SSA model to an ice-shelf cavity circulation model [Olbers and Hellmer, 2010], predicting a monotonic retreat of the grounding line over the next 200 years with large uncertainty in the retreat rate. They use parameterized mass balance and basal friction coefficient, and constant Glen's flow law parameter and channel width. Cornford and others [2013] apply their 3D depth-integrated hybrid finite volume model with adaptive mesh refinement to PIG and show a rapid deglaciation caused by sub-ice shelf melting.

Concerning TG, a recent modeling study by Parizek and others [2013] focuses on the impact of spatial resolution of existing datasets, grounding zone processes, and till rheology on the glacier dynamics. They use an ice stream-ice shelf finite element model with 1.5 and 2.5-dimensional treatments of mass continuity and momentum balance respectively, coupled to an ocean-plume model. They apply the model in flowline mode to the centerline of TG. They show that a bedrock rise, currently forming a pinning point downstream of the grounding line, produces a stable grounding-line position for centuries or longer. This stabilization disappears and TG retreats if the basal friction is reduced and warm water penetrates into the grounding zone, unless the bed is effectively plastic.

Motivated by the relatively small number of modeling studies on TG and its potential threat to future sea-level rise, we performed sensitivity experiments using a variety of datasets (geometry, ice velocity, basal shear stress, ice temperature, sub-ice shelf melt rate, accumulation rate) that we incorporated into a finite difference flowline ice stream-ice shelf SSA model. The approach taken here differs from Parizek and others [2013] in three ways. First, the domain extends upstream all the way to the ice divide between TG and Siple basins, while in Parizek and others [2013] the domain starts at the confluence of TG tributaries where incoming ice flux is specified as a boundary condition. Second, we use the recent bathymetry from Tinto and Bell [2011] and also test the new bed data from Bedmap2 [Fretwell and others, 2013]. Third, we focus on variable-width and buttressing parameterizations. The data and the model used are described first. Then, the different sensitivity experiments are explained. Finally, we present the results of our modeling study as well as a discussion.

5.2 Methodology

5.2.1 Data

This study uses data from a number of different sources. Ice surface elevation is from Bamber and others [2009] 1 km DEM. Grounded ice thickness is interpolated from Holt and others [2006] and Le Brocq and others [2010]. Floating ice thickness is derived from Bamber and others [2009] using a hydrostatic assumption [Griggs and Bamber, 2009]. Bathymetry is from Nitsche and others [2007] and Le Brocq and others [2010], with the addition of Tinto and Bell [2011] bathymetric model. Ice surface velocity u and basal shear stress τ_b are from Joughin and others [2009] and are used to calculate the basal friction coefficient C using a Weertman-type sliding law:

$$C = \frac{\tau_b}{|u|^{m-1}\,u},$$

(5.1)

where m is the basal friction exponent. No consensus has emerged on the most realistic value of m [Gudmundsson, 2011]. In this study, m is set to 1/3, based on prior model experiments with m values in the range 1/8 to 1, seeking the best match with observed modern velocities.

Ice temperature and sub-ice shelf melt rate are prescribed from the modern output of another 3D ice sheet-ice shelf model [Pollard and DeConto, 2012]. Glen's flow parameter *A* is derived from ice temperature using Pollard and DeConto [2012] equation (16), and sub-ice shelf melt rate is calculated from Pollard and DeConto [2012] equation (17). Finally, accumulation rate comes from Van de Berg and others [2006]. All these data are interpolated onto our model grid.

We use exactly the same flowline coordinates as in Parizek and others [2013], which represent the central area of fastest flow. Figure 5.1 shows the flowline used in this study, superimposed on the modern ice velocity map of ASE. The domain length from the ice divide to the calving front is about 580 km. The geometry and velocity profiles derived from the data are shown in Figure 5.2(a), where we can clearly identify the different bedrock highs and lows as well as the overall upward-sloping bedrock. In contrast to Bedmap2 [Fretwell and others, 2013], our dataset identifies a trough in bed elevation under the ice shelf 500 km from the ice divide (Fig. 5.2(b)), which can also be seen in Tinto and Bell [2011] Figure 3b. Other differences in bed elevation (up to 200 m) between both datasets are visible upstream of the grounding line. Since Bedmap2 does not incorporate the recent bathymetric model from Tinto and Bell [2011] and its different features, we use the latter data instead of Bedmap2. The grounding line of TG is located on a small sill about 450 km from the ice divide; with Bedmap2 topography, the grounding line would be 5 km downstream of this sill on a downward-sloping bed (Fig. 5.2). Therefore, simulations using Bedmap2 data would have a slower retreat due to the more stable initial grounding-line position [Schoof, 2007a].

5.2.2   Model description

We use a finite difference flowline ice stream-ice shelf model (vertically integrated) that computes the SSA on a fixed staggered grid, with *x* and *z* being the distance along the flow from the ice divide to the calving front and the elevation above sea level respectively. The model is the SSA-FG model, which stands for 'Shallow Shelf Approximation - Fixed Grid', as used in Drouet and others [2013]. This model has successfully participated in the Marine Ice Sheet Model Intercomparison Project (MISMIP) [Pattyn and others, 2012] under the name 'FPA5'. The grid size needs to be small enough to enable an accurate motion of the grounding line [Vieli and Payne, 2005; Durand and others, 2009b; Docquier and others, 2011; Pattyn and others, 2012, 2013]. In this study, we use a grid size of 50 m, well below the threshold suggested by Gladstone and others [2012a] for PIG.

The use of such a flowline model instead of a 3D model is justified by the fact that some 3D effects can be parameterized (such as the buttressing effect and the flow convergence) and the computation time is much smaller than with a 3D full-Stokes model. Furthermore, the SSA can be used to simulate the behavior of TG and other glaciers in ASE, such as PIG, since vertical shear stress is much less important than longitudinal stress and basal friction for those fast-flowing glaciers [MacAyeal, 1989].
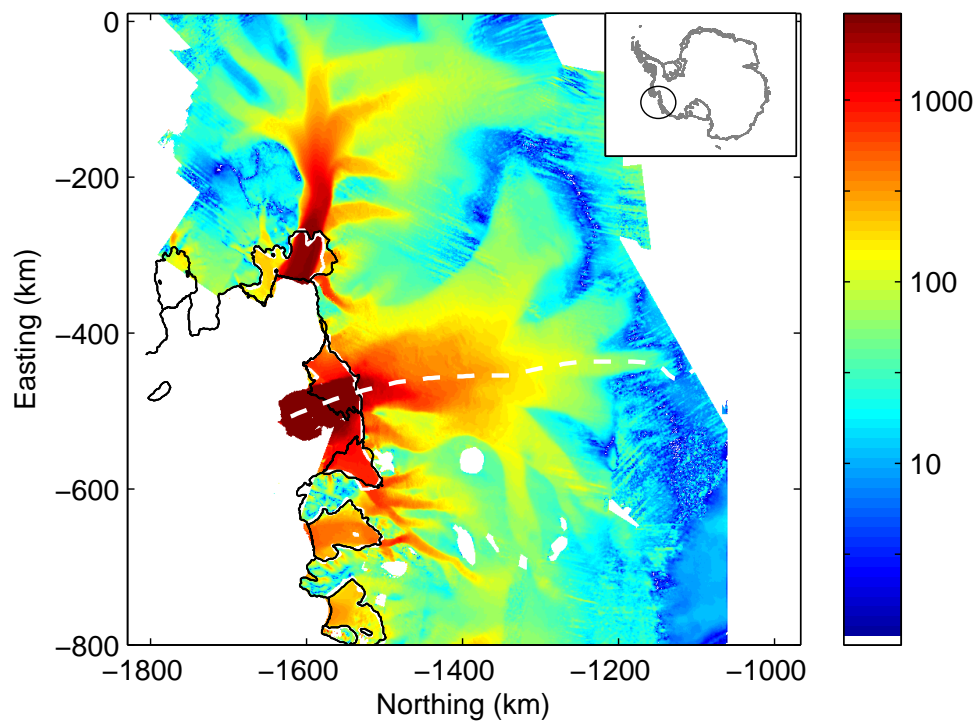
Figure 5.1: *Observed ice velocity (m a^{-1}) of Amundsen Sea Embayment (ASE) [Joughin and others, 2009] with the flowline of Thwaites Glacier used in this study represented as a dashed white line and the Mosaic of Antarctica (MOA) grounding line as a solid black line [Scambos and others, 2007]. The inset shows the location of ASE in Antarctica.*
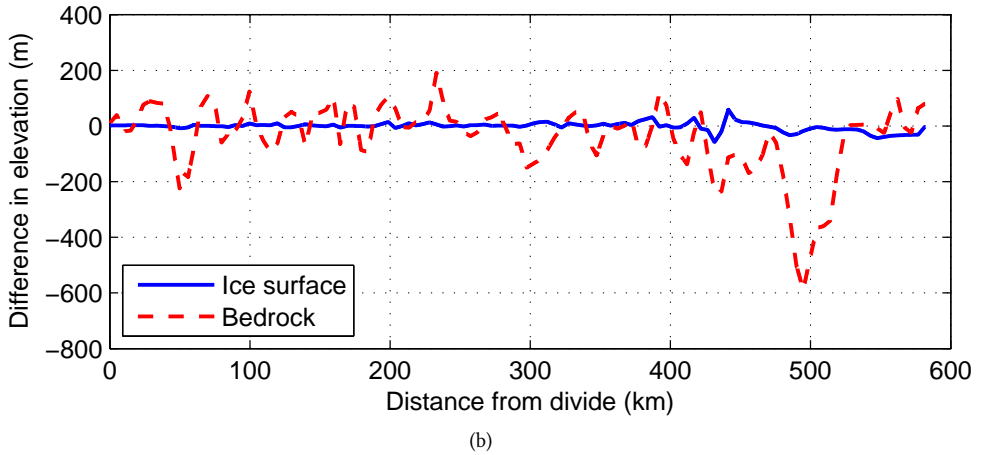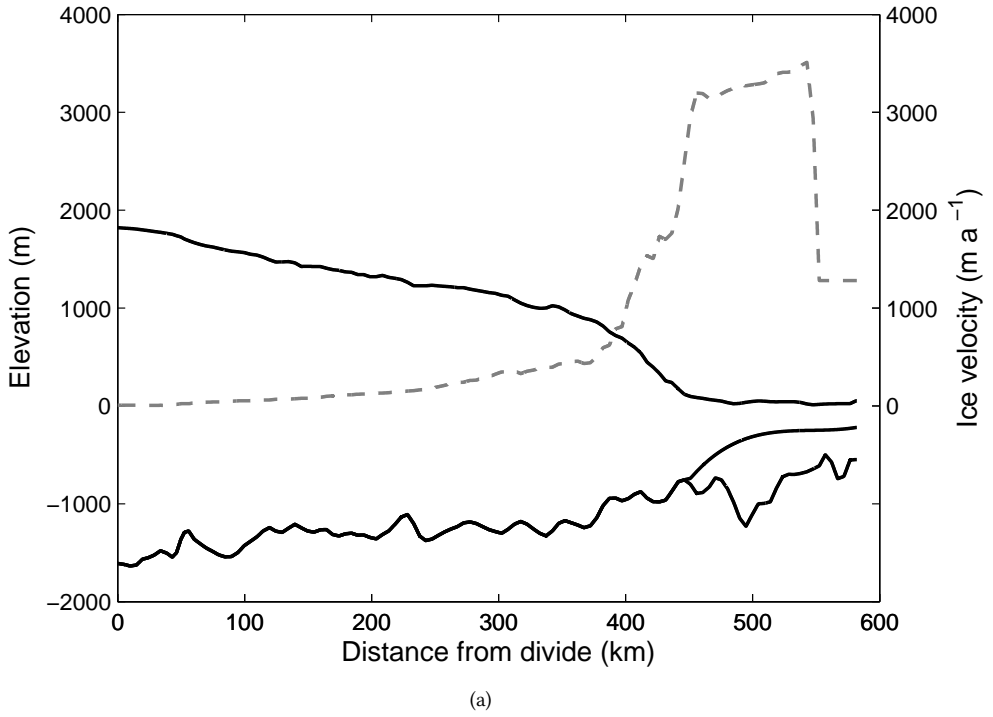
(a)

(b)

Figure 5.2: *(a) Observed geometry (solid black lines) and ice velocity (dashed gray line) profiles of Thwaites Glacier from the ice divide to the calving front with our dataset. (b) Difference in ice surface and bedrock elevations between our dataset and Bedmap2.*

The horizontal velocity u is obtained by solving the following SSA equations (5.2) and (5.3) [MacAyeal, 1989]. In the grounded ice sheet ($0 \leq x \leq x_g$), basal friction is taken in account:

$$2\frac{\partial(h\tau_{xx})}{\partial x} - Cu^m = \rho_i gh\frac{\partial z_s}{\partial x}, \tag{5.2}$$

and in the floating ice shelf ($x_g < x \leq x_f$):

$$2\frac{\partial(h\tau_{xx})}{\partial x} = \gamma h\frac{\partial h}{\partial x}, \tag{5.3}$$

where x_g is the grounding-line position, x_f is the calving front position, h is the ice thickness, $\tau_{xx} = 2\eta\partial u/\partial x$ is the longitudinal deviatoric stress, ρ_i is the ice density, g is the gravitational acceleration, z_s is the ice surface elevation. The effective viscosity η is computed as follows:

$$\eta = \frac{1}{2}A^{-\frac{1}{n}}\left\{\frac{\partial u}{\partial x}\right\}^{\frac{1-n}{n}}, \tag{5.4}$$

where A and n = 3 are the Glen's flow law parameter and exponent, respectively; γ is defined as:

$$\gamma = \rho_i g\left(1 - \frac{\rho_i}{\rho_w}\right), \tag{5.5}$$

where ρ_w is the water density. The boundary condition at the ice divide is $u(x = 0) = 0$, whereas the boundary condition at the ice bottom in the ice sheet is already included in equation (5.2). The horizontal force acting on the calving front is balanced by the hydrostatic water pressure [Paterson, 1994]:

$$\frac{\partial u}{\partial x} = A\tau_{xx}^n = A(C_F\frac{\gamma}{4}h_f)^n, \tag{5.6}$$

where h_f is the ice thickness at the calving front and C_F is the buttressing factor [Drouet and others, 2013]. A value of C_F = 1 means that the ice extension is opposed solely by water pressure, i.e. there is no ice-shelf buttressing. For $C_F < 1$, this induces a lower longitudinal stress at the calving front, simulating the buttressing effect. We model the whole ice shelf since a calving criterion is not implemented.

The ice bottom elevation z_b is determined from the no-penetration condition and the floating condition. For $x \leq x_g$:

$$z_b = b, \tag{5.7}$$

and for $x > x_g$:

$$z_b = \ell_w - h\rho_i/\rho_w > b, \tag{5.8}$$

where b is the bedrock elevation and ℓ_w is the sea-level height.

The ice surface elevation $z_s = z_b + h$ is deduced from the vertically-integrated mass conserva-

tion equation giving h as

$$\frac{\partial h}{\partial t} + \frac{1}{\omega} \frac{\partial (uh\omega)}{\partial x} = \dot{a} - \dot{m}_b, \tag{5.9}$$

where ω is the glacier width, $\dot{a}$ is the ice accumulation rate, and $\dot{m}_b$ is the sub-ice shelf melt rate. The flow convergence and divergence are therefore taken in account through the parameter ω.

The grounding-line position corresponds to the last grounded grid point, which is determined through the flotation criterion.

5.2.3   Sensitivity experiments

The aim of the experiments is to investigate the behavior of TG under varying width and buttressing parameterizations, all mimicking to some extent possible scenarios of present-day and future states. The model is initialized to the modern observed data described above, and is then run to equilibrium with modern climate forcing. After sufficient years of integration, this yields an approximate match between observed and modeled geometry profiles on the one hand, and observed and modeled velocity profiles on the other. The time span of most experiments is 200 years, as used in 'ice2sea' projections [Gladstone and others, 2012a; Hellmer and others, 2012; Drouet and others, 2013]. Unless otherwise mentioned, the buttressing factor $C_F = 1$ (i.e. no ice-shelf buttressing).

In Exp. CW (Exp. and CW stand for 'experiment' and 'constant width' respectively), the glacier width is kept constant over the whole domain (which is equivalent to $\omega = 1$ in equation (5.9)), so that there is no flow convergence. However, in reality, the drainage basin of TG is quite large at the ice divide, and narrows as it approaches the ice shelf. Therefore, a spatially variable glacier width should be used in the continuity equation (5.9). This allows us to take in account the flow coming from the glacier tributaries that feed the main trunk of the glacier. Given the complex flow pattern in the interior of the TG drainage basin, several parameterizations for convergence and divergence of ice flow have been tested, which may all be plausible. Exp. VW1 (VW stands for 'variable width') has the smallest mean glacier width with diverging flow upstream of the zone of convergence noted above. Exps. VW2 and VW3 only have a convergent flow regime, with VW3 having the largest mean glacier width profile. The lateral boundaries of CW, VW1, VW2 and VW3 are shown in Figure 5.3.

In the variable-width experiments (VW1 to VW3), the width at the grounding line increases as the grounding line retreats inland, resulting in flow convergence within the first kilometers of the ice shelf. This tends to generate a thicker ice shelf than is the case with constant width in the shelf. This effect may not be real because the boundaries of shelf flow could shift laterally in different ways as the grounding line retreats. Therefore, we carry out three other experiments, based on VW3 width profile, but keeping the width in the ice shelf constant at each time step. In these experiments, named CSW1, CSW2 and CSW3 (CSW stands for

(a) Exp. CW

(b) Exp. VW1

(c) Exp. VW2
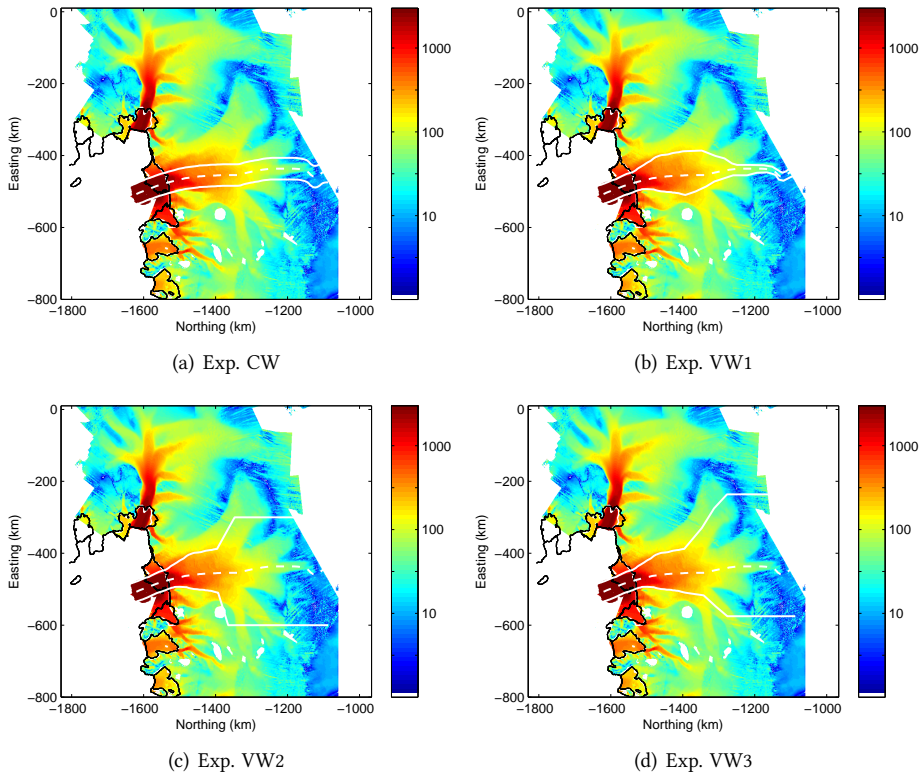
(d) Exp. VW3

Figure 5.3: *Lateral boundaries of Exps. (a) CW, (b) VW1, (c) VW2 and (d) VW3 represented as solid white lines. The colored map shows the observed ice velocity (m a^{-1}) of Amundsen Sea Embayment [Joughin and others, 2009] with the flowline of Thwaites Glacier used in this study (dashed white line) and the MOA grounding line (solid black line) [Scambos and others, 2007].*

Table 5.1: *Summary of experiments*

Exp.	Width	Buttressing
CW	constant	$C_F = 1$
VW1	variable (small)	$C_F = 1$
VW2	variable (medium)	$C_F = 1$
VW3	variable (large)	$C_F = 1$
CSW1	$\omega_s = \omega_g$	$C_F = 1$
CSW2	$\omega_s = (3\omega_g + \omega_c)/4$	$C_F = 1$
CSW3	$\omega_s = (\omega_g + \omega_c)/2$	$C_F = 1$
CF1VW3	variable (large)	$C_F = 0.8$
CF2VW3	variable (large)	$C_F = 0.6$
CF3VW3	variable (large)	$C_F = 0.4$
CF4VW3	variable (large)	$C_F = 0.2$
CF1CSW1	$\omega_s = \omega_g$	$C_F = 0.8$
CF2CSW1	$\omega_s = \omega_g$	$C_F = 0.6$
CF3CSW1	$\omega_s = \omega_g$	$C_F = 0.4$
CF4CSW1	$\omega_s = \omega_g$	$C_F = 0.2$
Bedmap2	$\omega_s = \omega_g$	$C_F = 1$

'constant shelf width'), the ice-shelf width ω_s is equal to ω_g, $(3\omega_g + \omega_c)/4$ and $(\omega_g + \omega_c)/2$ respectively, where ω_g and ω_c are the widths at the current grounding line and calving front respectively.

TG Tongue is known to exert limited buttressing on the inland grounded ice [Rignot, 2008; Parizek and others, 2013] but the eastern ice shelf is in contact with a pinning point [Tinto and Bell, 2011], reducing the flow of inland ice. To simulate the buttressing effect arising from the eastern ice shelf, we reduce longitudinal stress at the calving front in equation (5.6), similar to what is described in Drouet and others [2013], i.e. by lowering the buttressing factor C_F. Exps. CF1VW3, CF2VW3, CF3VW3 and CF4VW3 are based on VW3 width profile and use values of C_F = 0.8, 0.6, 0.4 and 0.2 respectively from the beginning of the simulation to the end. The same values of C_F are used in Exps. CF1CSW1, CF2CSW1, CF3CSW1 and CF4CSW1, which are based on CSW1 width profile. For example, a value of C_F = 0.2 means that the longitudinal stress at the calving front is five times lower than with C_F = 1. This simulates a buttressing increase, caused by lower sub-ice shelf melt for instance, and leads to deceleration of inland grounded ice [Pritchard and others, 2012].

A final experiment is performed with the new Bedmap2 bedrock data based on CSW1 width profile to test what is the difference with the bedrock data used here. The 16 experiments are summarized in Table 5.1.

5.3 Results and discussion

Initialized to modern data, most of the experiments lead to an approximate match between observed and modeled geometry profiles on one hand, and observed and modeled velocity profiles on the other, after 10 model years (Figs. 5.4 and 5.5).

In Exp. CW, the grounding line quickly retreats inland (Fig. 5.4(a)) and the ice-shelf velocities after 50 years reach more than 10 000 m a^{-1} (Fig. 5.5(a) is truncated at 5000 m a^{-1} to be compared to Fig. 5.5(b)), comparable to maximum observed velocities of Jakobshavn Isbrae [Joughin and others, 2004, 2010b]. The grounding line is located on an overall retrograde bed slope, accelerating the glacier retreat, and reaches a position of 153 km from the ice divide after 200 years. This corresponds to a mean retreat rate of about 1.5 km a^{-1}, higher than the observed 1 km a^{-1} [Tinto and Bell, 2011]. We let the model run longer for this experiment and found that the glacier shrinks after 370 years. A contact between the ice shelf and a bedrock rise 550 km from the divide is established after 60 years, which slows down the retreat for about 100 years (Fig. 5.7). Once the grounding line passes the bedrock rise at $x = 220$ km (160 years), the retreat accelerates. This experiment should be considered as an end-member case since buttressing and width variations are not included. An increase in backstress provided by the ice shelf would slow down the grounding-line retreat [Drouet and others, 2013]. A change in the width gradient from the ice divide to the calving front would also provide a slower retreat. Mathematically, the latter corresponds to a reduction of all the width terms in the discrete form of the continuity equation (5.9), reducing the ice flux at the grounding line.

Using a spatially variable glacier width in the continuity equation (Exps. VW1 to VW3) slows the retreat and stabilizes the glacier at a grounding-line position of $x_g \approx 390$ km from the ice divide after 200 years, as can be seen for Exp. VW3 in Figures 5.4(b), 5.5(b) and 5.6(a). The mean width rises from Exp. VW1 to VW3 (Fig. 5.3) but no noticeable difference in GL migration is perceived between the three experiments due to the contact created between the ice shelf and the bedrock rise at $x = 450$ km after 70 years (Fig. 5.7). The variable glacier width of those experiments takes in account the flow coming from TG tributaries (flow convergence and divergence). While the grounding line retreats, the ice-shelf width close to the grounding line increases, thereby increasing the width spatial gradient $\partial \omega / \partial x$. Therefore, the ice shelf gets thicker and makes contact with a pinning point, which slows the retreat and stabilizes the grounding line. In that same experiment, mean grounding-line retreat rate (0.3 km a^{-1}) is lower than the observed 1 km a^{-1} [Tinto and Bell, 2011] and grounding-line thinning rate is comparable to the observations [Shepherd and others, 2010; Pritchard and others, 2012] in the very first years of the simulation, i.e. during the relaxation phase (Fig. 5.6). Those rates substantially increase and vary in time afterwards, due to the position of the grounding line on a retrograde bed slope. Moreover, the grounding line can slightly re-advance (positive migration rates) during the overall retreat process because of the contact between the ice shelf and a pinning point (e.g. between 55 and 60 years), a behavior already simulated by Favier and others [2012] (Fig. 5.6(a)). Some high thickening rates are observed (e.g. 50-55 years) due

to the fast retreat of the grounding line in a region of lower bedrock elevation (Fig. 5.6(b)).

If the ice-shelf width is kept constant (Exps. CSW1 to CSW3), the grounding line retreats much faster than in the experiments with spatially variable width (Exps. VW1 to VW3) and reaches a position of $x_g \approx 220$ km in 200 years, but this retreat is slower than the constant-width experiment (Exp. CW), as shown in Figures 5.4(c) and 5.7. Some stages of slowing down are identified in those three experiments ($\approx$ 60-80 and 100-200 years) and are linked to the grounding line positioned on a bedrock high (Fig. 5.7), confirming a finding from Parizek and others [2013] for TG. A wider ice shelf ($\omega_{CSW1} > \omega_{CSW2} > \omega_{CSW3}$) gives a slightly more retreated grounding-line position (Fig. 5.7). Increasing the width in the ice shelf means that the width spatial gradient between the ice sheet and the ice shelf decreases, providing higher flux and less stabilization. The mean grounding-line retreat rate of those experiments is 1.1 - 1.2 km a^{-1}, closer to the observations than Exps. CW and VW1 to VW3. However, this parallel-sided case is not necessarily more realistic than Exps. VW1 to VW3; as the grounding line retreats, there are prominent highs on either side of the domain that act as pinning points for the new ice shelf, which is not captured by the model. Therefore, marching back with a parallel-sided ice shelf overestimates the vulnerability of TG.

Applying buttressing (experiments starting with 'CF') also reduces the grounding-line retreat compared to Exp. CW (Figs. 5.4(d) and 5.8). This can be compared to the results previously obtained in Drouet and others [2013]. As a matter of fact, an increase of buttressing effect (through a decrease in C_F) lowers ice flux at the grounding line and therefore provides a slightly more advanced grounding-line position. Furthermore, combining those buttressing increases with VW3 parameterization (variable width) leads to less grounding-line retreat than with CSW1 parameterization (constant shelf width), as shown in Figure 5.8. An extreme case (CF4VW3, i.e. C_F = 0.2) shows a final grounding-line position some km downstream the observed one. As for the CSW1-CSW3 experiments, bedrock highs tend to stabilize the grounding-line position for some years (Fig. 5.8).

Using Bedmap2 for the bed (with CSW1 width profile and $C_F = 1$) provides a final grounding-line position of $x_g \approx 440$ km (after 200 years), i.e. on a bedrock high very close to the initial position (Fig. 5.4(e)). This behavior is completely different from Exp. CSW1 that uses the same parameters but not the same bedrock elevation, and is in agreement with Parizek and others [2013] results. Both Bedmap2 and Parizek and others [2013] do not include Tinto and Bell [2011] bathymetric model, wich may explain why the grounding line does not retreat as much. Indeed, the slightly different bedrock geometry in the vicinity of the grounding line between both datasets plays a non-negligible role in the behavior of TG. The initial grounding line is located on a small sill with our dataset while 5 km downstream this sill with Bedmap2 (Fig. 5.2).

Figure 5.9 shows the wide spread of grounding-line migration rates for the width and buttressing experiments. The highest retreat rates (more than 15 km a^{-1}) are modeled with a constant width in the whole domain (Exp. CW) as well as with constant shelf width experiments (Exps.

CSW1 to CSW3 and CF1CSW1-CF2CSW1). More realistic rates are modeled with variable-width experiments (Exps. VW1 to VW3). The final grounding-line position obtained in all the 16 experiments performed in this study is shown in Figure 5.10. Four experiments (CW and CSW1 to CSW3) lead to a grounding-line retreat more than 200 km in 200 years (i.e. mean retreat rate of ≥ 1 km a^{-1}). All simulations show a retreat of the grounding line, except the simulations with high ice-shelf buttressing combined with a non-constant shelf width (CF3VW3 and CF4VW3) and the one including Bedmap2 data. Almost all simulations lead to a contact between the ice shelf and a pinning point. The location of those pinning points is indicated through the color code in Figure 5.10.

5.4 Conclusions and outlook

The short time-scale response of TG (200 years) was computed with an SSA flowline ice stream-ice shelf model and all the available data (geometry, ice velocity, basal shear stress, ice temperature, sub-ice shelf melt rate, accumulation rate). All simulations show a retreat of the grounding line with some stages of slowing down, except two simulations with high ice-shelf buttressing combined with a variable ice-shelf width and the simulation using Bedmap2 data. We identify that the retreat is greatly slowed when the effect of flow convergence is included, i.e. using a variable glacier width in the continuity equation, leading to reduced grounding-line retreat rates on downward-sloping portions of the bed. The way this width is parameterized produces different results in terms of grounding-line migration and ice velocity. A convergence in the ice shelf decreases the ice flux and tends to stabilize the grounding line, while a constant ice-shelf width leads to speed up and grounding-line retreat. Moreover, the parameterization of buttressing also affects grounding-line position. Our experiments show that if we do not take in account buttressing, this can lead to a drastic grounding-line retreat (300 km in 200 years in the constant-width experiment).

These experiments were performed using a flowline model, which considerably reduces the computation time compared to a three-dimensional model. However, buttressing and width parameterizations used here should be compared to a three-dimensional model that includes these effects. In this study, we also assume that an SSA model works well for TG as it is a fast-flowing glacier. However, there may be a contribution from vertical shear that could slow down the ice flow. SSA models only include membrane stresses and are faster in their response than models including both membrane stresses and vertical shearing [Pattyn and others, 2013].

5.5 Supplementary information

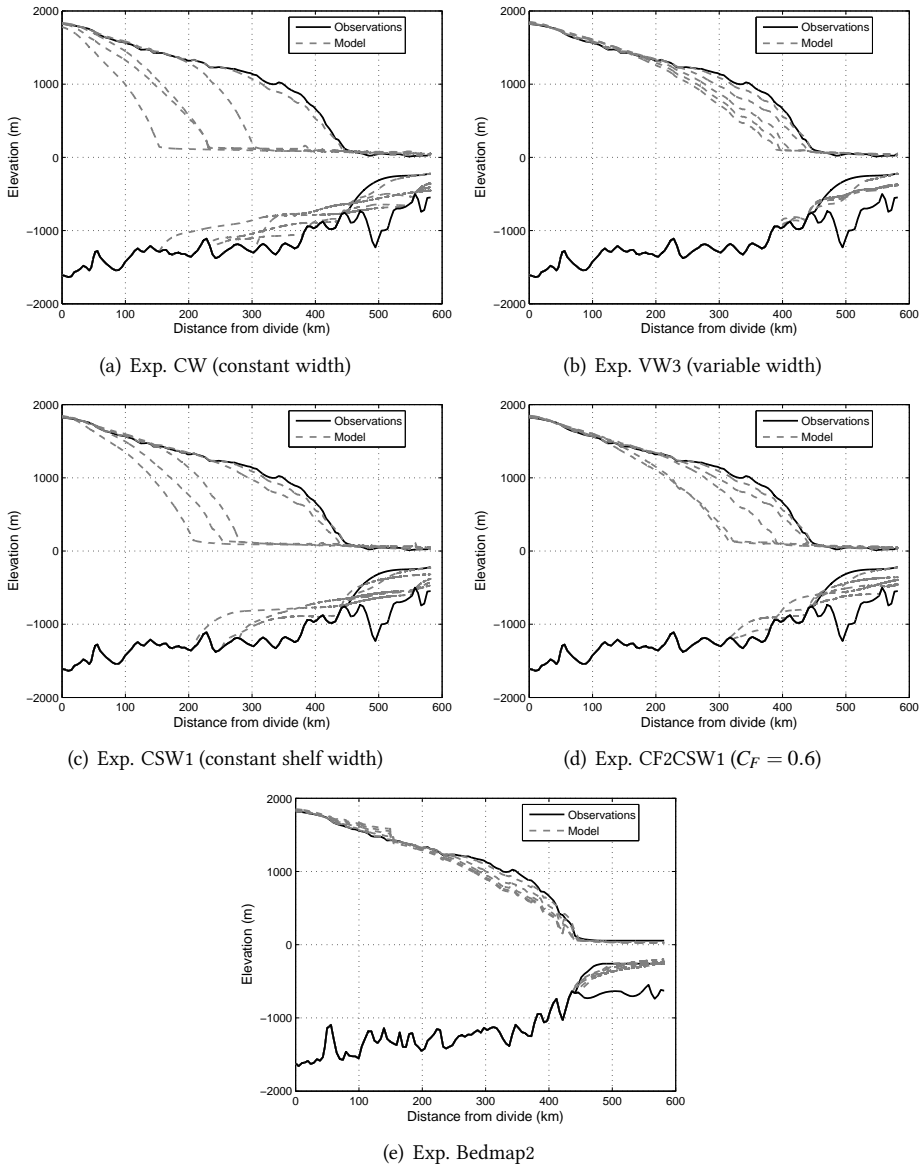The supplementary information below is not part of the article.

(a) Exp. CW (constant width)

(b) Exp. VW3 (variable width)

(c) Exp. CSW1 (constant shelf width)

(d) Exp. CF2CSW1 ($C_F = 0.6$)

(e) Exp. Bedmap2

Figure 5.4: *Modeled geometry profiles of Thwaites Glacier after 10, 50, 100, 150 and 200 years (from right to left) and observed geometry profile.*

(a) Exp. CW (constant width)   (b) Exp. VW3 (variable width)
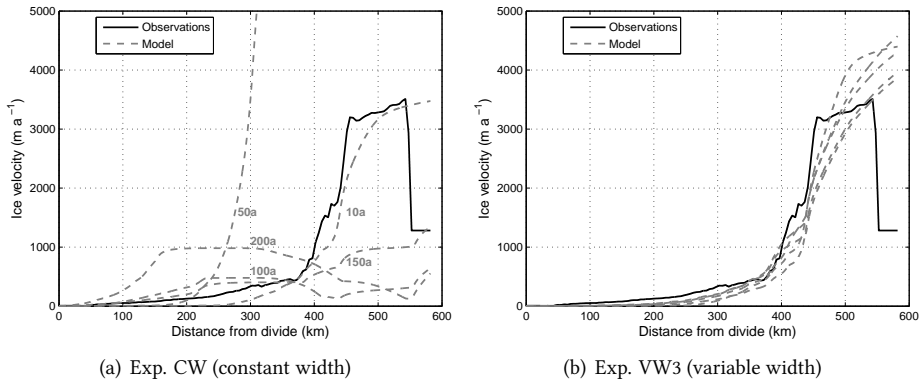
Figure 5.5: *Modeled velocity profiles of Thwaites Glacier after 10, 50, 100, 150 and 200 years (labeled for (a) Exp. CW and from left to right for (b) Exp. VW3). The velocity profile of (a) is truncated at 5000 m a^{-1} to be compared to (b).*
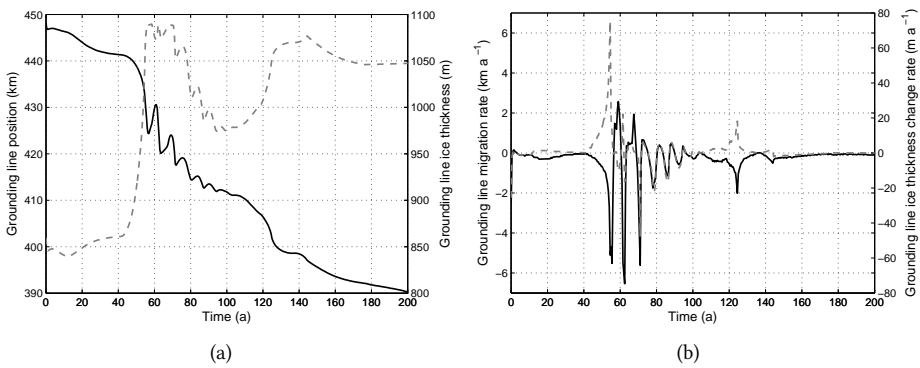

(a)   (b)

Figure 5.6: *Results of Exp. VW3: (a) grounding-line position (solid black line) and ice thickness (dashed gray line); (b) grounding-line migration rate (solid black line) and ice-thickness change rate (dashed gray line).*
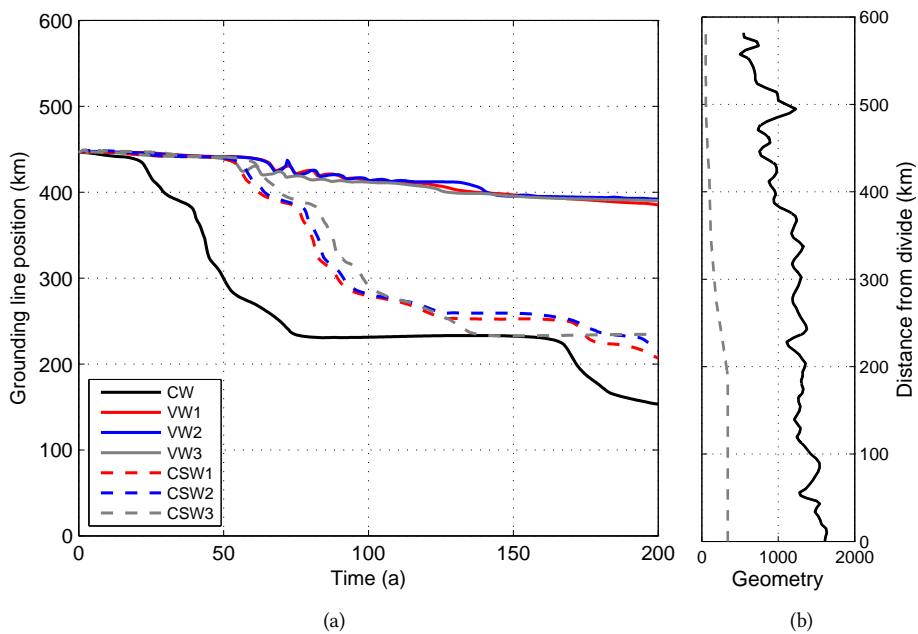
Figure 5.7: *(a) Thwaites grounding-line position as a function of time for the width experiments. (b) Bedrock depth (m, solid black line) and VW3 width (km, dashed gray line).*
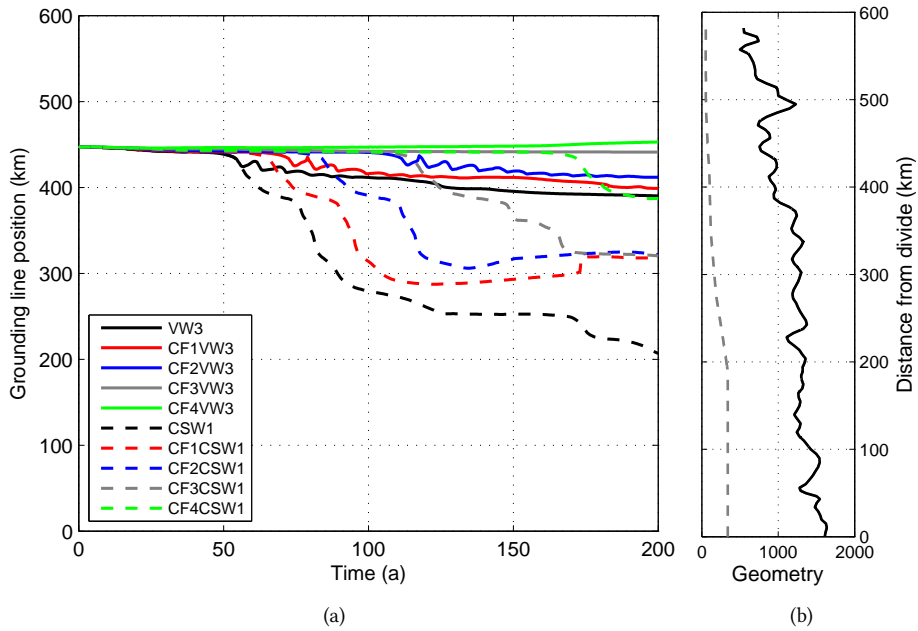
Figure 5.8: *(a) Thwaites grounding-line position as a function of time for the buttressing experiments. (b) Bedrock depth (m, solid black line) and VW3 width (km, dashed gray line).*
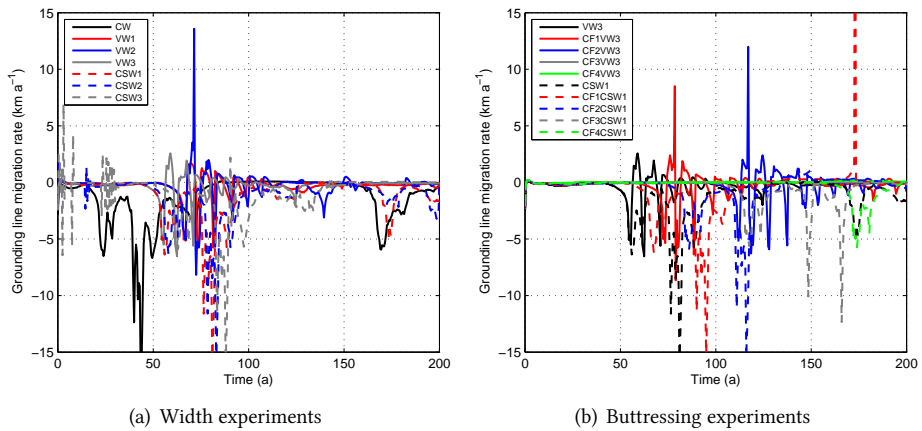

Figure 5.9: *Thwaites grounding-line migration rate as a function of time for the (a) width and (b) buttressing experiments.*
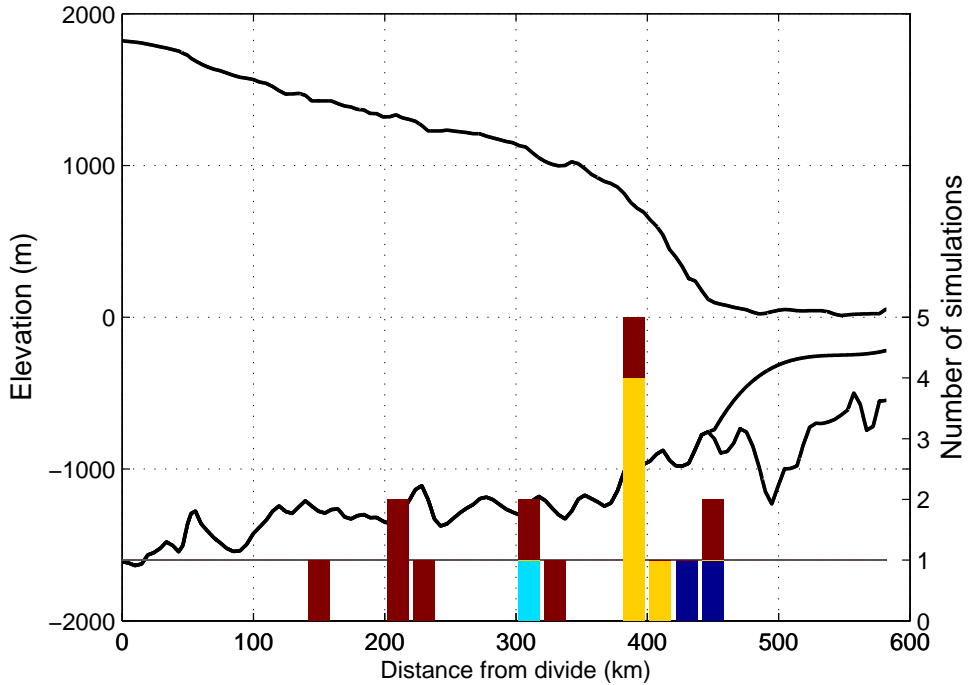
Figure 5.10: *Observed ice sheet-ice shelf geometry of Thwaites Glacier along with a frequency histogram of model simulations binned by final grounding-line position (within a range of 20 km). Blue bars show frequency of 'non-pinned shelf' simulations, while other colors show frequency of 'pinned shelf' simulations, i.e. simulations with an ice shelf in contact with a pinning point (PP) in the end of the simulation, as in Gladstone and others [2012a]. The different colors indicate where the ice shelf makes first contact with a PP (cyan: PP location ≈ 380 km from the divide, yellow: PP location ≈ 450 km, dark red: PP location ≈ 555 km).*

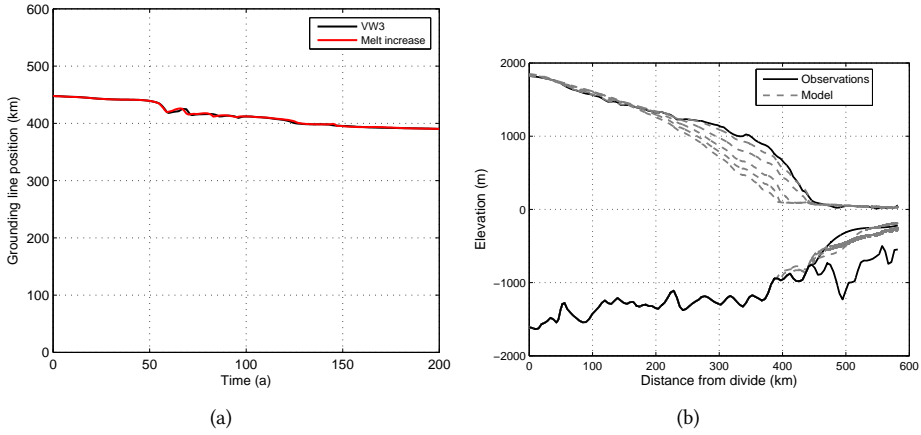**Figure 5.11**: *Thwaites Glacier (a) grounding-line position as a function of time for Exps. VW3 and basal melt increase (+ 5 m a^{-1}) and (b) modeled geometry profiles for the basal melt increase experiment after 10, 50, 100, 150 and 200 years (from right to left). The observed geometry profile is also shown.*

5.5.1 Effect of flow convergence

Grounding-line retreat is slowed down when there is a flow convergence, i.e. when the width decreases from upstream to downstream regions. This can be mathematically demonstrated, as explained in Section 5.3, by using equation (5.9). If glacier width ω decreases along flow, the ice flux divergence becomes negative ($\partial(uh\omega)/\partial x < 0$), which leads to an increase in ice thickness from one time step to the other ($\frac{\partial h}{\partial t} > 0$) in order to keep the same mass balance ($\dot{a} - \dot{m}_b$).

5.5.2 Additional experiment

An additional experiment is performed with exactly the same parameters as Exp. VW3, except that sub-ice shelf melt rate $\dot{m}_b$ is increased by 5 m a^{-1} from the grounding line to the calving front. Basal melt is indeed responsible of major ice loss in the ASE (Fig. 1.5) and we try to understand how it affects the response of the grounding line of TG. As we can see in Figure 5.11(a), no grounding-line retreat is observed but the ice shelf gets thinner than the ice shelf of Exp. VW3 (compare Figs. 5.11(b) and 5.4(b)).

In reality, while the melt under the ice shelf increases, the buttressing effect is progressively lowered. Therefore, an experiment combining sub-ice shelf melt increase and buttressing loss should be performed to render the experiment more realistic. However, the buttressing parameter in the experiment above is already set to $C_F = 1$. A loss of buttressing would mean that this factor would become greater than 1, which is above the upper limit of this parameter. It could be explained by some slow-moving ice adjacent to an ice stream, where the fast flow

in the ice stream causes the ice shelf to pull on the slow-moving ice next to it (Hindmarsh, Personal Communication, 2013). In the absence of any real physical explanation, we did not perform such an experiment.

6

A three-dimensional modeling study of Thwaites Glacier

Here we use a three-dimensional (3D) ice stream-ice shelf model that solves the Shallow-Shelf Approximation (SSA) on a staggered grid and perform sensitivity experiments applied to Thwaites Glacier to improve our analysis of its grounding-line sensitivity on decadal time scales. The use of full-plane observations results in a much slower grounding-line retreat when compared to a bedrock that is laterally extruded (i.e. laterally repetition of the central flowline). Lateral variations in bedrock elevation have an important impact on the glacier behavior, as downward-sloping portions of the bedrock provoke slowing down of the grounding line. The general upward-sloping bedrock of Thwaites Glacier is further enhanced when smoothing the bedrock over a certain distance, leading to faster retreat.[1]

> Thwaites
> 3D SSA
> Transient
> Bedrock
> Width

---
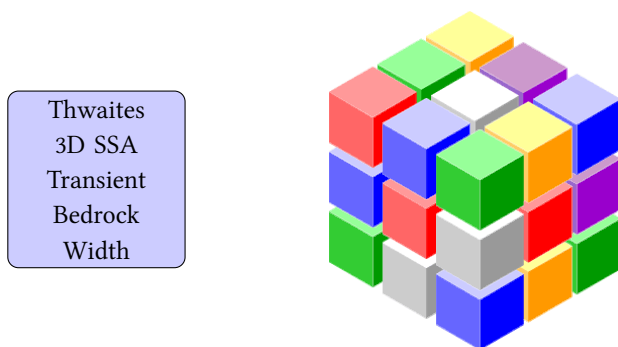
[1]This chapter has not been submitted in a journal and follows a short stay in Penn State in October-November 2012 to work with David Pollard.

6.1   Introduction

As previously mentioned (Chap. 5), the Amundsen Sea Embayment (ASE) is particularly vul-
nerable to warm ocean waters, leading to increased basal melt under the ice shelves and
acceleration of inland grounded ice through buttressing loss [Pritchard and others, 2012].
Furthermore, the ASE is subject to the marine ice-sheet instability hypothesis [Weertman,
1974; Schoof, 2007a] with a bedrock below sea level and sloping upward towards the ocean.
Thwaites Glacier (TG) has this configuration and significantly contributes to current Antarctic
ice-sheet loss [Rignot and others, 2011]. Therefore, it is essential to know how the glacier will
evolve in the near future.

In Chapter 5, the effect of ice-shelf buttressing is parameterized as a function of longitudinal
stress at the calving front. There is no buttressing parameterization in the present chapter
due to the three-dimensional (3D) nature of the model used, which accounts for variations in
stresses in both horizontal dimensions. Using such a 3D model, it is possible to find stable
steady-state grounding-line positions on retrograde bedrock slopes (upward-sloping towards
the ocean) due to the presence of buttressing [Gudmundsson and others, 2012].

Sensitivity experiments are performed on TG with three different bedrock configurations and
a constant glacier width. The aim is to understand what is the impact of bedrock topogra-
phy on grounding-line migration and where the differences with the flowline model used in
Chapter 5 come from. First, the methodology (data, model and experiments) is explained. Sec-
ond, we show the results of the experiments before concluding. Finally, as this is an ongoing
research, we give a large outlook of what could be further made to improve the study.

6.2   Methodology

6.2.1   Data

Model inputs here are similar to the previous flowline study (Chap. 5), except that Glen's
flow coefficient A is not calculated from ice temperature but kept constant in the ice sheet and
in the ice shelf for reasons of model stability (Tab. 6.1). Geometry data (surface and bedrock
elevations, grounded and floating ice thicknesses) and basal melt rate $\dot{m}_b$ come from full-plane
observations (same data as in Chap. 5) and are bi-linearly interpolated onto our model grid.
Basal friction coefficient C and accumulation rate $\dot{a}$ also come from full-plane observations for
the central flowline and are laterally extruded, i.e. values of the central flowline are repeated
laterally. The central flowline is the same as the flowline of Parizek and others [2013] and
Chapter 5, which represents the central area of fastest flow. Lateral boundaries are provided
by the domain width ω in a symmetric way from the central flowline, e.g. a width of 50
(100) km considers 25 (50) km from each side of the central flowline. Surface and bedrock
elevations, basal shear stress, Glen's flow coefficient, basal melt and accumulation rates are

Table 6.1: *Source of model inputs for the flowline and 3D experiments*

Model input	Flowline Chapter 5	3D This chapter
Upper surface elevation z_s	Bamber and others [2009]	full-plane observations
Bedrock elevation b	Nitsche and others [2007] Le Brocq and others [2010] Tinto and Bell [2011]	full-plane observations
Grounded ice thickness $h(x < x_g)$	Holt and others [2006] Le Brocq and others [2010]	full-plane observations
Floating ice thickness $h(x > x_g)$	Bamber and others [2009] Griggs and Bamber [2009]	full-plane observations
Surface velocity v	Joughin and others [2009]	full-plane observations
Basal shear stress τ_b	Joughin and others [2009]	full-plane observations
Basal friction coefficient C	derived from v and τ_b	lateral extrusion
Basal friction exponent m	1/3	1/3
Temperature T	Pollard and DeConto [2012]	not used
Glen's flow coefficient A	derived from T	ice sheet: 5×10^{-25} Pa^{-3} s^{-1} ice shelf: 10^{-24} Pa^{-3} s^{-1}
Glen's flow exponent n	3	3
Basal melt rate $\dot{m}_b$	Pollard and DeConto [2012]	full-plane observations
Accumulation rate $\dot{a}$	Van de Berg and others [2006]	lateral extrusion
Grid size Δx	50 m	5 km

shown in plane view in Figure 6.1 and along the central flowline in Figure 6.2. A 3D view of the observed glacier geometry is depicted in Figure 6.3. Ice velocity was already shown in Chapter 5 (Figs. 5.1 and 5.2(a)) and is shown in plane view for the model domain in Figure 6.4.

6.2.2 Model

The model used in this study is the same as 'FM50' in Pattyn and others [2013] and is a 3D extension (i.e. including transverse direction) of the flowline SSA-FG model used in Chapters 3 to 5. This model shows reversibility of the grounding line according to the Schoof [2007a] setup for grid sizes $\Delta x \leq 500$ m [Pattyn and others, 2013]. We use finite-difference methods on a staggered grid to solve the shallow-shelf approximation (SSA) equations [MacAyeal, 1989].

Using deviatoric stresses τ_{ij} (equation (1.8)) in the component form of the momentum equation, where vertical shearing and vertical resistive stresses are neglected (equations (2.9), (2.10) and (2.11)), we derive

$$\frac{\partial}{\partial x}\left(2\tau_{xx} + \tau_{yy}\right) + \frac{\partial \tau_{xy}}{\partial y} = \rho_i g \frac{\partial z_s}{\partial x}, \tag{6.1}$$

$$\frac{\partial}{\partial y}\left(2\tau_{yy} + \tau_{xx}\right) + \frac{\partial \tau_{xy}}{\partial x} = \rho_i g \frac{\partial z_s}{\partial y}, \tag{6.2}$$

(a) Upper surface elevation

(b) Bedrock elevation

(c) Basal shear stress

(d) Basal melt rate
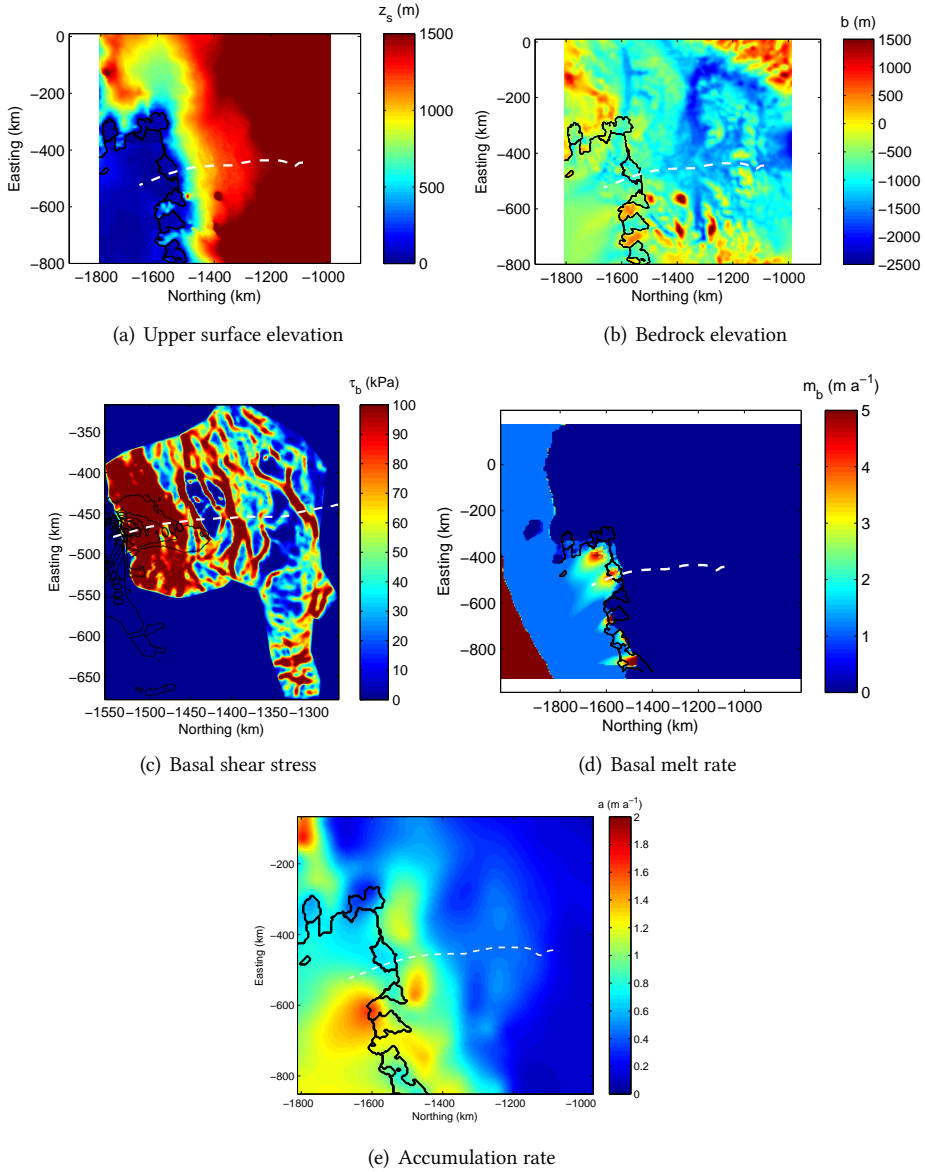
(e) Accumulation rate

Figure 6.1: *Model inputs (see Tab. 6.1 for source of data) for Amundsen Sea Sector with the central flowline of Thwaites Glacier used in this study (dashed white line) and the MOA grounding line (solid black line) [Scambos and others, 2007].*
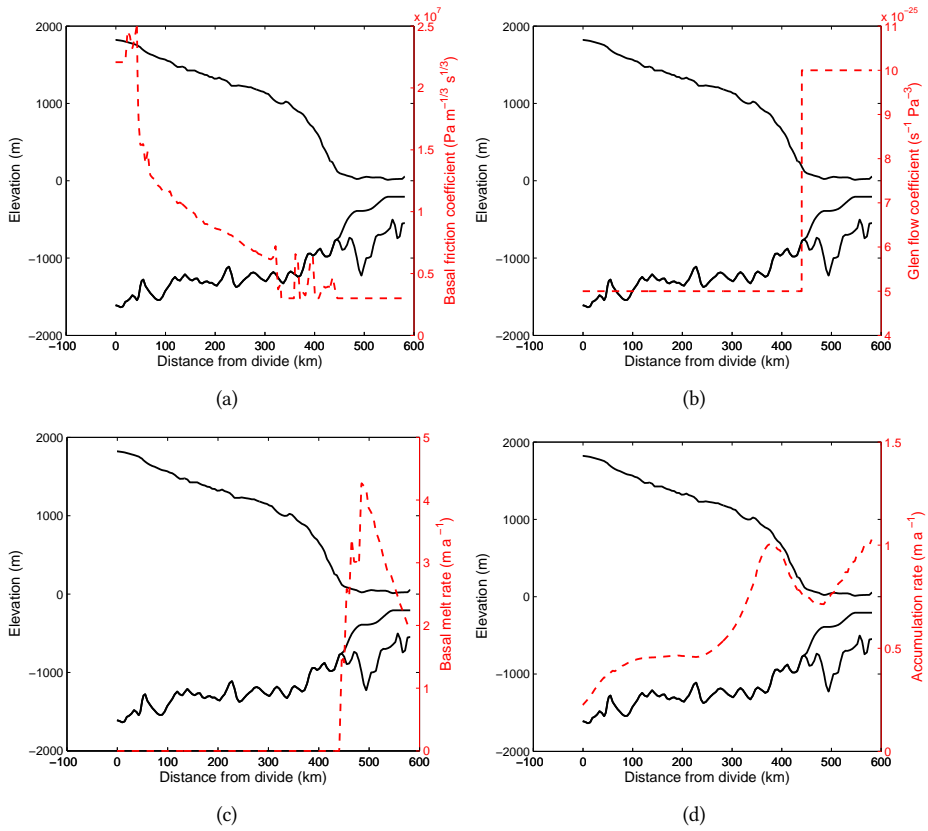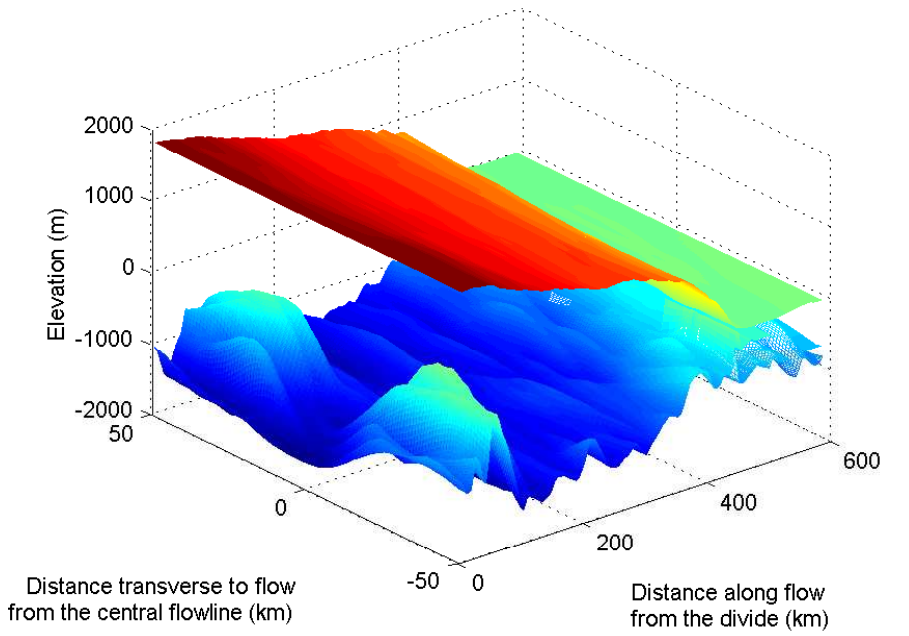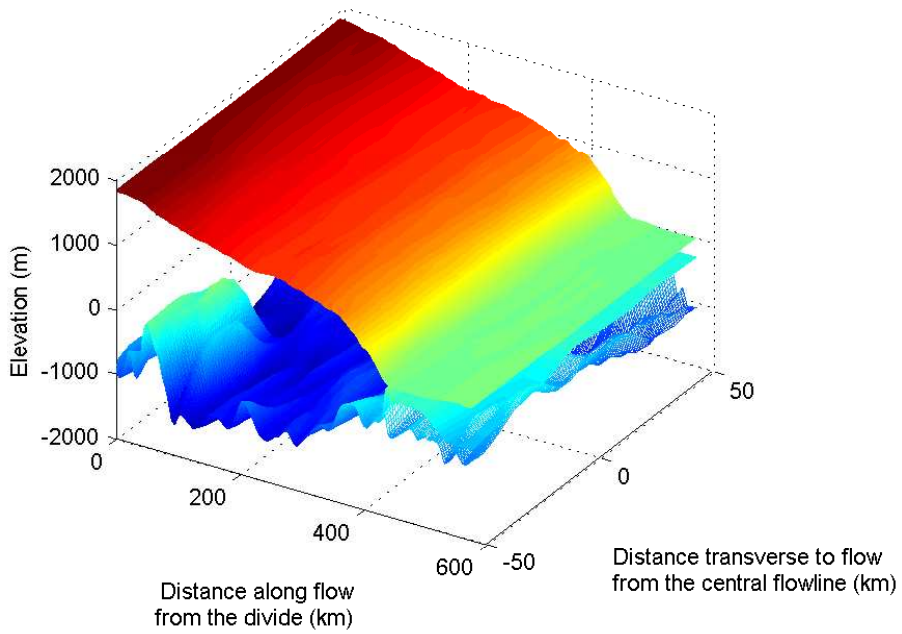
Figure 6.2: *Observed ice-sheet geometry and other model inputs (see Tab. 6.1 for source of data) along the central flowline of Thwaites Glacier.*

(a)

(b)

Figure 6.3: *Observed ice-sheet geometry of Thwaites Glacier with a width ω = 100 km from two different visual perspectives (Δx = 1 km).*
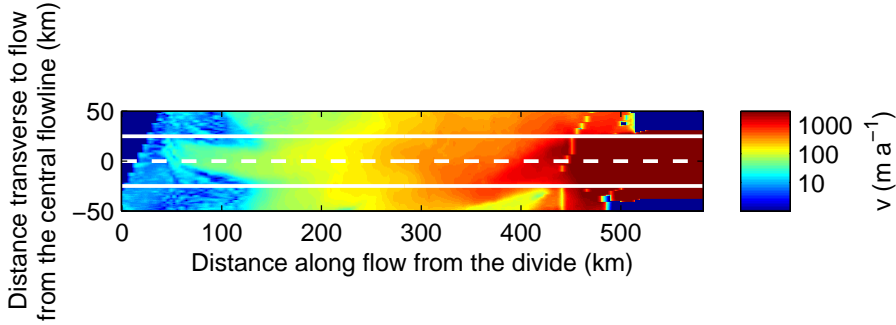
Figure 6.4: *Observed ice velocity v of the domain in plane view obtained by bi-linear interpolation of the data ($\Delta x = 1$ km). The central flowline is shown as a dashed white line. The domain lateral boundaries corresponding to widths $\omega = 50$ km and $\omega = 100$ km are shown as solid white lines and lateral borders of the figure respectively.*

where x and y are horizontal coordinates along flow and transverse to flow respectively, ρ_i is ice density, g is gravitational acceleration and z_s is surface elevation. Integrating (6.1) and (6.2) over the vertical, combining with Glen's flow law (1.9) and including the boundary condition at the ice bottom, we obtain the SSA equations [MacAyeal, 1989]:

$$\frac{\partial}{\partial x}\left[2\eta h\left(2\frac{\partial u}{\partial x}+\frac{\partial v}{\partial y}\right)\right] + \frac{\partial}{\partial y}\left[\eta h\left(\frac{\partial u}{\partial y}+\frac{\partial v}{\partial x}\right)\right] - \tau_{b,x} = \rho_i g h \frac{\partial z_s}{\partial x}, \qquad (6.3)$$

$$\frac{\partial}{\partial y}\left[2\eta h\left(2\frac{\partial v}{\partial y}+\frac{\partial u}{\partial x}\right)\right] + \frac{\partial}{\partial x}\left[\eta h\left(\frac{\partial u}{\partial y}+\frac{\partial v}{\partial x}\right)\right] - \tau_{b,y} = \rho_i g h \frac{\partial z_s}{\partial y}, \qquad (6.4)$$

where u and v are x- and y- components of ice velocity respectively and h is ice thickness. While the x- and y- components of basal shear stress are nonexistent in the ice shelf, they are given by:

$$\tau_{b,x} = C|u|^{m-1}u, \qquad (6.5)$$

$$\tau_{b,y} = C|v|^{m-1}v \qquad (6.6)$$

in the ice sheet, where C and m are basal friction coefficient and exponent respectively. The effective viscosity is computed as follows:

$$\eta = \frac{1}{2}A^{-\frac{1}{n}}\left[\left(\frac{\partial u}{\partial x}\right)^2 + \left(\frac{\partial v}{\partial y}\right)^2 + \frac{1}{4}\left(\frac{\partial u}{\partial y}+\frac{\partial v}{\partial x}\right)^2 + \frac{\partial u}{\partial x}\frac{\partial v}{\partial y}\right]^{\frac{1-n}{2n}}, \qquad (6.7)$$

where A and n are Glen's flow law coefficient and exponent respectively (vertical strain rate components are neglected).

The ice divide is a symmetry axis so the boundary conditions there are $u(0,y) = -u(\Delta x, y)$

and $v(0,y) = v(2\Delta x, y)$ for ice velocity and $h(0,y) = h(2\Delta x, y)$ for ice thickness. The boundary condition at the calving front reads:

$$2\eta \left[\left(2\frac{\partial u}{\partial x} + \frac{\partial v}{\partial y} \right) n_x + \frac{1}{2} \left(\frac{\partial u}{\partial y} + \frac{\partial v}{\partial x} \right) n_y \right] = n_x \frac{1}{2} \rho_i g h_c \left(1 - \frac{\rho_i}{\rho_w} \right), \tag{6.8}$$

$$2\eta \left[\left(2\frac{\partial v}{\partial y} + \frac{\partial u}{\partial x} \right) n_y + \frac{1}{2} \left(\frac{\partial u}{\partial y} + \frac{\partial v}{\partial x} \right) n_x \right] = n_y \frac{1}{2} \rho_i g h_c \left(1 - \frac{\rho_i}{\rho_w} \right) \tag{6.9}$$

for ice velocity, where $\mathbf{n} = (n_x, n_y)$ is the outward-pointing unit vector normal to the calving front, h_c is ice thickness at the calving front, ρ_w is water density. For ice thickness, the calving front boundary condition is $h(L, y) = h(L - \Delta x, y)$, where L is the domain length and Δx is the grid size in x.

Plane-strain (symmetric) boundary conditions apply at the domain lateral boundaries when we use full-plane observations: $u(x,0) = u(x, 2\Delta y)$, $u(x, \omega) = u(x, \omega - \Delta y)$, $v(x, 0) = -v(x, \Delta y)$, $v(x, \omega) = 0$, $\eta(x, 0) = \eta(x, 2\Delta y)$, $h(x, 0) = h(x, 2\Delta y)$, $h(x, \omega) = h(x, \omega - \Delta y)$, where ω is the domain width and Δy is the grid size in y.

In the case of laterally extruded geometries, periodic boundary conditions apply at the lateral boundaries of the domain: $u(x, 0) = u(x, \omega - \Delta y)$, $u(x, \omega) = u(x, \Delta y)$, $v(x, 0) = v(x, \omega - \Delta y)$, $v(x, \omega) = v(x, \Delta y)$, $\eta(x, 0) = \eta(x, \omega - \Delta y)$, $\eta(x, \omega) = \eta(x, \Delta y)$, $h(x, 0) = h(x, \omega - \Delta y)$, $h(x, \omega) = h(x, \Delta y)$.

The mass conservation equation (1.7) is integrated along the vertical to obtain the ice thickness evolution:

$$\frac{\partial h}{\partial t} + \nabla \cdot (\mathbf{v} h) = \dot{a} - \dot{m}_b, \tag{6.10}$$

where $\mathbf{v} = (u, v)$ is the horizontal ice velocity vector, $\dot{a}$ is accumulation rate and $\dot{m}_b$ is basal melt rate.

The grounding-line position for each y corresponds to the last grounded grid point, which is determined through the flotation criterion.

6.2.3   Experiments

Four experiments are performed to test the impact of TG geometry (bedrock and width) on grounding-line migration. As in Chapter 5, the model is initialized to the modern observed data described above and is then run to equilibrium with modern climate forcing. After sufficient years of integration, this yields an approximate match between observed and modeled geometry profiles on the one hand, and observed and modeled velocity profiles on the other. Like Exp. CW in Chapter 5, glacier width ω is constant in space and time, so that the effect of flow convergence is not taken into account and our domain looks like the one shown in Figure 5.3(a) (Chap. 5). Grid sizes of 0.25, 0.5 and 1 km are used in all experiments. We compare

these results with the flowline model of Chapter 5 using same model inputs along the flowline (with constant Glen's flow coefficient A, see Tab. 6.1) and grid sizes $\Delta x = 0.5$ and 0.05 km.

In the first experiment (Exp. 1), glacier width $\omega = 50$ km and bedrock elevation is obtained by bi-linear interpolation of the data for the whole domain (Fig. 6.5(a)). All other model inputs are similar to parameters in Table 6.1.

Lateral variations in bedrock elevation may cause the grounding line to stop or accelerate depending on the bedrock slope. Therefore, a second experiment (Exp. 2) is carried out with a laterally extruded geometry (bedrock (Fig. 6.5(b)), ice bottom and upper surface), as well as laterally extruded basal melt, i.e. there is no lateral variation. Other model inputs are similar to Exp. 1.

As shown by Durand and others [2011], the spatial resolution of bedrock elevation needs to be fine enough in coastal regions to capture grounding-line motion. To test this effect, we perform a third experiment (Exp. 3) where the bedrock is smoothed over 25 km (Fig. 6.5(c)). Smoothing is performed on the laterally extruded bedrock of Exp. 2 in these experiments. All other parameters are similar to Exp. 2.

A wider glacier domain ($\omega = 100$ km) is considered in a fourth experiment (Exp. 4) with the three different bedrock cases: bi-linear interpolation, lateral extrusion and smoothing.

6.3   Results

Figure 6.6 shows grounding-line evolution of Exps. 1−3 with different grid sizes, as well as the result of the flowline model. While no grounding-line retreat is observed when bi-linearly interpolating the bedrock (Exp. 1), the grounding line retreats by $\sim$ 180 km with laterally extruded bedrock (Exp. 2) and $\sim$ 270 km with lateral extrusion and bedrock smoothing over 25 km (Exp. 3) in 50 years. The flowline model behaves in the same way as laterally extruded experiments (Exps. 2 and 3) with a final grounding line between both experiments ($\sim$ 220 km). Recall that Exp. CW in Chapter 5 provides a grounding-line retreat of $\sim$ 150 km in 50 years but Glen's flow coefficient A varies in space in those flowline experiments. While a grid size of 1 km seems necessary to resolve grounding-line migration over 50 years for Exps. 1 and 3 (i.e. there is no significant difference between $\Delta x = 0.5$ km and $\Delta x = 1$ km), the coarsest grid size ($\Delta x = 1$ km) shows a stabilization of the grounding line on a bedrock bump after 35 years for Exp. 2. This is in agreement with the behavior of the flowline model (see also Chap. 5).

If Exp. 1 is run during 200 years, the grounding line retreats but only by $\sim$ 60 km (Fig. 6.7). We think that this retreat is much slower than with other bedrock configurations due to lateral variations in bedrock elevation that cause the grounding line to slow down. Figure 6.8 shows grounding-line positions in plane view for the three different kinds of bedrock treatments (bi-linear interpolation, lateral extrusion, smoothing): slower retreat observed with the bi-linearly

(a) Bi-linear interpolation

(b) Lateral extrusion of flowline
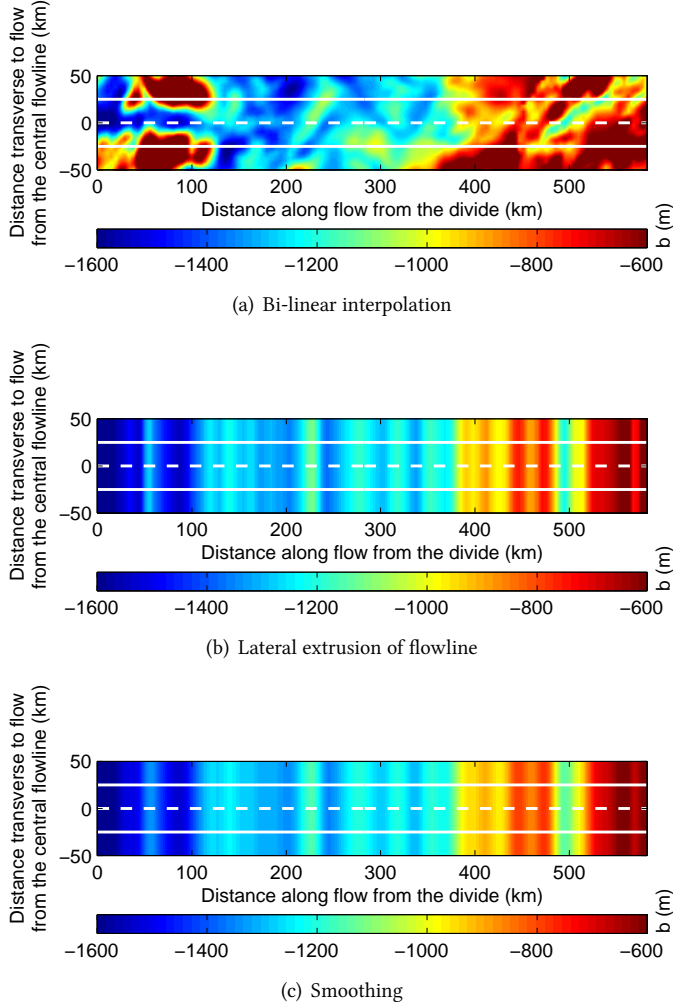
(c) Smoothing

Figure 6.5: *Bedrock elevation b of the domain in plane view obtained by (a) bi-linear interpolation of the data (Exp. 1), (b) lateral extrusion of central flowline data (Exp. 2), and (c) smoothing of bedrock elevation over 25 km (Exp. 3) ($\Delta x = 1$ km). The central flowline is shown as a dashed white line. The domain lateral boundaries corresponding to widths $\omega = 50$ km and $\omega = 100$ km are shown as solid white lines and lateral borders of the figure respectively.*
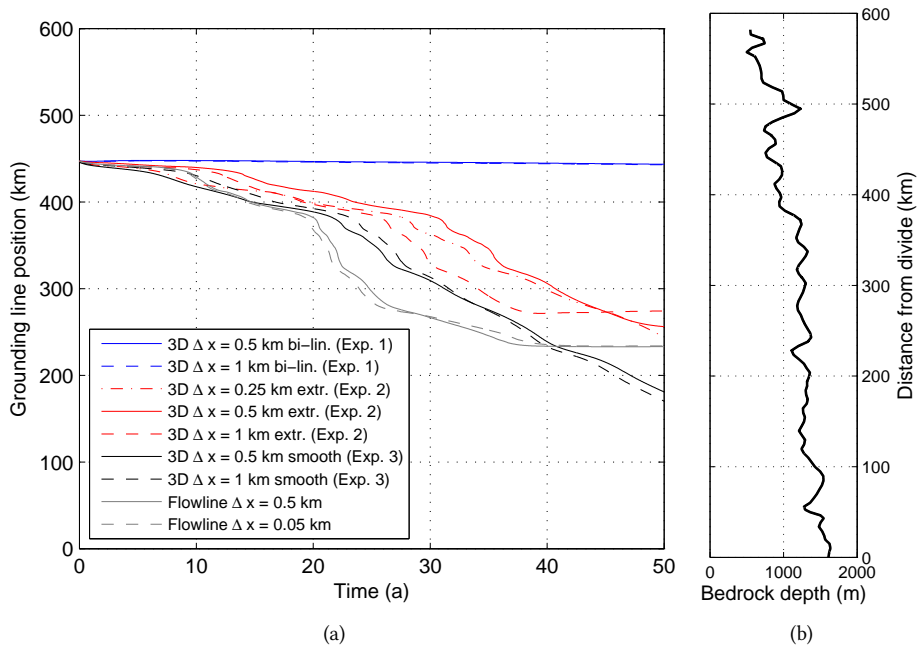
Figure 6.6: *(a) Thwaites central grounding-line position as a function of time (50 a) using the 3D model with different grid sizes (Δx = 0.25, 0.5 and 1 km) and three different geometry configurations ('bi-lin.' stands for 'bi-linear interpolation' and 'extr.' for 'lateral extrusion'). The 'central grounding-line position' is the position where the grounding line intersects the central flowline. Simulations with the flowline model are also shown (Δx = 0.5 and 0.05 km). (b) Bedrock depth.*

(a)   (b)
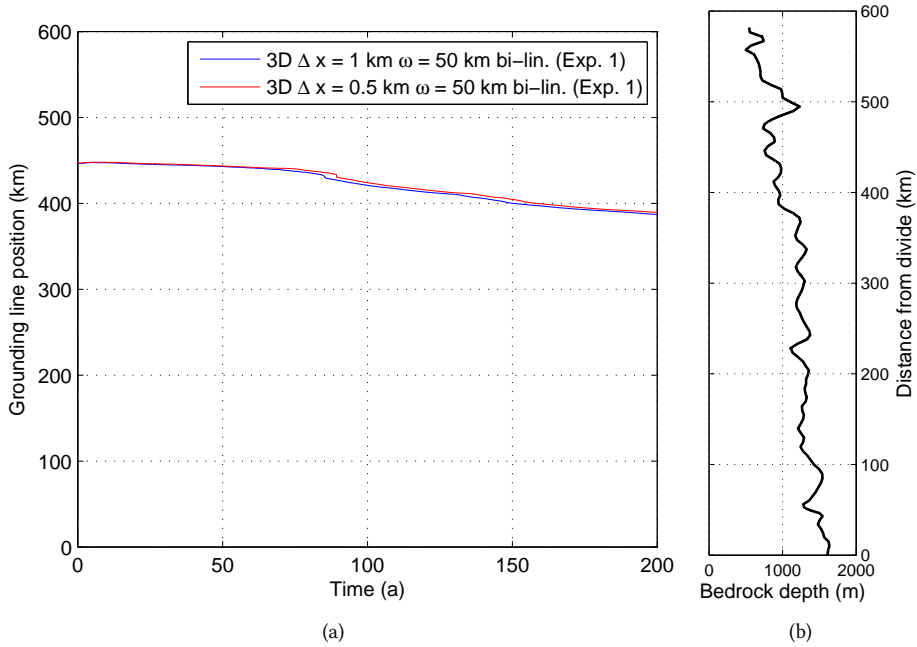
Figure 6.7: *(a) Thwaites central grounding-line position as a function of time (200 a) for Exp. 1 (bi-linear interpolation of data) with $\Delta x = 0.5$ and 1 km and $\omega = 50$ km. (b) Bedrock depth.*

interpolated bedrock may be due to the lateral variations in bedrock elevation, especially 50 km upstream the initial grounding line, involving grounding-line stabilization (Fig. 6.8(a)). The grounding lines of Exps. 2 and 3 are straight and retreat much more in a smaller time period (Figs. 6.8(b) and 6.8(c)). The use of a bedrock sampling distance of 25 km (Exp. 3) gives more retreat than other simulations, probably due to under-resolution of the bedrock bumps, allowing the grounding line to easily jump over them and enhancing the unstable nature of the bedrock (globally upward-sloping towards the ocean).

According to Schoof [2007a], a downward-sloping bedrock towards the ocean provides stable steady-state grounding-line positions, while a retrograde (i.e. upward-sloping) bedrock leads to instability. The focus here is on transient states (and not steady states) but it has been previously shown that negative bedrock slopes, and especially bedrock highs, slow down the grounding line in flowline mode while positive slopes accelerate it [Parizek and others, 2013; Docquier and others, submitted]. 3D modeling is more complex because lateral variations are present. However, we can clearly see that a non-negligible number of pixels are located in a 'stable' region (i.e. negative bedrock slope) in the beginning of Exp. 1 (Figs. 6.9(a) and 6.10(a)), whereas the initial grounding line of Exp. 2 is just at the boundary between stable and unstable regions (Figs. 6.9(b) and 6.10(b)) and Exp. 3 has an initial grounding line in an unstable region (Figs. 6.9(c) and 6.10(c)). We think that the more stable initial grounding-line

(a) Bi-linear interpolation (Exp. 1)

(b) Lateral extrusion (Exp. 2)
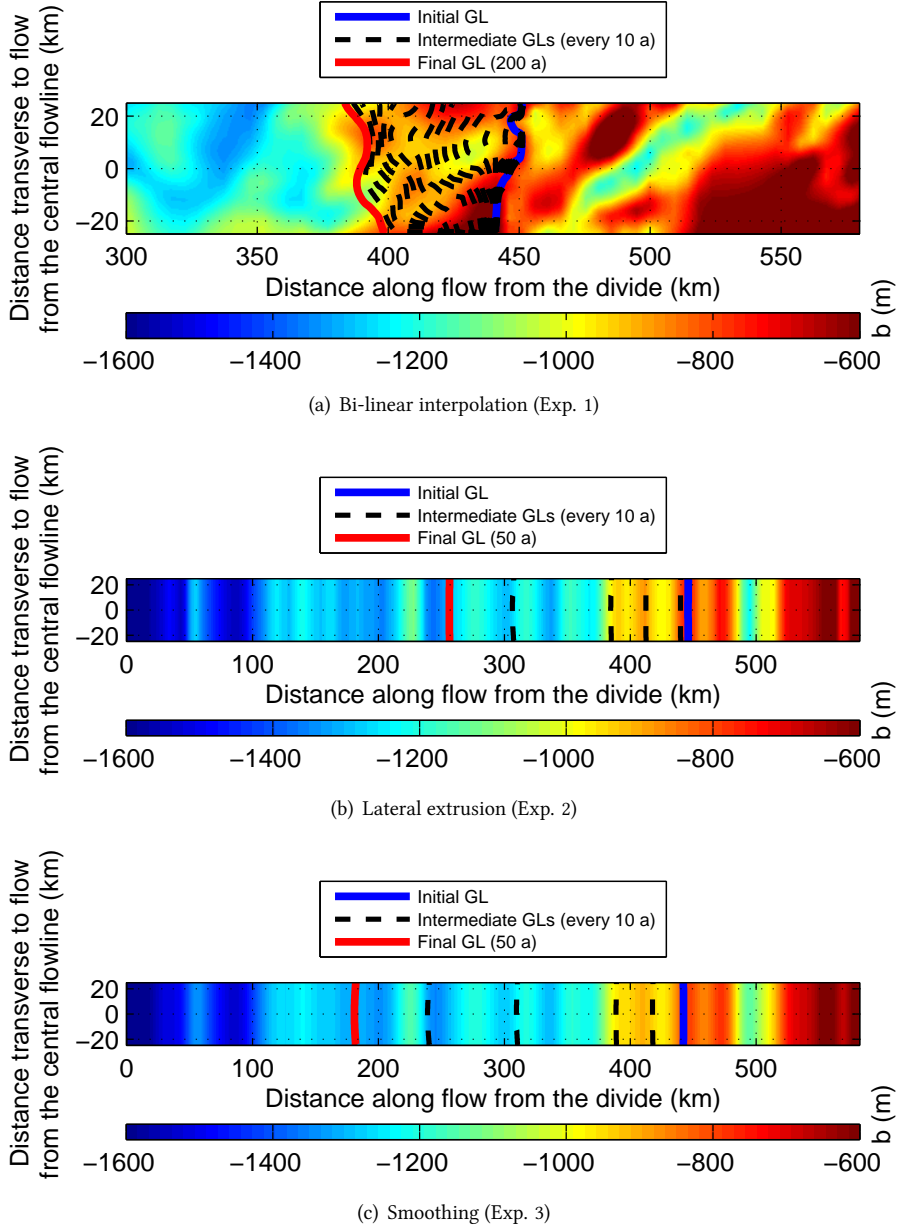

(c) Smoothing (Exp. 3)

Figure 6.8: *Grounding-line (GL) positions in plane view plotted every 10 year with the corresponding bedrock elevation b for three simulations: (a) bi-linear interpolation of the data (Exp. 1), (b) lateral extrusion of central flowline data (Exp. 2), and (c) smoothing of bedrock elevation over 25 km (Exp. 3) (Δx = 0.5 km).*

position of Exp. 1 is linked to its slow retreat.

The grounding-line ice flux is much higher for Exps. 2 and 3 relative to Exp. 1 (Fig. 6.11), leading to high grounding-line retreats for those two experiments. The pattern of Exp. 1 is especially interesting because lateral variations in grounding-line flux correlate with grounding-line position: after 70 years, the higher flux around $y = 5$ km (Fig. 6.11(a)) leads to a grounding line further upstream in this region (Figs. 6.9(a) and 6.10(a)). This higher flux is caused by a higher grounding-line thickness (Fig. 6.12). The high grounding-line flux in the very beginning of the simulation (Fig. 6.11(a)) is linked to high velocity at the grounding line.

The wider domain considered in Exp. 4 (glacier width $\omega = 100$ km) gives approximately the same grounding-line retreat for the three bedrock configurations when compared to a width $\omega = 50$ km (compare Figs. 6.13 and 6.6).

6.4   Conclusions

Three different kinds of bedrock configurations with a constant glacier width of 50 km were used to feed a 3D SSA model applied to Thwaites Glacier (from the ice divide to the calving front). Bi-linearly interpolating full-plane observations (first bed configuration) shows no grounding-line retreat in 50 years and ~ 60 km in 200 years (mean rate of 0.3 km a^{-1}). Much faster retreats of the glacier inland result from laterally extruding the bedrock (second bed configuration; mean rate of ~ 3.6 km a^{-1}) and smoothing the bedrock over 25 km (third bed configuration; mean rate of ~ 5.4 km a^{-1}), resembling the result obtained with the flowline model.

Lateral variations in bedrock elevation cause the grounding line not to retreat as fast as with lateral extrusion of the central flowline. Downward-sloping bedrock towards the ocean and lower ice thickness provide lower grounding-line ice flux and slow down the grounding line. Smoothing the bedrock over a certain distance enhances the unstable nature of the bedrock, providing faster retreat. Therefore, an accurate description of the bedrock topography, especially in the vicinity of the grounding line, is of major importance to understand future glacier behavior. Finally, no significant difference is found when the width is doubled (100 km).

6.5   Outlook

A number of further tests could be made with this model on TG. We detail them below.

1. As long as these 'projections' do not use future emission scenarios (e.g. IPCC), through atmospheric coupling, no robust glacier projection can be done. In addition, we would need to couple the ice-sheet model to an ocean model to correctly simulate sub-ice shelf melt [Goldberg and others, 2012].

(a) Bi-linear interpolation (Exp. 1)

(b) Lateral extrusion (Exp. 2)
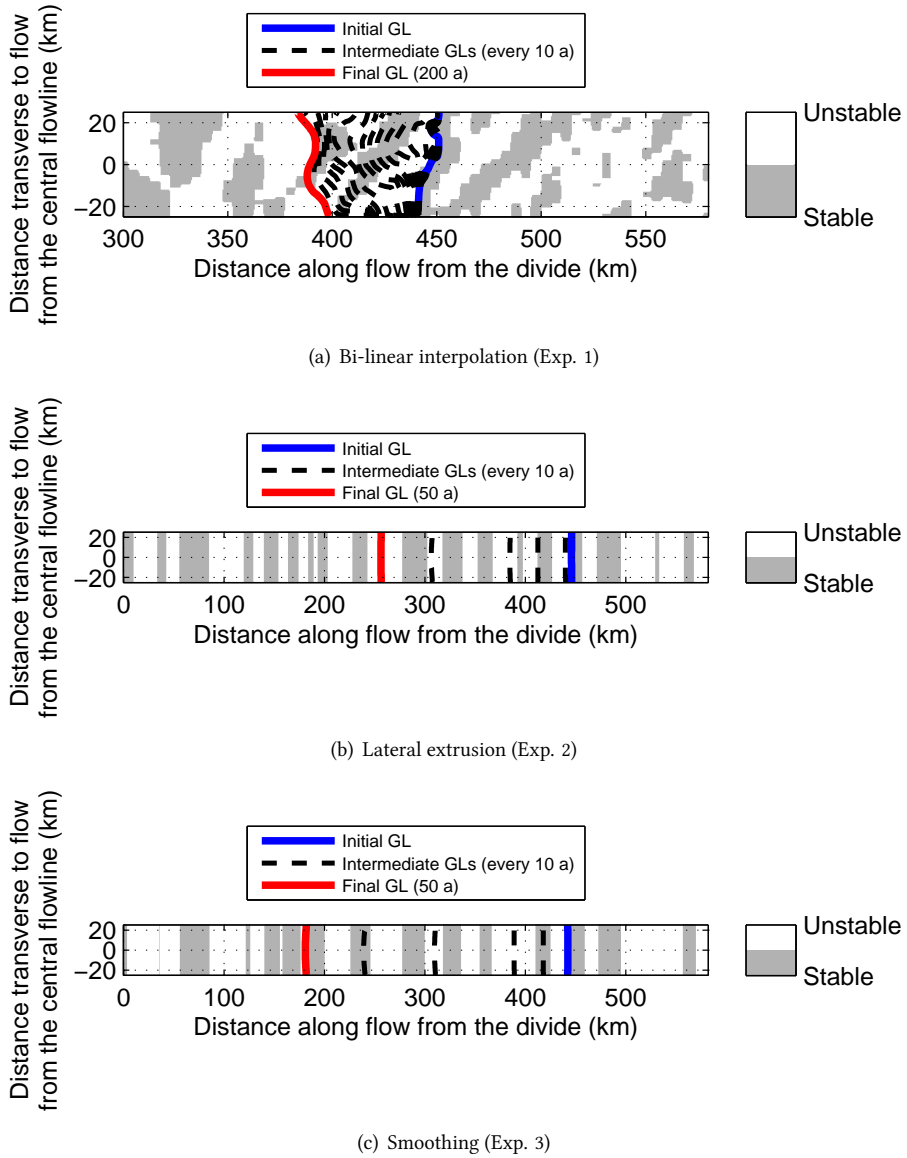
(c) Smoothing (Exp. 3)

Figure 6.9: *Grounding-line (GL) positions in plane view plotted every 10 year with the corresponding 'stability' for three simulations: (a) bi-linear interpolation of the data (Exp. 1), (b) lateral extrusion of central flowline data (Exp. 2), and (c) smoothing of bedrock elevation over 25 km (Exp. 3) (Δx = 0.5 km). Grounding-line stability is based on bedrock slope: a positive/negative bedrock slope (towards the ocean) provides unstable/stable position respectively.*

(a) Bi-linear interpolation (Exp. 1)   (b) Lateral extrusion (Exp. 2)   (c) Smoothing (Exp. 3)

Figure 6.10: *Same as Figure 6.9 with a zoom close to the initial grounding line.*

2. Glen's flow coefficient A depends on ice temperature. However, the 3D model used here becomes unstable when using provided spat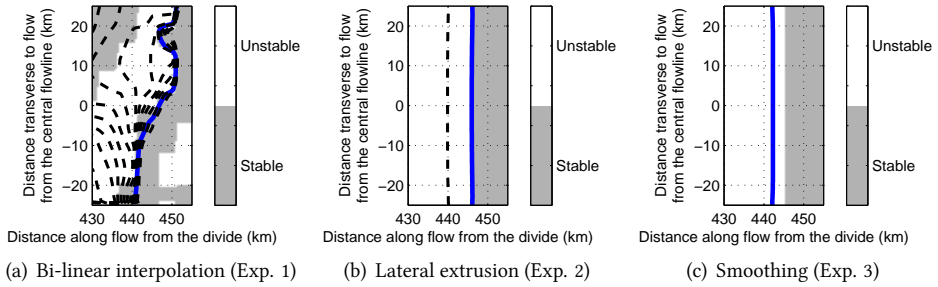ially-variable A values, so that we use a constant value in the ice sheet and a different constant value in the ice shelf. The sensitivity to spatially-variable A could be tested by slightly changing the provided values and trying to find a 'stable' simulation.

3. In this study, basal friction coefficient C is laterally extruded due to model instability when running with full-plane observations. This is probably due either to the fact that basal shear stress τ_b comes from a model inversion [Joughin and others, 2009], which is not the model we use here, or because C varies too much in the lateral direction. Furthermore, C depends on both basal shear stress τ_b and ice velocity v but these parameters are not known with certainty, especially τ_b that comes from an inversion [Joughin and others, 2009]. Thus, a sensitivity to C could be performed.

4. The reason why the 3D extruded case (Exp. 2) does not provide exactly the same retreat as the flowline model is not clear but could be due to the fact that the lateral boundary conditions of the 3D model may play a role. This is to further explore.

5. Finally, experiments in this study use a constant glacier width, like Exp. CW in Chapter 5. However, in the real world, the glacier widens inland, so that there is an effect of flow convergence and divergence. Improvement of the model could be made by taking the whole drainage basin as a model domain instead of a constant width. This would permit a comparison between these 3D results and the flowline results of Exps. VW and CSW (Chap. 5). The strategy for this test could be implemented in two steps and is detailed below. Figure 6.14 illustrates the principle.

The first step consists in determining the drainage basin of TG. This can be done by locating where both ice surface elevation slope dz_s/dy in the direction transverse to flow and ice velocity vector v are approximately zero. This provides the limits of the drainage basin, i.e. boundaries with Pine Island Glacier in the east and Smith Glacier in
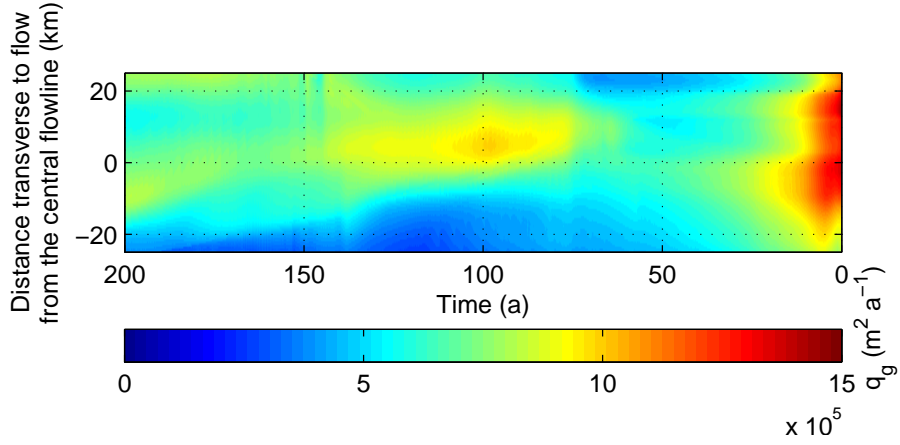
(a) Bi-linear interpolation (Exp. 1)
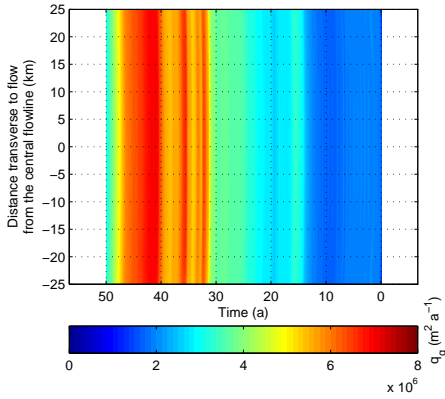
(b) Lateral extrusion (Exp. 2)
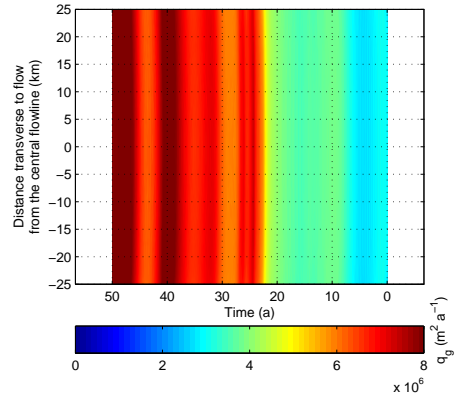
(c) Smoothing (Exp. 3)

Figure 6.11: *Modeled grounding-line ice flux q_g in plane view as a function of time for three simulations: (a) bi-linear interpolation of the data (Exp. 1), (b) lateral extrusion of central flowline data (Exp. 2), and (c) smoothing of bedrock elevation over 25 km (Exp. 3) ($\Delta x = 0.5$ km). The beginning of the simulation corresponds to time $= 0$ (right).*

Figure 6.12: *Modeled grounding-line ice thickness h_g in plane view as a function of time for the simulation using bi-linear interpolation of the data (Exp. 1) ($\Delta x = 0.5$ km). The beginning of the simulation corresponds to time = 0 (right).*
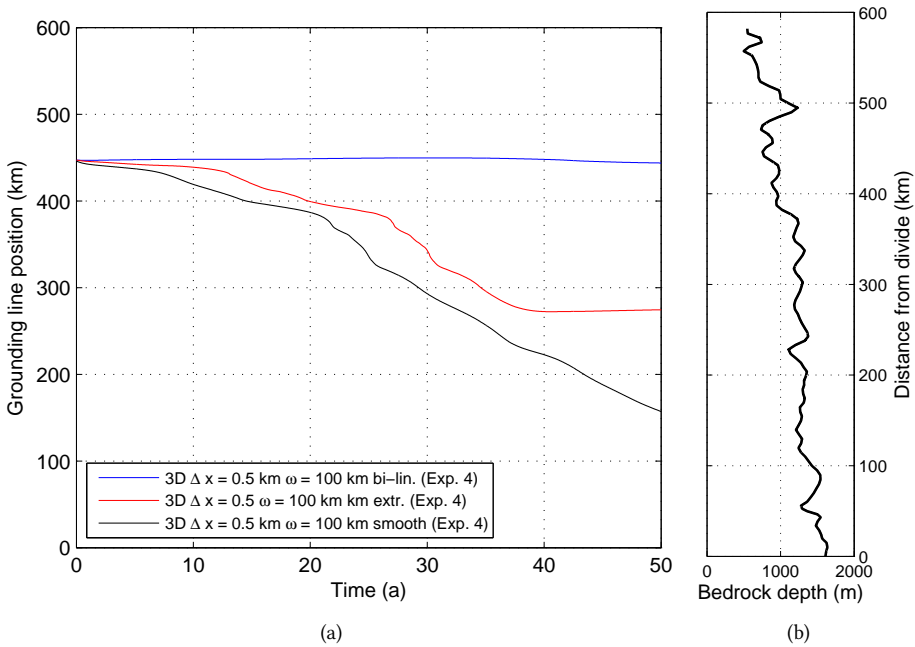
Figure 6.13: *(a) Thwaites central grounding-line position as a function of time (50 a) with $\Delta x = 0.5$ km and $\omega = 100$ km. (b) Bedrock depth.*
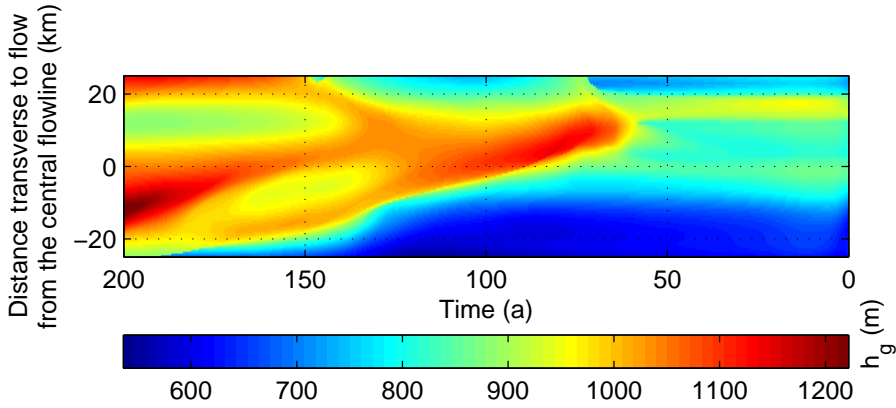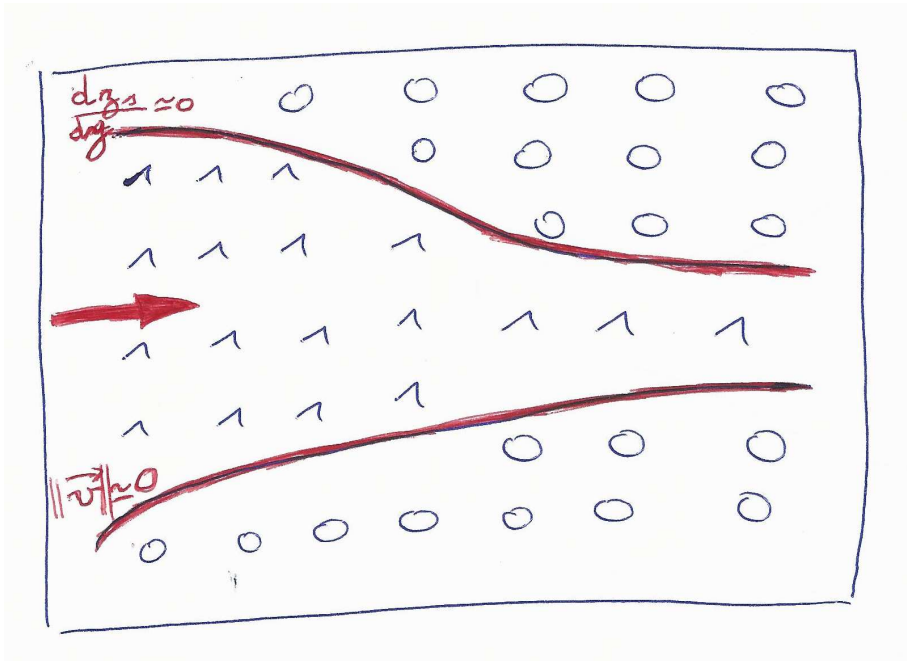
Figure 6.14: *Schematic plane-view representation of the method used to incorporate Thwaites Glacier drainage basin into the model. The limits of the drainage basin (in red) are defined by surface elevation slope $dz_s/dy \approx 0$ and ice velocity vector $v \approx 0$. A value of 1 is assigned to pixels within the drainage basin and a value of 0 outside the basin. The ice flow direction is represented by the red arrow.*

the west. An approximate location of this basin can be seen in Figure 1 of Joughin and others [2009].

The second step is the model implementation. Since our model is designed in such a way that the domain must be rectangular, one could take a domain that encompasses the whole drainage basin and build a mask for making the calculations only inside the basin (Pattyn, Personal Communication, 2013), i.e. assigning values of 1 for pixels falling into the basin and 0 for pixels out of the basin. A velocity of 0 could be given as lateral boundary condition.

Ideally, this implementation should be performed with the new Bedmap2 data [Fretwell and others, 2013], incorporating the Tinto and Bell [2011] bathymetry, to test the influence of the bedrock ridge on the eastern ice shelf.

Conclusions and Perspectives

7.1 Conclusions

Media have widely reported Greenland and Antarctic ice-sheet losses and corresponding sea-level rise in recent years but reasons for these rapid changes have not always been clear. It is rather complex to identify the exact causes since we lack data about conditions within ice sheets, and models need more development before realistically simulating recent changes. That is why research is divided into several groups that study very specific glaciological processes and interact with each other in order to resolve the unknowns.

This thesis focuses on a very specific glaciological process, i.e. grounding-line migration, that is key to understand how the West Antarctic ice sheet behaves. The dynamics of the grounding line strongly controls the stability of a marine ice sheet [Weertman, 1974; Schoof, 2007a] and thus, indirectly, the land-ice contribution to sea-level rise, one of the most important concerns of scientists today [Solomon and others, 2007; ice2sea, 2013; Bindschadler and others, 2013]. Rapid inland retreat and flow acceleration of the glaciers in the Amundsen Sea Embayment (ASE) have been observed over the last decades [Rignot and others, 2008; Scott and others, 2009; Wingham and others, 2009; Jenkins and others, 2010; Tinto and Bell, 2011]. Those are caused by warm ocean currents that come underneath the ice shelves and thin their base, provoking a loss of buttressing [Pritchard and others, 2012; Steig and others, 2012].

Chapter 2 clearly demonstrates the dependence of grounding-line migration modeling on both the numerical approach and the physical approximation of the model used. We use three kinds of finite-difference flowline models, two using the Shallow-Ice Approximation (SIA) in the ice sheet and the Shallow-Shelf Approximation (SSA) in the shelf and one using the SSA in the whole domain with basal sliding in the ice sheet. The two hybrid SIA/SSA models differ by the type of grid, i.e. staggered or non-staggered (collocated) grid. All three models include the Schoof [2007a] boundary condition at the grounding line via the Pollard and DeConto [2009] heuristic rule. In theory, starting from an ice sheet with a certain initial grounding-line position, increasing the ice-sheet viscosity to achieve a grounding-line advance and resetting it to its initial value on a downward-sloping bedrock (towards the ocean) should give a final steady-state grounding-line position equal to the initial position [Schoof, 2007a]. However, a difference between final and initial grounding-line positions exists and depends on the type

of model used, as later demonstrated by the Marine Ice Sheet Model Intercomparison Project (MISMIP, Pattyn and others [2012]) and its corresponding three-dimensional (3D) version (MISMIP3D, Pattyn and others [2013]).

In Chapter 2, we also show that staggered-grid models (SIA/SSA and SSA) forced with the Schoof [2007a] boundary condition converge to the same steady-state grounding-line position irrespective of the grid size used. On the contrary, models that are either non-staggered or do not include the Schoof [2007a] boundary condition converge only to the same advance-retreat position for sufficiently small grid sizes, confirming results of Vieli and Payne [2005] and Durand and others [2009b] for fixed-grid models. The transient behavior of those models is influenced by the parameterization scheme of grounding-line migration, leading to sudden changes in grounding-line ice flux whenever a jump from one grid point to another occurs due to the heuristic rule.

In Chapter 3, we execute short-term perturbations (200 years) of a steady-state ice sheet by decreasing the buttressing effect provided by the ice shelf on the inland grounded ice, leading to grounding-line retreat. Four different flowline models that differ by the physics (SSA or full-Stokes), numerics (finite difference, finite element or pseudo-spectral), grid type (fixed, moving or adaptive) and grounding-line treatment (flotation, heuristic rule, contact problem or margin tracking) implemented are compared. The model results are broadly consistent between each other in terms of grounding-line migration and evolution of surface geometry.

However, some differences remain. The model that implements the Schoof [2007a] boundary condition exhibits faster grounding-line retreat and larger surface thinning, which leads to an overestimated grounding-line discharge. The signal of this model over decadal time scales is also altered by high frequency, large amplitude numerical noise, due partly to the coarse grid size and partly to the heuristic rule. Therefore, models that prescribe the flux at the grounding line should be used with particular attention to analyze transient behavior. The full-Stokes model also shows a discontinuous grounding-line retreat due to the grid size, but with a lower amplitude than the model that prescribes the grounding-line flux. The moving grid model used in this study explicitly calculates grounding-line migration (and not grounding-line position), ensuring a smoother behavior compared to the other models.

Using the same four flowline models, we show in Chapter 4 that a same initial setup can give different steady-state ice-sheet profiles depending on the model used. The full-Stokes model has a grounding line further upstream, probably due to the inclusion of vertical shear stress, reducing the effective viscosity and speeding up ice flow. This important result, first shown with these experiments, has been confirmed in the framework of MISMIP3D. In terms of grounding-line position, thickness and flux, the overall model response to sea-level perturbations is similar. Like in Chapter 3, the oscillating behaviors of the model prescribing the flux at the grounding line and the full-Stokes model are still observed. Finally, the grounding-line evolution of the model using the heuristic rule is improved by linearly interpolating ice flux.

In Chapter 5, we apply a flowline ice stream-ice shelf SSA model to Thwaites Glacier (TG),

which is located in ASE and is one of the fastest-flowing outlet glaciers of West Antarctica with Pine Island Glacier. By feeding the model with available data for the geometry, basal shear stress, ice temperature, basal melt rate and accumulation rate, an approximate match between modeled and observed velocities is performed after less than 10 years, with thinning rates comparable to the observed ones. After this relaxation phase, the grounding line retreats with a mean rate of 1.5 km a^{-1}, i.e. 300 km in 200 years. The effect of flow convergence is tested by parameterizing the glacier width in the continuity equation: this generally slows down the retreat. Furthermore, a convergence in the ice shelf decreases the ice flux and tends to stabilize the grounding line.

The parameterization of ice-shelf buttressing according to different observed scenarios further reduces the glacier retreat and can even lead to a slight advance in the most buttressed case. A contact between the ice shelf and a pinning point is made in most experiments, leading to lower discharge. We also use the new Bedmap2 [Fretwell and others, 2013] dataset and show that the grounding line does not retreat much due to an initial position further downstream on the downward-sloping bedrock (towards the ocean). However, Bedmap2 does not include the Tinto and Bell [2011] bathymetry.

The experiments performed in Chapter 5 are extended to the 3D case in Chapter 6 using a constant glacier width. Lateral boundaries are parallel to the central flowline[1]. The grounding line retreats by about the same distance as the grounding line modeled by the flowline model (i.e. $\sim$ 200 km in 50 years) if the bedrock is laterally extruded from the central flowline, with faster retreat when smoothing the bedrock elevation over 25 km (mean rate of $\sim$ 5.4 km a^{-1}). If full-plane observations are bi-linearly interpolated onto our model grid, the grounding line does not retreat in 50 years and only retreats by $\sim$ 60 km in 200 years. This is caused by lateral variations in bedrock topography, with downward-sloping bedrock that slows the grounding-line retreat and lowers the ice flux.

However, a number of limitations exist about the models used, the data and the user himself in this thesis. Concerning the model limitations:

- Even if we compare the results of this study with a full-Stokes model (Elmer/Ice), we mainly use SSA models due to their fast computation time and their applicability to fast-flowing glaciers (see Section 5.2.2), but those models may lack some processes, e.g. vertical shearing.

- The models used in this thesis solve the Stokes equations with finite differences, although comparisons are performed with other numerical approaches (finite element and pseudo-spectral). The finite-difference scheme used here is the FTCS (forward in time, central in space), which is only first-order accurate in time, whereas the CTCS (central in time and space) scheme is second-order accurate in both time and space. However,

---

[1]The central flowline corresponds to the flowline in Chapter 5.

the CTCS is unconditionally unstable, i.e. spontaneous perturbations in the solutions of the equations do not necessarily decay as the computations proceed [Primer, 2011].

- Most simulations of this study are performed along a flowline (only Chap. 6 uses a 3D model), lacking 3D effects even if they can be parameterized (e.g. buttressing and flow convergence). These parameterizations may not adequately represent the 'real world'.

- The heuristic rule of Pollard and DeConto [2009], implemented in one of the models (SSA-H-FG), performs well in steady-state simulations but is less accurate in terms of short-term experiments. Thus, predicting future behavior of Antarctica, or some parts of it, with this kind of model should be done very carefully.

- In the 3D simulations (Chap. 6), glacier width is constant in space and the validity of lateral boundary conditions is questionable, as mentioned in Section 6.5.

- Other effects are not taken into account in the models, e.g. iceberg calving, atmospheric and oceanic coupling, sedimentation effect.

- Thermomechanical coupling is also not taken into account.

- The subglacial system underneath TG seems to play a key role in glacier stability and grounding-line retreat, with a distributed water system upstream lubricating the ice above and concentrated canals downstream causing the ice base to stick [Schroeder and others, 2013]. However, current models predicting glacier behavior do not yet account for these subglacial processes.

Four kinds of limitations are inherent to the data used in Chapters 5 and 6 for TG:

- An error is linked to both measurements of ice-sheet geometry and ice velocity, and data originating from other models, i.e. basal shear stress, ice temperature, basal melt rate and accumulation rate.

- There is a mismatch in data acquisition time, e.g. between surface geometry (2003-2008) and ice velocity (1996), but this numerically stabilizes the modern TG according to Parizek and others [2013].

- Data spatial resolution may also be another source of error, especially close to the grounding line. Bedrock resolution needs to be sufficiently low to capture grounding-line motion accurately, as suggested by Durand and others [2011] and our bedrock smoothing in Chapter 6. In Chapters 5 and 6, we use an improved version of ALBMAP data instead of Bedmap2 because the former dataset includes the Tinto and Bell [2011] bathymetry, which is crucial for TG. However, ALBMAP is compiled via 5 km and re-sampled to 1 km, whereas Bedmap2 is directly interpolated from the original data to a 1 km grid.

- Interpolation of model inputs onto our model grid can also produce small artifacts. The approach of linear interpolation is used in Chapters 5 and 6.

Other limitations are linked to the user, i.e. a lack of experience in certain fields (e.g. data acquisition) and possible computing errors (e.g. in the model codes).

7.2 Perspectives

In response to the limitations presented above, some improvements could be made:

- Compare the results obtained for TG (Chaps. 5 and 6) with other models, e.g. Elmer/Ice (finite-element full-Stokes model) [Favier and others, 2012] or BISICLES (finite-volume higher-order model) [Cornford and others, 2013], as already carried out for Pine Island Glacier [Favier and others, submitted].

- For the 3D simulations (Chap. 6), take into account the whole drainage basin of TG (see Section 6.5) and use lateral boundary conditions that involve a prescribed amount of lateral drag obtained from observed velocity gradients at the sides.

- For the 3D simulations (Chap. 6), test the sensitivity of grounding-line migration on both Glen's flow and basal friction coefficients.

- Include iceberg calving [Nick and others, 2009; Bassis, 2011; Nick and others, 2013], atmospheric and oceanic coupling, sedimentation effect [Alley and others, 2007], subglacial processes [Schroeder and others, 2013], thermomechanical coupling [Pattyn, 2003], etc. in the models. For example, oceanic coupling would permit us to better understand how the ocean interacts with the ice shelf base and what is the effect of basal melting on grounding-line migration [Goldberg and others, 2012].

- Acquire higher bedrock spatial resolution close to the grounding line of TG and use Bedmap2 data with the Tinto and Bell [2011] bathymetry.

- Test other methods to interpolate data onto our model grid (e.g. nearest neighbor, spline, cubic).

Concerning TG bedrock spatial resolution, we have answered the Bedgap questionnaire proposed by H. Pritchard concerning priorities for improving the mapping of subglacial/submarine topography of Bedmap2 [Fretwell and others, 2013]. Below are the questions of Pritchard as well as our answers.

```
From: david.docquier@ulb.ac.be
Subject: Bedgap Questionnaire
```

To: hprit@bas.ac.uk
Date: 30/07/2013 17:54

Dear Hamish,

These are my answers to your Bedgap questionnaire.

1) In terms of bed topography, what sampling does your work require?
i.e., how detailed does the topographic grid need to be to capture
the features important to your research? Please give a value in km
(e.g. 0.1 km, 2 km, 10 km...).

Less than 0.5 km in the vicinity of the grounding line (recommended
by MISMIP3D) and coarser grid size away from the grounding line.
Ideally, it would be good to have a spatial resolution of 0.25 km
in a zone starting about 100 km upstream the grounding line (Thwaites
Glacier is expected to retreat in the coming decades) and ending
about 20 km downstream the grounding line. Having a resolution of
1 km away from this zone would be enough (so using Bedmap2 is fine).

2) Approximately what size of area would you need these data over?
This doesn't need to be an exact measure, it could be a rough box
e.g. 20x20 km, 100x100 km, or 500x1000 km.

A zone of approx. 120 km long (100 km upstream the GL + 20 km
downstream) and 100 km wide (along Thwaites Glacier Tongue and eastern
ice shelf grounding line), where the grid size is lower than 0.5 km.

3) Where would you put this survey? To answer this, you can either
centre it on a latitude/longitude coordinate or define it by a
recognised geographical name so I could work out where to put it on a
map.

Lower Thwaites Glacier (including Thwaites Glacier Tongue and eastern
ice shelf).

4) What is the theme of your research? e.g. ice stream dynamics,
oceanography, subglacial hydrology, geomorphology, ice cores,
tectonics, biodiversity

Ice stream dynamics (grounding-line dynamics) using flowline and 3D

```
marine ice-sheet models.
```

```
Best regards,
David
```

In conclusion, evidence of recent warming has been shown in a large number of different studies and will be confirmed in the next IPCC report (AR5). One of the major consequences is the melting of ice sheets and glaciers, involving sea-level rise. Meehl and others [2012] show that with an aggressive mitigation scenario[2], global average temperature increase could be stabilized below 2 °C above pre-industrial values. However, sea level would continue to rise due to the system inertia.

Therefore, in order to apply the best adaptation and mitigation procedures, it is crucial to keep improving our understanding of the physical processes that govern our planet, especially how the huge Antarctic ice sheet will react in such a warming world. Longer observational records, including observations at the ice-ocean interface, and more robust model projections would improve this understanding. According to Wayman [2013], 'although the ramp-up in research has not yet provided a detailed climate forecast for Antarctica, recent studies reveal that the remote landmass is not as isolated as once thought. Its fate is linked with every corner on Earth.'

---

[2]This aggressive scenario corresponds to RCP2.6 and specifies that, from 2070, more carbon dioxide is removed from the atmosphere than it is emitted. A strategy that could lead to this goal would be to have $\sim$ 20 % fossil fuel without carbon capture and storage (CCS), $\sim$ 45 % fossil fuel with CCS, and $\sim$ 35 % renewable and nuclear energies for the primary energy sources in 2070 [Meehl and others, 2012].

Figure 7.1: *International summer school in glaciology (Kennicott Glacier, Alaska, June 2010).*

Bibliography

Alley, R. B., S. Anandakrishnan, T. K. Dupont, B. R. Parizek and D. Pollard, 2007. Effect of sedimentation on ice-sheet grounding-line stability, *Science*, **315**, 1838–1841.

Bamber, J. L., J. L. Gomez-Dans and J. A. Griggs, 2009. A new 1 km digital elevation model of the Antarctic derived from combined satellite radar and laser data – Part 1: Data and methods, *The Cryosphere*, **3**(1), 101–111.

Baral, D. R., K. Hutter and R. Greve, 2001. Asymptotic theories of large-scale motion, temperature, and moisture distribution in land-based polythermal ice sheets: a critical review and new developments, *Appl. Mech. Rev.*, **54**(3), 215–256.

Bassis, J. N., 2011. The statistical physics of iceberg calving and the emergence of universal calving laws, *J. Glaciol.*, **57**(201), 3–16.

Bindoff, N. L., J. Willebrand, V. Artale, A. Cazenave, J. Gregory, S. Gulev, K. Hanawa, C. Le Quéré, S. Levitus, Y. Nojiri, L.D. C.K. Shum, Talley and A. Unnikrishnan, 2007. Observations: Oceanic Climate Change and Sea Level. In: *Climate Change 2007: The Physical Science Basis. Contribution of Working Group I to the Fourth Assessment Report of the Intergovernmental Panel on Climate Change* [Solomon, S., D. Qin, M. Manning, Z. Chen, M. Marquis, K.B. Averyt, M. Tignor and H.L. Miller (eds.)], Cambridge University Press, Cambridge, United Kingdom and New York, NY, USA.

Bindschadler and others, 2013. Ice-sheet model sensitivities to environmental forcing and their use in projecting future sea level (the SeaRISE Project), *J. Glaciol.*, **59**(214), 195–224.

Blatter, H., 1995. Velocity and Stress Fields in Grounded Glaciers: a Simple Algorithm for Including Deviatoric Stress Gradients, *J. Glaciol.*, **41**(138), 333–344.

Cazenave, A. and W. Llovel, 2010. Contemporary Sea Level Rise, *Annu. Rev. Mar. Sci.*, **2**, 145–173.

Chen, J. L., C. R. Wilson, D. Blankenship and B. D. Tapley, 2009. Accelerated Antarctic ice loss from satellite gravity measurements, *Nature Geosci.*, **2**, 859–862.

Chen, J. L., C. R. Wilson and B. D. Tapley, 2011. Interannual variability of Greenland ice losses from satellite gravimetry, *J. Geophys. Res.*, **116**(B07406).

Chen, J. L., C. R. Wilson and B. D. Tapley, 2013. Contribution of ice sheet and mountain glacier melt to recent sea level rise, *Nat. Geosci.*, **6**, 549–552.

Church, J. A., J. M. Gregory, P. Huybrechts, M. Kuhn, K. Lambeck, M. T. Nhuan, Q. Qin and P. L. Woodworth, 2001. Changes in Sea Level, Houghton, J.T., Y. Ding, D.J. Griggs, M. Noguer, P.J. van der Linden, X. Dai, K. Maskell and C.A. Johnson, eds., Climate Change 2001: The Scientific Basis. Contribution of Working Group I to the Third Assessment Report of the International Panel on Climate Change., Cambridge University Press, Cambridge, 639–693.

Cornford, S. L., D. F. Martin, D. T. Graves, D. F. Ranken, A. M. Le Brocq, R. M. Gladstone, A. J. Payne, E. G. Ng and W. H. Lipscomb, 2013. Adaptive mesh, finite volume modeling of marine ice sheets, *Journal of Computational Physics*, **232**, 529–549.

Cuffey, K. M. and W. S. B. Paterson, 2010. The Physics of Glaciers, Elsevier, Burlington, MA, 4th ed.

Delvaux, C., 2013. Pine Island Glacier dynamics and marine ice sheet instability, Master Thesis (ULB).

Docquier, D., L. Perichon and F. Pattyn, 2011. Representing grounding line dynamics in numerical ice sheet models:

Recent advances and outlook, *Surveys in Geophysics*, **32**, 417–435.

Docquier, D., D. Pollard and F. Pattyn, submitted. Thwaites Glacier grounding-line retreat: Influence of width and buttressing parameterizations, *Submitted to J. Glaciol.*.

Drouet, A. S., D. Docquier, G. Durand, R. C. A. Hindmarsh, F. Pattyn, O. Gagliardini and T. Zwinger, 2013. Grounding line transient response in marine ice sheet models, *The Cryosphere*, **7**, 395–406.

Dupont, T. K. and R. B. Alley, 2005. Assessment of the importance of ice-shelf buttressing to ice-sheet flow, *Geophys. Res. Lett.*, **32**(L04503).

Dupont, T. K. and R. B. Alley, 2006. Role of small ice shelves in sea-level rise, *Geophys. Res. Lett.*, **33**(L09503).

Durand, G., O. Gagliardini, L. Favier, T. Zwinger and E. Le Meur, 2011. Impact of bedrock description on modeling ice sheet dynamics, *Geophys. Res. Lett*, **38**(L20501).

Durand, G., O. Gagliardini, B. de Fleurian, T. Zwinger and E. Le Meur, 2009a. Marine ice sheet dynamics: Hysteresis and neutral equilibrium, *J. Geophys. Res.*, **114**(F03009).

Durand, G., O. Gagliardini, T. Zwinger, E. Le Meur and R. C. A. Hindmarsh, 2009b. Full Stokes modeling of marine ice sheets: influence of the grid size, *Ann. Glac.*, **50**(52), 109–114.

Favier, L., G. Durand, S. L. Cornford, G. H. Gudmundsson, O. Gagliardini, F. Gillet-Chaulet, T. Zwinger, A. J. Payne and A. M. LeBrocq, submitted. Irreversible retreat of Pine Island Glacier owing to topographic-induced instability, *Submitted to Nature Climate Change.*

Favier, L., O. Gagliardini, G. Durand and T. Zwinger, 2012. A three-dimensional full Stokes model of the grounding line dynamics: effect of a pinning point beneath the ice shelf, *The Cryosphere*, **6**(1), 101–112.

Feldmann, J., T. Albrecht, C. Khroulev, F. Pattyn and A. Levermann, submitted. Resolution-dependent performance of grounding line motion in a shallow model compared to a full-Stokes model according to the MISMIP3d intercomparison, *Submitted to J. Glaciol.*.

Fornberg, B., 1996. A Practical Guide to Pseudospectral Methods, Cambridge University Press.

Fretwell, P. and others, 2013. Bedmap2: improved ice bed, surface and thickness datasets for Antarctica, *The Cryosphere*, **7**(1), 375–393.

Fricker, H. A. and L. Padman, 2006. Ice shelf grounding zone structure from ICESat laser altimetry, *Geophys. Res. Lett.*, **33**(L15502).

Fürst, J., 2013. Dynamic response of the Greenland ice sheet to future climatic warming, PhD Thesis, Vrije Universiteit Brussel (VUB).

Gagliardini, O., G. Durand, T. Zwinger, R. C. A. Hindmarsh and E. Le Meur, 2010. Coupling of ice-shelf melting and buttressing is a key process in ice-sheet dynamics, *Geophys. Res. Lett.*, **37**(14).

Gillet-Chaulet, F. and G. Durand, 2010. Glaciology: Ice sheet advance in Antarctica, *Nature*, **467**, 794–795.

Gillet-Chaulet, F., O. Gagliardini, H. Seddik, M. Nodet, G. Durand, C. Ritz, T. Zwinger, R. Greve and D. G. Vaughan, 2012. Greenland ice sheet contribution to sea-level rise from a new-generation ice-sheet model, *The Cryosphere*, **6**(6), 1561–1576.

Gladstone, R. M., V. Lee, J. Rougier, A. J. Payne, H. H. Hellmer, A. M. Le Brocq, A. Shepherd, T. L. Edwards, J. Gregory and S. L. Cornford, 2012a. Calibrated prediction of Pine Island Glacier retreat during the 21st and 22nd centuries with a coupled flowline model, *Earth Planet. Sci. Lett.*, **333-334**, 191–199.

Gladstone, R. M., A. J. Payne and S. L. Cornford, 2010. Parameterising the Grounding Line in Ice Sheet Models, *The Cryosphere Discuss.*, **4**, 1063–1105.

Gladstone, R. M., A. J. Payne and S. L. Cornford, 2012b. Resolution requirements for grounding-line modelling: sensitivity to basal drag and ice-shelf buttressing, *Ann. Glaciol.*, **53**(60), 97–105.

Glen, J. W., 1955. The Creep of Polycrystalline Ice, *Proc. Royal. Soc. London A*, **228**, 519–538.

Goldberg, D., D. M. Holland and C. Schoof, 2009. Grounding line movement and ice shelf buttressing in marine ice sheets, *J. Geophys. Res.*, **114**(F024026).

Goldberg, D. N., C. M. Little, O. V. Sergienko, A. Gnanadesikan, R. Hallberg and M. Oppenheimer, 2012. Investigation of land ice-ocean interaction with a fully coupled ice-ocean model: 1. Model description and behavior, *J. Geophys. Res.*, **117**(F02037).

Gomez, N., D. Pollard, J. X. Mitrovica, P. Huybers and P. U. Clark, 2012. Evolution of a coupled marine ice sheet sea level model, *J. Geophys. Res.*, **117**(F01013).

Greve, R. and H. Blatter, 2009. Dynamics of Ice Sheets and Glaciers, Springer-Verlag Berlin Heidelberg.

Griggs, J. A. and J. L. Bamber, 2009. Ice shelf thickness over Larsen C, Antarctica, derived from satellite altimetry, *Geophys. Res. Lett.*, **36**(L19501).

Gudmundsson, G. H., 2011. Ice-stream response to ocean tides and the form of the basal sliding law, *The Cryosphere*, **5**(1), 259–270.

Gudmundsson, G. H., 2013. Ice-shelf buttressing and the stability of marine ice sheets, *The Cryosphere*, **7**(6), 647–655.

Gudmundsson, G. H., J. Krug, G. Durand, L. Favier and O. Gagliardini, 2012. The stability of grounding lines on retrograde slopes, *The Cryosphere*, **6**(6), 1497–1505.

Hanna, E., F. J. Navarro, F. Pattyn, C. M. Domingues, X. Fettweis, E. R. Ivins, R. J. Nicholls, C. Ritz, B. Smith, S. Tulaczyk, P. L. Whitehouse and H. J. Zwally, 2013. Ice-sheet mass balance and climate change, *Nature*, **498**, 51–59.

Hellmer, H. H., F. Kauker, R. Timmermann, J. Determann and J. Rae, 2012. Twenty-first-century warming of a large Antarctic ice-shelf cavity by a redirected coastal current, *Nature*, **485**, 225–228.

Herterich, K., 1987. On the Flow within the Transition Zone between Ice Sheet and Ice Shelf, Van der Veen, C.J. and J. Oerlemans, eds., Dynamics of the West Antarctic ice sheet, Dordrecht, Kluwer Academic Publishers, 185–202.

Hindmarsh, R. C. A., 1993. Qualitative Dynamics of Marine Ice Sheets, Peltier, W.R., ed., Ice in the Climate System, Berlin, Springer–Verlag, NATO ASI Series I (12), 67–99.

Hindmarsh, R. C. A., 1996. Stability of Ice Rises and Uncoupled Marine Ice Sheets, *Ann. Glaciol.*, **23**, 105–115.

Hindmarsh, R. C. A., 2004. A numerical comparison of approximations to the Stokes equations used in ice sheet and glacier modeling, *J. Geophys. Res*, **109**(F01012), doi:10.1029/2003JF000065.

Hindmarsh, R. C. A., 2006. The Role of Membrane-Like Stresses in Determining the Stability and Sensitivity of the Antarctic Ice Sheets: Back Pressure and Grounding Line Motion, *Phil. Trans. R. Soc. A*, **364**, 1733–1767.

Hindmarsh, R. C. A., 2012. An observationally validated theory of viscous flow dynamics at the ice-shelf calving front, *J. Glaciol.*, **58**, 375–387.

Hindmarsh, R. C. A. and E. Le Meur, 2001. Dynamical processes involved in the retreat of marine ice sheets, *J. Glaciol.*, **47**(157), 271–282.

Holt, J. W., D. D. Blankenship, D. L. Morse, D. A. Young, M. E. Peters, S. D. Kempf, T. G. Richter, D. G. Vaughan and H. F. J. Corr, 2006. New boundary conditions for the West Antarctic Ice Sheet: Subglacial topography of the Thwaites and Smith glacier catchments, *Geophys. Res. Lett.*, **33**(L09502).

Hutter, K., 1983. Theoretical Glaciology, Dordrecht, Kluwer Academic Publishers.

Huybrechts, P., 1990. A 3-D Model for the Antarctic Ice Sheet: a Sensitivity Study on the Glacial-Interglacial Contrast, *Climate Dyn.*, **5**, 79–92.

Huybrechts, P., 2009. West-side story of Antarctic ice, *Nature*, **458**, 295–296.

Huybrechts, P., A. Abe-Ouchi, I. Marsiat, F. Pattyn, A.J. Payne, C. Ritz and V. Rommelaere, 1998. Report of the Third EISMINT Workshop on Model Intercomparison, European Science Foundation (Strasbourg).

Huybrechts, P., A.J. Payne and The EISMINT Intercomparison Group, 1996. The EISMINT Benchmarks for Testing Ice–Sheet Models, *Ann. Glaciol.*, **23**, 1–12.

ice2sea, Consortium, 2013. From ice to high seas: Sea-level rise and European coastlines, Cambridge, United Kingdom.

Jacobs, S., A. Jenkins, C. Giulivi, F. Nitsche, B. Huber and R. Guerrero, 2012. The Amundsen Sea and the Antarctic Ice Sheet, *Oceanography*, **25**(3), 154–163.

Jacobs, S. S., A. Jenkins, C. F. Giulivi and P. Dutrieux, 2011. Stronger ocean circulation and increased melting under Pine Island Glacier ice shelf, *Nat Geosc*, **4**, 519–523.

Jenkins, A., P. Dutrieux, S. Jacobs, J. McPhail, J. Perrett, A. Webb and D. White, 2010. Observations beneath Pine Island Glacier in West Antarctica and implications for its retreat, *Nature Geosci.*, **3**(7), 468–472.

Joughin, I., W. Abdalati and M. Fahnestock, 2004. Large fluctuations in speed on Greenland's Jakobshavn Isbrae glacier, *Nature*, **432**, 608–610.

Joughin, I. and R. B. Alley, 2011. Stability of the West Antarctic ice sheet in a warming world, *Nat. Geosci.*, **4**.

Joughin, I., E. Rignot, C. E. Rosanova, B. K. Lucchitta and J. Bohlander, 2003. Timing of recent accelerations of Pine Island Glacier, Antarctica, *Geophys. Res. Lett.*, **30**(13), doi:10.1029/2003GL017609.

Joughin, I., B. E. Smith and D. M. Holland, 2010a. Sensitivity of 21st century sea level to ocean-induced thinning of Pine Island Glacier, Antarctica, *Geophys. Res. Lett.*, **37**(L20502).

Joughin, I., B. E. Smith, I. M. Howat, T. Scambos and T. Moon, 2010b. Greenland flow variability from ice-sheet-wide

velocity mapping, *J. Glaciol.*, **56**(197).

Joughin, I., S. Tulaczyk, J. L. Bamber, D. Blankenship, J. W. Holt, T. Scambos and D. G. Vaughan, 2009. Basal conditions for Pine Island and Thwaites Glaciers, West Antarctica, determined using satellite and airborne data, *J. Glaciol.*, **55**(190), 245–257.

Jouvet, G. and C. Graser, 2013. An adaptive Newton multigrid method for a model of marine ice sheets, *J. Comp. Phys.*, **252**, 419–437.

Katz, R. F. and M. G. Worster, 2010. Stability of ice-sheet grounding lines, *Proc. R. Soc. A*, **466**(2118), 1597–1620.

King, M. A., R. J. Bingham, P. Moore1, P. L. Whitehouse, M. J. Bentley and G. A. Milne, 2012. Lower satellite-gravimetry estimates of Antarctic sea-level contribution, *Nature*, **491**, 586–590.

Larour, E., J. Schiermeier, E. Rignot, H. Seroussi, M. Morlighem and M. Paden, 2012. Sensitivity analysis of Pine Island Glacier ice flow using ISSM and DAKOTA, *J. Geophys. Res*, **117**.

Le Brocq, A. M., A. J. Payne and A. Vieli, 2010. An improved Antarctic dataset for high resolution numerical ice sheet models (ALBMAP v1), *Earth Syst. Sci. Data*, **2**(2), 247–260.

Lestringant, R., 1994. A Two-Dimensional Finite-Element Study of Flow in the Transition Zone between an Ice Sheet and an Ice Shelf, *Ann. Glaciol.*, **20**, 67–72.

MacAyeal, D. R., 1989. Large-scale Ice Flow over a Viscous Basal Sediment: Theory and Application to Ice Stream B, Antarctica, *J. Geophys. Res*, **94**(B4), 4071–4087.

MacAyeal, D. R., 1992. Irregular Oscillations of the West Antarctic Ice Sheet, *Nature*, **359**, 29–32.

MacAyeal, D. R., C. L. Hulbe, P. Huybrechts, V. Rommelaere, J. Determann and C. Ritz, 1996. An ice-shelf model test based on the Ross Ice Shelf, *Ann. Glaciol.*, **23**, 46–51.

MacGregor, J. A., G. A. Catania, M. S. Markowski and A. G. Andrews, 2012. Widespread rifting and retreat of ice-shelf margins in the eastern Amundsen Sea Embayment between 1972 and 2011, *J. Glaciol.*, **58**(209), 458–466.

Martin, M. A., R. Winkelmann, M. Haseloff, T. Albrecht, E. Bueler, C. Khroulev and A. Levermann, 2011. The Potsdam Parallel Ice Sheet Model (PISM-PIK). Part 2: Dynamic equilibrium simulation of the Antarctic ice sheet, *The Cryosphere*, **5**, 727–740.

Meehl, G. H., A. Hu, C. Tebaldi, J. M. Arblaster, W. M. Washington, H. Teng, B. M. Sanderson, T. Ault, W. G. Strand and J. B. White, 2012. Relative outcomes of climate change mitigation related to global temperature versus sea-level rise, *Nature Climate Change*, **2**, 576–580.

Morinishi, Y., T. S. Lund, O. V. Vasilyev, and P. Moin, 1998. Fully Conservative Higher Order Finite Difference Schemes for Incompressible Flow, *J. Comp. Phys.*, **143**, 90–124.

Morland, L. W., 1987. Unconfined Ice shelf flow, *Dynamics of the West Antarctic Ice Sheet, edited by C. J. V. van der Veen and J. Oerlemans, Cambridge University Press, United Kingdom and New York, NY USA.*

Morlighem, M., E. Rignot, H. Seroussi, E. Larour, H. Ben Dhia and D. Aubry, 2010. Spatial patterns of basal drag inferred using control methods from a full-Stokes and simpler models for Pine Island Glacier, West Antarctica, *Geophys. Res. Lett.*, **37**(14).

Moss, R. H. and others, 2010. The next generation of scenarios for climate change research and assessment, *Nature*, **463**, 747–756.

Nicholls, R. J. and A. Cazenave, 2010. Sea-Level Rise and Its Impact on Coastal Zones, *Science*, **328**, 1517–1520.

Nick, F. M., A. Vieli, M. L. Andersen, I. Joughin, A. Payne, T. L. Edwards, F. Pattyn and R. S. W. van de Wal, 2013. Future sea-level rise from Greenland's main outlet glaciers in a warming climate, *Nature*, **2**(2), 110–114.

Nick, F. M., A. Vieli, I. M. Howat and I. Joughin, 2009. Large-Scale Changes in Greenland Outlet Glacier Dynamics Triggered at the Terminus, *Nat. Geosc.*, **497**, 235–238.

Nitsche, F.O., S.S. Jacobs, R.D. Larter and K. Gohl, 2007. Bathymetry of the Amundsen Sea continental shelf: Implications for geology, oceanography, and glaciology, *Geochemistry, Geophysics, Geosystems*, **8**(10).

Olbers, D. and H. H. Hellmer, 2010. A box model of circulation and melting in ice shelf caverns, *Ocean Dyn.*, **60**(1), 141–153.

Parizek, B. R., K. Christianson, S. Anandakrishnan, R. B. Alley, R. T. Walker, R. A. Edwards, D. S. Wolfe, G. T. Bertini, S. K. Rinehart, R. A. Bindschadler and S. M. J. Nowicki, 2013. Dynamic (in)stability of Thwaites Glacier, West Antarctica, *J. Geophys. Res.*, **118**(2), 638.

Park, J. W., N. Gourmelen, A. Shepherd, S. W. Kim, D. G. Vaughan and D. J. Wingham, 2013. Sustained retreat of the Pine Island Glacier, *Geophys. Res. Lett.*, **40**, 2137.

Paterson, W. S. B., 1994. The Physics of Glaciers, Oxford, Pergamon Press, 3rd ed.

Pattyn, F., 2000. Ice-Sheet Modelling at Different Spatial Resolutions: Focus on the Grounding Line, *Ann. Glaciol.*, **31**, 211–216.

Pattyn, F., 2003. A New 3D Higher-Order Thermomechanical Ice-Sheet Model: Basic Sensitivity, Ice-Stream Development and Ice Flow across Subglacial Lakes, *J. Geophys. Res.*, **108**(B8, 2382), doi:10.1029/2002JB002329.

Pattyn, F. and G. Durand, 2013. Why marine ice-sheet model predictions may diverge in estimating future sea-level rise, *Geophys. Res. Lett.*, **40**, 1–5.

Pattyn, F., A. Huyghe, S. De Brabander and B. De Smedt, 2006. Role of Transition Zones in Marine Ice Sheet Dynamics, *J. Geophys. Res.*, **111**(F02004), doi:10.1029/2005JF000394.

Pattyn, F. and others, 2012. Results of the Marine Ice Sheet Model Intercomparison Project, MISMIP, *The Cryosphere*, **6**, 573.

Pattyn, F. and others, 2013. Grounding-line migration in plan-view marine ice-sheet models: results of the ice2sea MISMIP3d intercomparison, *J. Glaciol.*, **59**(215), 410–422.

Pollard, D. and R. M. DeConto, 2009. Modelling West Antarctic Ice Sheet Growth and Collapse Through the Past Five Million Years, *Nature*, **458**, doi:10.1038/nature07809.

Pollard, D. and R. M. DeConto, 2012. Description of a hybrid ice sheet-shelf model, and application to Antarctica, *Geosci. Model Dev.*, **5**, 1273–1295.

Price, S., I. Howat and B. Smith, 2011. Committed sea-level rise for the next century from Greenland ice sheet dynamics during the past decade, *Proc. Nat. Aca of Sci.*, **108**, 8978–8983.

Primer, A., 2011. Mathematical modeling of Earth's dynamical systems, Princeton University Press.

Pritchard, H. D., S. R. M. Ligtenberg, H. A. Fricker, D. G. Vaughan, M. R. van den Broeke and L. Padman, 2012. Antarctic ice-sheet loss driven by basal melting of ice shelves, *Nature*, **484**, 502–505.

Rignot, E., 2008. Changes in West Antarctic ice stream dynamics observed with ALOS PALSAR data, *Geophys. Res. Lett.*, **35**(L12505).

Rignot, E., J. L. Bamber, M. R. van den Broeke, C. Davis, Y. Li, W. J. van de Berg and E. van Meijgaard, 2008. Recent Antarctic ice mass loss from radar interferometry and regional climate modelling, *Nature Geosci.*, **1**, 106–110.

Rignot, E., S. Jacobs, J. Mouginot and B. Scheuchl, 2013. Ice shelf melting around Antarctica, *Science*, **341**(6143), 266–270.

Rignot, E., I. Velicogna, M. R. van den Broeke, A. Monaghan and J. Lenaerts, 2011. Acceleration of the contribution of the Greenland and Antarctic ice sheets to sea level rise, *Geophys. Res. Lett.*, **38**(L05503).

Rignot, E. J., 1998. Fast recession of a West Antarctic Glacier, *Science*, **281**(5376), 549–551.

Ritz, C., V. Rommelaere and C. Dumas, 2001. Modeling the Evolution of the Antarctic Ice Sheet over the Last 420000 Years: Implications for Altitude Changes in the Vostok Region, *J. Geophys. Res.*, **106**(D23), 31943–31964.

Robison, R. A. V., H. E. Ruppert and M. G. Worster, 2009. Dynamics of viscous grounding lines, *J. Fluid Mech.*, **648**(doi:10.1017/S0022112009993119), 363–380.

Scambos, T. A., T. M. Haran, M. A. Fahnestock, T. H. Painter and J. A. Bohlander, 2007. MODIS-based Mosaic of Antarctica (MOA) data sets: continent-wide surface morphology and snow grain size, *Remote Sens. Environ.*, **111**, 242–257.

Schoof, C., 2007a. Ice sheet grounding line dynamics: Steady states, stability and hysteresis, *J. Geophys. Res.*, **112**(F03S28).

Schoof, C., 2007b. Marine ice sheet dynamics. Part I. The case of rapid sliding, *J. Fluid Mech.*, **573**, 27–55.

Schoof, C. and R.C.A. Hindmarsh, 2010. Thin-film flows with wall slip: an asymptotic analysis of higher order glacier flow models, *Quart. J. Mech. Appl. Math.*, **63**(1), 73–114.

Schoof, C., F. Pattyn and R.C.A. Hindmarsh, 2007. Benchmarks and intercomparison program for marine ice sheet models, *Geophysical Research Abstracts*, **9**(EGU2007-A-04644).

Schroeder, D. M., D. D. Blankenship and D. A. Young, 2013. Evidence for a water system transition beneath Thwaites Glacier, West Antarctica, *Proc. Nat. Aca of Sci.*, 10.1073/pnas.1302828110.

Scott, J. B. T., G. H. Gudmundsson, A. M. Smith, R. G. Bingham, H. D. Pritchard and D. G. Vaughan, 2009. Increased rate of acceleration on Pine Island Glacier strongly coupled to changes in gravitational driving stress, *The Cryosphere*, **3**(125-131).

Shepherd, A., D. Wingham, D. Wallis, K. Giles, S. Laxon and A. V. Sundal, 2010. Recent loss of floating ice and the

consequent sea level contribution, *Geophys. Res. Lett.*, **37**(L13503).

Shepherd, A., D. J. Wingham, J. A. D. Mansley and H. F . J. Corr, 2001. Inland thinning of Pine Island Glacier, West Antarctica, *Science*, **291**, 862–864.

Shepherd, A. and others, 2012. A reconciled estimate of ice-sheet mass balance, *Science*, **338**, 1183–1189.

Solomon, S., D. Qin, M. Manning, Z. Chen, M. Marquis, K. B. Averyt, M. Tignor and H. L. Miller (ed.), 2007. Climate Change 2007: The Physical Science Basis. Contribution of Working Group I to the Fourth Assessment Report of the Intergovernmental Panel on Climate Change, Cambridge University Press, Cambridge, United Kingdom and New York, NY, USA.

Steig, E. J., Q. Ding, D. S. Battisti and A. Jenkins, 2012. Tropical forcing of Circumpolar Deep Water Inflow and outlet glacier thinning in the Amundsen Sea Embayment, West Antarctica, *Ann. Glaciol.*, **53**(60), 19–28.

Thoma, M., A. Jenkins, D. Holland and S. Jacobs, 2008. Modelling Circumpolar Deep Water intrusions on the Amundsen Sea continental shelf, Antarctica, *Geophys. Res. Lett.*, **35**(L18602).

Thomas, I. D. and others, 2011. Widespread low rates of Antarctic glacial isostatic adjustment revealed by GPS observations, *Geophysical Research Letters*, **38**(22).

Thomas, R. H. and C. R. Bentley, 1978. A Model for Holocene Retreat of the West Antarctic Ice Sheet, *Quat. Res.*, **10**, 150–170.

Tinto, K. J. and R. E. Bell, 2011. Progressive unpinning of Thwaites Glacier from newly identified offshore ridge: Constraints from aerogravity, *Geophys. Res. Lett.*, **38**(L20503).

Turner, J. and G. J. Marshall, 2011. Climate Change in the Polar Regions, Cambridge, Cambridge University Press.

Turner, J. and others, 2013. Antarctic climate change and the environment: an update, *Polar Record*.

Van de Berg, W. J., M. R. van den Broeke, C. H. Reijmer and E. van Meijgaard, 2006. Reassessment of the Antarctic surface mass balance using calibrated output of a regional atmospheric climate model, *J. Geophys. Res*, **111**(D11104), doi:10.1029/2005JD006495.

Van den Broeke, M., J. Bamber, J. Ettema, E. Rignot, E. Schrama, W. J. van de Berg, E. van Meijgaard, I. Velicogna and B. Wouters, 2009. Partitioning Recent Greenland Mass Loss, *Science*, **326**, 984–986.

Velicogna, I., 2009. Increasing rates of ice mass loss from the Greenland and Antarctic ice sheets revealed by GRACE, *Geophys. Res. Lett.*, **36**(L19503), doi:10.1029/2009GL040222.

Vieli, A. and A.J. Payne, 2005. Assessing the ability of numerical ice sheet models to simulate grounding line migration, *J. Geophys. Res.*, **110**(F01003).

Walton, D. W. H., 2013. Antarctica: Global science from a frozen continent, Cambridge University Press.

Wayman, E., 2013. Taking Antarctica's temperature: Frozen continent may not be immune to global warming, *Science News*, **184**(2), 18.

Weertman, J., 1974. Stability of the junction of an ice sheet and an ice Shelf, *J. Glaciol.*, **13**(67), 3–11.

Williams, C.R., R. C.A. Hindmarsh and R.J. Arthern, 2012. Frequency response of ice streams, *Proc. Roy. Soc. Ser. A.*, 3285–3310.

Wingham, D. J., A. Shepherd, A. Muir and G. J. Marshall, 2006. Mass Balance of the Antarctic Ice Sheet, *Phil. Trans. R. Soc. A*, **364**, 1627–1635.

Wingham, D. J., D. W. Wallis and A. Shepherd, 2009. Spatial and temporal evolution of Pine Island Glacier thninning, 1995-2006, *Geophys. Res. Lett.*, **36**(L17501), doi:10.1029/2009GL039126.

Winkelmann, R., M. A. Martin, M. Haseloff, T. Albrecht, E. Bueler, C. Khroulev and A. Levermann, 2011. The Potsdam Parallel Ice Sheet Model (PISM-PIK). Part 1: Model description, *The Cryosphere*, **5**, 715–726.

Wouters, B., J. L. Bamber, M. R. van den Broeke, J. T. M. Lenaerts and I. Sasgen, 2013. Limits in detecting acceleration of ice sheet mass loss due to climate variability, *Nat. Geosci.*, **6**, 613–616.

Zwally, H. J., J. Li, A. C. Brenner, M. Beckley, H. G. Cornejo, J. DiMarzio, M. B. Giovinetto, T. A. Neumann, J. Robbins, J. L. Saba and W. Wang D. Yi, 2011. Greenland ice sheet mass balance: distribution of increased mass loss with climate warming; 2003Ű07 versus 1992Ű2002, *J. Glac.*, **57**(201), 88–102.

Publications

Peer-reviewed Publications

Lead author

- Docquier, D., L. Perichon and F. Pattyn (2011). Representing grounding line dynamics in numerical ice sheet models: Recent advances and outlook, *Surveys in Geophysics*, 32, 417–435, doi: 10.1007/s10712-011-9133-3.

- Docquier, D., D. Pollard and F. Pattyn (submitted). Thwaites Glacier grounding-line retreat: Influence of width and buttressing parameterizations, *Submitted 23/05/2013 to Journal of Glaciology*.

- Drouet, A. S., D. Docquier, G. Durand, R. C. A. Hindmarsh, F. Pattyn, O. Gagliardini and T. Zwinger (2013). Grounding line transient response in marine ice sheet models, *The Cryosphere*, 7, 395–406, doi: 10.5194/tc-7-395-2013.

Secondary author

- Pattyn F., K. Matsuoka, D. Callens, H. Conway, M. Depoorter, D. Docquier, B. Hubbard, D. Samyn and J. L. Tison (2012). Melting and refreezing beneath Roi Baudouin Ice Shelf (East Antarctica) inferred from radar, GPS, and ice core data, *Journal of Geophysical Research*, 117, F04008, doi:10.1029/2011JF002154.

- Pattyn, F., L. Perichon, G. Durand, L. Favier, O. Gagliardini, R. C. A. Hindmarsh, T. Zwinger, T. Albrecht, S. Cornford, D. Docquier, J. Fürst, D. Goldberg, G. H. Gudmundsson, A. Humbert, M. Huetten, P. Huybrechts, G. Jouvet, T. Kleiner, E. Larour, D. Martin, M. Morlighem, T. Payne, D. Pollard, M. Rückamp, O. Rybak, H. Seroussi, M. Thoma and N. Wilkens (2013). Grounding-line migration in plan-view marine ice-sheet models: results of the ice2sea MISMIP3d intercomparison, *Journal of Glaciology*, 59 (215): 410–422, doi:10.3189/2013JoG12J129.

Non-peer-reviewed Publications

- Docquier, D. and L. S. Sorensen (2013). Young scientists at the heart of ice2sea. In: *From Ice to High Seas: Sea-level rise and European coastlines* [The ice2sea Consortium], Cambridge, UK.

- Docquier, D., F. Pattyn, X. Fettweis and P. Huybrechts (2013). Ice2sea: Contribution of land ice to future sea-level rise. In: *Science Connection 41 (special issue): Antarctica* [Belspo], Brussels, `http://www.belspo.be/belspo/organisation/publ_science_en.stm`.

Significant Communications

- Docquier D., D. Pollard D. and F. Pattyn (May 2013). Modelling Thwaites Glacier grounding-line retreat, Poster presented at *ice2sea Open Forum IV*, London.

- Docquier D. and L. S. Sorensen (May 2013). ice2sea: The perspective of early career scientists, Poster presented at *ice2sea Open Forum IV*, London.

- Docquier D., D. Pollard D. and F. Pattyn (December 2012). Grounding line migration on unstable bedrock slopes: The example of Thwaites Glacier, Antarctica, Talk presented at *American Geophysical Union Fall Meeting*, San Francisco.

- Docquier D., A. S. Drouet, R. C. A. Hindmarsh, G. Durand and F. Pattyn (April 2012). Grounding line migration captured by flowline ice sheet models, Poster presented at *European Geosciences Union General Assembly*, Vienna.

- Docquier D., A. S. Drouet, R. C. A. Hindmarsh, G. Durand and F. Pattyn (February 2012). Grounding line migration captured by flowline ice sheet models, Poster presented at *ice2sea Open Forum III*, Amsterdam.

- Docquier, D., F. Pattyn, L. Perichon, A. S. Drouet, L. Favier and G. Durand (June 2011). Representing grounding line dynamics in numerical ice sheet models, Poster presented at *International Glaciological Society Symposium on Interactions of Ice Sheets and Glaciers with the Ocean*, La Jolla, California.

- Docquier, D., L. Perichon and F. Pattyn (March 2011). Representing grounding line dynamics in numerical ice sheet models, Poster presented at *ice2sea Open Forum II*, Copenhagen.

- Docquier, D., F. M. Nick, L. Perichon and F. Pattyn (June 2010). Effect of numerical resolution on grounding line position in marine ice sheet models, Poster presented at *24th International Forum for Research into Ice Shelf Processes*, Bad Bederkesa, Germany.

- Docquier, D., F. M. Nick, L. Perichon and F. Pattyn (May 2010). Grounding line migration captured by flowline ice sheet models, Poster presented at *European Geosciences Union General Assembly*, Vienna.

Since the mid-20th century, global average temperatures have dramatically risen mostly due to the increasing amount of greenhouse gas emissions in the atmosphere. The effects of this recent global warming are already evident and could be exacerbated in the near future if no real action is taken. Recent ice loss in West Antarctica, monitored by satellite measurements and other techniques, gives cause for concern in such a warming world. A major part of this loss has been driven by warm water masses penetrating underneath the ice shelves in this region. This has led to a flow acceleration of the inland outlet glaciers and a greater discharge of ice to the ocean. The actual resulting contribution of West Antarctica to sea-level rise is estimated to be ~ 0.2 mm per year between 1992 and 2011, i.e. about one third of the ice-sheet contribution (Antarctica and Greenland), and is expected to increase in the near future.

In this thesis, we first clearly demonstrate that modeling grounding-line (the boundary between grounded and floating ice) migration depends on both the numerical approach and the physical approximation of the ice-sheet model used. Ice-sheet models prescribing the ice flux at the grounding line and using appropriate physical level and numerical approach converge to the same steady-state grounding-line position irrespective of the grid size used. However, the transient behavior of those models is less accurate than other models and leads to an overestimated grounding-line discharge. Therefore, they need to be used with particular attention on short time scales. Furthermore, the non-inclusion of vertical shear stress in those models increases the effective viscosity and gives steady-state grounding-line positions further downstream when compared to full-Stokes models.

The second major finding of this thesis is the high control of geometry (glacier width and bedrock topography) on Thwaites Glacier, one of the fastest-flowing outlet glaciers in West Antarctica. A flowline finite-difference Shallow-Shelf Approximation (SSA) model is applied to the glacier and shows that ice-flow convergence (through width parameterization) slows down the grounding-line retreat when compared to simulations where the width is constant. A new buttressing parameterization is also tested on the glacier and permits a better understanding of this effect. Finally, the three-dimensional version of the model above is applied to Thwaites Glacier and highlights the strong control of lateral variations in bedrock topography on grounding-line migration.